Simulation and Testing of Metallic Aperture Arrays at Terahertz Frequencies

HILL, CARLO,ALEXANDER,KIM

Simulation and Testing of Metallic Aperture Arrays at Terahertz Frequencies

Carlo Alexander Kim Hill

A Thesis submitted for the degree of Doctor of Philosphy

School of Engineering and Computing Sciences

Durham University

March 2016

Abstract

Since the demonstration of Extraordinary Optical Transmission (EOT) in sub-wavelength aperture arrays, first at optical then at terahertz (THz) frequencies, the role of Surface Plasmon Polaritons (SPPs) in this phenomenon has been under investigation. By studying the interaction between THz radiation and free standing metal foils, which contain periodic arrays of apertures, this thesis explores the interaction between rectangular waveguided modes controlled by aperture dimensions and SPP modes defined by aperture periodicity.

Fabrication of a free standing metal foil perforated by micron scale 5:1 aspect ratio rectangular holes with varied array spacings is performed by photolithography and electroplating. Such free standing metal foils are shown to demonstrate EOT at THz frequencies when studied by terahertz time-domain spectroscopy (THz-TDS). Results obtained by the systematic variation of aperture size and lattice spacing are presented, accompanied by finite-difference time-domain (FDTD) simulation data. The changing aperture array dimensions allow for the isolation of the different resonant modes present in the EOT phenomena.

Further exploitation of the interaction between the two resonant modes is provided by altering the incident angle between the free standing metal aperture array and the THz field.

The high frequency resolution provided by THz Vector Network Analyser measurements allows for small changes in transmission spectra to be observed as the resonant modes are brought into close proximity.

The removal of a fixed periodic spacing between the sub-wavelength apertures perforating the metal foil removes a necessary component of SPP excitation. The design of an array of aperiodic sub-wavelength apertures is presented. This array demonstrates EOT in the absence of SPPs.

Furthermore, SPPs induced by the periodic x-axis aperture spacing, and controlled by THz field incidence angle, are used to extinguish the sharp transmission resonance produced by the sub-wavelength apertures. To this author's knowledge this is the first reporting of resonant transmission extinguished by SPP excitation and manipulation.

Table of Contents

Abstract ..... **i**

Table of Contents ..... **iii**

Nomenclature ..... **v**

Acknowledgements ..... **viii**

Copyright ..... **ix**

Publication List ..... **x**

Conference Papers x

Further Publications x

1. Introduction **1**

1.1 Structure of Thesis 3

2. Measurement Techniques **6**

2.1 Terahertz Time Domain Spectroscopy (THz-TDS) 7

2.1.1 THz Generation and Detection 8

2.1.2 Durham THz-TDS Arrangement 10

2.1.3 THz-TDS Reference Pulse 11

2.1.4 Data Extraction 16

2.2 Vector Network Analyser 23

2.2.1 Extension Module Calibration 24

2.2.2. Dynamic Range 27

2.3 Conclusions 33

3. Surface Plasmons **35**

3.1 Formal Definition 36

3.2 Origin of SPP Modes 38

3.3 Excitation of SPPs 41

3.4 Losses and Decay Length 43

3.5 Optical Response of a Metal 45

3.6 Extraordinary Optical Transmission 46
3.7 THz Surface Plasmons 48
3.8 Rectangular Sub-Wavelength Apertures 51
3.9 Conclusions 53
4. Finite-Difference THz Simulations 54
4.1 Introduction to FDTD 55
4.2 Numerical Limitations 56
4.3 Electromagnetic Source 58
4.4 Perfect Electrical Conductors 61
4.5 Simulation Geometry 61
4.6 Simulation Screenshots 64
4.6.1 Unstable Geometry 64
4.6.2 Normal Incidence 66
4.6.3 Angular Incidence 69
4.7 Commercial Simulation Comparisons 72
4.8 Conclusions 73
5. Transmission Mechanisms 75
5.1 Fabrication 76
5.1.1 Lithography 76
5.1.2 Copper Electroplating 78
5.2 Fixed Ratio Arrays 79
5.3 Fixed Apertures Varied Square Lattice 83
5.4 Periodic Rectangular Lattice 92
5.5 Conclusions 94
6. Controlling SPP Minima 96
6.1 Varying Incident Angle 97
6.2 Effect of Surface Quality 103
6.3 Randomly Located Aperture Array 106
6.4 Varied Periodic Spacing 109
6.5 Origin of Minima 114
6.6 Conclusions 117

7. Conclusions **119**

7.1 Further Work 122

Bibliography **127**

Nomenclature

TDS	Time-Domain Spectroscopy
SPP	Surface Plasmon Polariton
SP	Surface Plasmon
EOT	Extraordinary Optical Transmission
VNA	Vector Network Analyser
FDTD	Finite-Difference Time-Domain
FFT	Fast Fourier Transform
SNR	Signal to Noise Ratio
RMS	Root Mean Square
IF	Intermediate Frequency
TIR	Total Internal Reflection
E_{THz}	THz electric field
J	Current density
t	Time
e	Charge of an electron
v_e	Relative speed between an electron and a hole
n_e	Carrier density
d	Distance

n	Refractive index
c	Speed of light in a vacuum
T_N	Sample interval
f_c	Nyquist frequency
f_s	Sampling frequency
f_r	Resonant Frequency
df	Frequency resolution
N	Number of samples
σ	Standard deviation
μ	Mean
P_n	Noise power
k	Boltzmann's constant
T	Absolute temperature
B	Receiver bandwidth
E	Energy
ħ	Reduced Planck's constant
v	Frequency of oscillation
ω	Angular frequency
ω_p	Plasma frequency
ω_{spp}	SPP frequency
λ	Wavelength
k_x, k_y, k_z	Wavenumber
ϵ	Permittivity
ϵ_m	Permittivity of metal

ϵ_d	Permittivity of dielectric
ϵ_0	Permittivity of free space
μ_r	Relative permeability
$\mathfrak{J}$	Imaginary complex component
$\mathfrak{R}$	Real complex component
m_e	Effective mass of an electron
η_B	Aperture transmission efficiency
r	Aperture radius
a_x	Aperture width
a_y	Aperture length
d	Square lattice constant
S_c	Courant number
Δt	Time step
$\Delta x, \Delta y, \Delta z$	Spatial step
c_p	Continuous phase velocity
$\tilde{c}_p$	Discrete phase velocity
N_λ	Nodes per wavelength

Acknowledgements

I would like begin by thanking my supervisors Dr Andrew Gallant and Professor David Wood, for their advice and guidance throughout my PhD; despite the numerous times I ignored it, they have supported me throughout. In particular I would like to thank Andrew for his straightforward honest advice when it was needed. And David for always pushing me to achieve more.

I would also like the thank Dr Claudio Balocco for his involvement and numerous discussions about my work, my understanding of surface plasmons would not be same without his involvement. Dr Mark Rosamond was especially influential during the first years of my PhD, I thank him for the late nights of fabrication and discussion; it has not been the same since he left.

I dedicate this thesis to my partner Rachel, without her love and support I might not have gotten through the harder times. And to my mother who first pushed me towards Durham University which has become such a large part of my life.

Copyright

Publication List

Conference Papers

The work in this thesis has featured in the following publications:

- C.K.A. Hill, M.C. Rosamond, D. Dai, D. Wood, A.J. Gallant “Metal aperture arrays for operation in the THz region” Terahertz Science and Technology. EOS Topical Meeting. 3rd 2012. (TST 2012), EOS, 2012.

- C.K.A. Hill, L.E. Dodd, M.C. Rosamond and D. Wood, “Zero Temperature Coefficient of Resistivity in Nichrome”, Proc. MicroMechanics Europe (MME 2013), 2013.

- C. A. K. Hill, C. Balocco, D. Wood and A. J. Gallant “Free standing metal aperture array acting as a variable bandpass filter in the THz region” Radio Science Conference (URSI AT-RASC), 2015 1st URSI Atlantic, IEEE, 2015.

- C. K. A. Hill, A. K. Klein, C. Balocco, D. Wood and A. J. Gallant “Effect of Wood's anomalies on the THz transmission spectra of free-standing metallic hole arrays” Infrared, Millimeter, and Terahertz waves (IRMMW-THz), 2015 40th International Conference on, IEEE, 2015.

Further Publications

Further publications on which I am an author:

- D. Wood, M. Chamberlain, A. Baragwanath, L. Dodd, C. Hill and A. J. Gallant, "Micromachined Devices for Use in Terahertz Applications", Advances in Science and Technology, Vol. 81, pp. 20-27, 2013.

Chapter 1

Introduction

The terahertz (THz) region of the electromagnetic spectrum, commonly referred to as the 'THz gap', is typically taken to reside between 300 GHz and 10 THz. A lack of coherent sources has left this region of the spectrum relatively unexplored when compared to its neighbouring microwave and infrared counterparts. The mature communication technologies of the microwave region continue to move to ever higher frequencies in search of higher data transfer rates and new applications. At the same time, new efficient laser sources are beginning to populate the far-infrared region bringing the wealth of knowledge related to optics to a new regime.

In the past decade there has been a large uptake in the use of THz for non-destructive testing for security and non-invasive imaging purposes, for instance finding imaging applications in the fields of art conservation [1] and archaeology [2] [3] due to various

advantages over x-ray imaging techniques [4]. Characteristic THz spectra have been shown to exist for illicit drugs and explosives [5] [6], which along with passive imaging techniques [7], not permitted for higher energy x-rays, make the region open for exploitation for security purposes.

The advent of terahertz time-domain spectroscopy (THz-TDS) [8] [9] enabled the generation and detection of THz pulses, providing a broadband THz source. Recent years have continued to see a steady growth in research into the THz region [10]. With a recent rise in the number of publications aimed towards applications, as the potential of the THz region is beginning to be more widely understood. THz has attracted much interest from industry and academia alike due to its non-ionising nature for the testing of biological processes [11].

As well as a vast amount of research in the areas of imaging and spectral fingerprinting in the THz regime, recent years have seen a rising interest in the area of THz metamaterials. Surface plasmon polaritons (SPPs) are a class of surface waves which have been under study and in use since the 1970's in the fields of Raman spectroscopy [12] and surface plasmon resonance [13]. SPPs have become a renewed area of interest since the (re)discovery of extraordinary optical transmission (EOT) in 1998 [14] at optical frequencies. The work of Pendry [15] predicted the ability to engineer a 'spoof' surface plasmon at almost any frequency where none existed before, at metal surfaces. Controlled only by the geometry of subwavelength features, this class of surface mode provides the ability to tailor a metal's effective plasma response into the THz regime. The excitation, confinement and manipulation of these surface modes provide new opportunities for sensing and imaging. Easily explored and exploited by microfabrication techniques on the μm scale (1 THz = 300 μm) the THz regime is well matched to the photo-lithography techniques available at Durham University. THz frequency SPPs have been observed and exploited for 2D aperture

array transmission [16], biological [17] and dielectric [18] sensing, and guiding [19] and focusing [20] of THz radiation.

The work in this thesis focuses on 2D metal aperture arrays acting as metamaterials in the THz regime. 2D metal aperture arrays have been shown to display EOT at both optical [14] and THz [21] frequencies. However, the transmission mechanisms behind the phenomena are still under investigation both theoretically and experimentally. Figure 1.1 shows an example of the µm scale periodic patterning used to engineer a spoof surface plasmon at THz frequencies alongside a picture of such a free-standing copper patterned array.

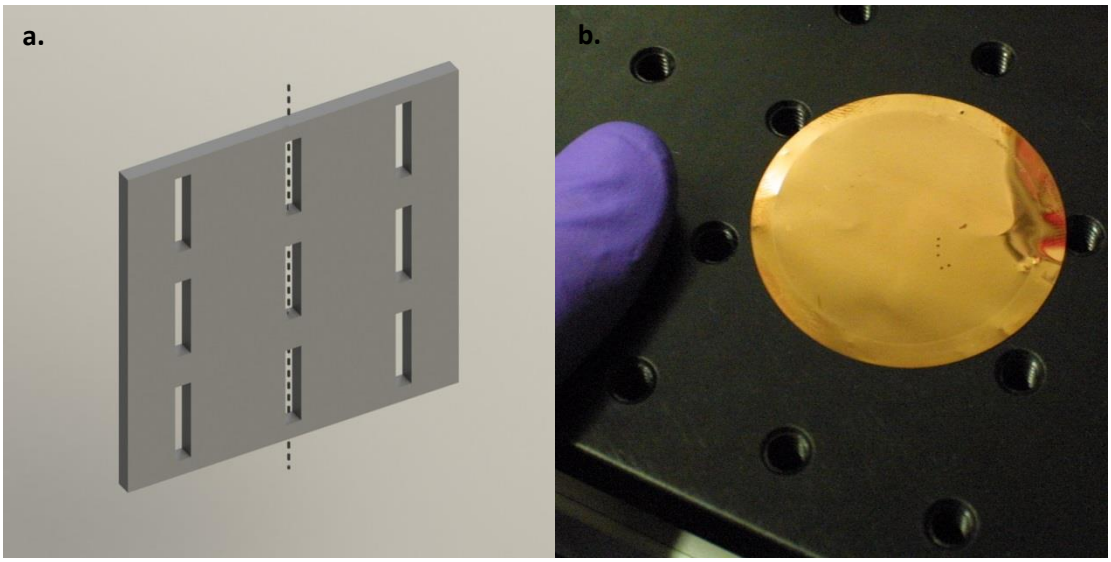

Figure 1.1: a.Rectangular 5:1 aspect ratio subwavelength apertures periodically spaced in a square lattice array to form a THz metamaterial, b. Photograph of free-standing copper array of such 5:1 aspect ratio subwavelength apertures fabricated at Durham Univserity.

1.1 Structure of Thesis

The work presented in this thesis utilises well established microfabrication techniques to produce free standing metallic periodic aperture arrays. Chapter 2 will present the two measurement techniques used to establish the transmission properties of various aperture arrays at THz frequencies. Firstly, the THz-Time Domain Spectroscopy system used to obtain the broadband response to a THz time domain pulse is presented; a brief outline of the

generation and detection methods used in the Durham University system are given, accompanied by the changes made to increase the available scan range. Then a THz-Vector Network Analyser (THz-VNA) system using WR1.0 –VNAX extension modules to produce free space coherent continuous wave (CW) THz radiation is presented. This VNA system allows for much faster, higher frequency resolution, direct frequency domain measurements by comparison to THz-TDS measurements, albeit at the cost of reduced bandwidth.

Chapter 3 presents the underlying physics behind the resonant features observed in THz aperture arrays. Beginning with an introduction to surface plasmons at optical frequencies, the well-established case for 'spoof' surface plasmons at THz frequencies will be presented, including direct observation and simulation of the electric field close to the metal interface. The role of aperture resonance in the phenomena of EOT will be discussed for the particular case of rectangular apertures.

Chapter 4 introduces the finite-difference time-domain (FDTD) simulation techniques used throughout chapters 5 and 6 to compare to experimental observations. The simulation program framework (Lucifer), written in Fortran, is under continued development at Durham University. Meshing issues related to the problem of varying the incident angle between the THz source and aperture array are discussed. Two commercial simulation packages, Lumerical and CST, are briefly presented. The data produced by the commercial simulation packages is compared to experimental data and that produced by Lucifer to assess the quality of Lucifer's solution.

Chapter 5 presents the systematic investigation of the transmission spectra of rectangular free space aperture arrays. Measurements obtained by THz-TDS are compared to simulation data, and the sources of various resonant features are established. The transmission is shown to greatly exceed unity when normalised to free space aperture area. The

transmission strength, both in absolute and relative to free space terms, is investigated as a function of the periodic geometry. Finally, the role of periodic spacing in sub-wavelength rectangular aperture arrays is established.

Chapter 6 varies the incident angle between the incoming THz radiation and the free standing metal film. The manipulation of the incident angle changes the SPP resonant frequency, allowing the interaction between the aperture and SPP resonant modes to be observed. The sharp resonant features produced by this varying angle are observed by THz-VNA transmission spectra. The case for the deviation between real copper aperture array measurements and simulation results is presented. Finally, the transmission produced by an aperiodic array of apertures is observed, establishing the existence of a transmission resonance in the absence of a periodic structure.

Chapter 7 concludes the thesis, presenting simulation data produced by FDTD suggesting an interesting direction for future research, if the not insignificant fabrication difficulties can be overcome.

Chapter 2

Measurement Techniques

Terahertz (THz) transmission properties allow for the characterisation of materials in the THz regime. Few materials respond naturally to THz radiation, and much of the work in the THz regime is focused around the development and control of THz metamaterials. The characterisation of such a metamaterial, and the control of, and interaction between, observed resonances are the goals of this thesis.

Many detection methods are sensitive to THz radiation; incoherent detectors such as the Golay cell and Bolometer are able to measure the magnitude of THz radiation, but lack phase information. Coherent detection methods provide phase information as well as magnitude by utilising knowledge of the relative phase between the input and output while observing the output radiation. Coherent detection allows for the detection of low power

THz radiation by the use of a lock-in amplifier. A lock-in amplifier can extract a signal with a known carrier wave despite large noise.

Each detection method can be defined by its relative merits: the frequency range in which it can effectively operate; the frequency resolution which it can achieve; difficulties in setup/alignment; and additional environmental requirements (pressure, temperature, atmosphere control). This chapter will present the two experimental techniques used to obtain THz transmission properties of the metallic aperture arrays investigated in this thesis; terahertz time-domain spectroscopy (THz-TDS), and a Vector Network Analyser (VNA).

THz-TDS is a well-established method for investigations in this frequency regime, allowing coherent investigations in the 'THz Gap' since its first demonstration in 1989 [22]. Working in the time domain, THz-TDS allows for the indirect measurement of frequency components by a Fast Fourier Transform (FFT).

VNAs have been extensively used at lower frequencies, and through the recent addition of higher frequency extension modules, it is now possible to work directly in the frequency domain up to and above 1 THz. This can be considered the final stage in closing the 'THz Gap', as optical phenomena and techniques meet those utilised by microwave and telecommunications technologies.

2.1 Terahertz Time Domain Spectroscopy (THz-TDS)

The majority of the experiments presented in this thesis have been conducted using a THz-TDS experimental setup. The technique allows for very low power THz pulses to be detected with a high signal to noise ratio due to the coherent nature of the radiation.

This section will give an introduction to the THz-TDS techniques used for the experiments presented in chapter 5. The background physics which underpins these techniques will be outlined along with a description of the THz-TDS system used at Durham University. Finally, some of the system changes made to enable the longer scanning times, with the absence of system reflections, are detailed. Longer time domain scans are able to fully capture resonant features with long decay times, while also improving the frequency resolution obtainable by FFT.

2.1.1 THz Generation and Detection

All the THz-TDS experiments undertaken in this work have been conducted with a photoconductive THz source. The design and production of high intensity, larger bandwidth THz photoconductive sources is an active area of research [23] [24].

In a photoconductive antenna, an external electric field is applied across a semiconducting substrate gap by two electrodes. When the semiconductor is illuminated by a laser pulse, of above bandgap energy, electron-hole pairs are created. The field separates the carriers and drives them to opposite electrodes creating a transient current. The THz field emitted by the antenna is proportional to the time derivative of the transient current (2.1), and therefore contains a positive half cycle as the current rises to saturation followed by a negative half cycle as the current decays.

$$E_{THz} \propto \frac{\partial J}{\partial t} \qquad \textbf{(2.1)}$$

Where E_{THz} is the emitted THz field, J is the current density, and t is time. This leads to, from [25];

$$E_{THz} \propto e v_e \frac{\partial n_e}{\partial t} + e n_e \frac{\partial v_e}{\partial t} \quad \textbf{(2.2)}$$

where e is the charge of an electron, v_e is the relative speed between an electron and a hole, and n_e is the carrier density.

The first term on the right-hand side of (2.2) is due to a change in carrier density, while the second is due to the acceleration of the carriers under the electric field. Ultra-short femtosecond laser pulses create a rapid change in carrier density ensuring the first term is large. Carrier velocity is related to carrier mobility and field bias. GaAs has a reasonably high mobility (5000 cm^2/Vs) [26] and a high electric field strength breakdown (100 kV/cm) [27], making it a good choice as a photoconductive antenna substrate.

Though a reliable source of terahertz radiation, the typical power produced by a photoconductive antenna is in the order of μW [28]. To detect the low power pulses an efficient coherent detection is required. Two main types of coherent detection exist; using photoconductive antennas and electro-optic crystals. Photoconductive antennas work as detectors via the inverse process by which they function as sources. A THz electric field induces a voltage difference across the electrodes; excitation of the semiconductor by a laser pulse allows a current to flow by creating electron-hole pairs. The photocurrent across the electrodes is related to the instantaneous THz electric field.

The principle of electro-optic detection lies in the Pockels effect, in which birefringence in an optical medium is induced by an external electric field. This effect allows the THz electric field to induce a change in polarisation of the synchronised femtosecond pulse which is directly proportional to the incident electric field. In the absence of an external THz field, the femtosecond pulse passes through the crystal with its polarisation unchanged. This linearly

polarised pulse next passes through a quarter wave plate, becoming circularly polarised. Upon entering the Wollaston Prism, this circularly polarised beam is split into its divergent orthogonal linear components of equal magnitude. The presence of a THz electric field upon the detection crystal causes an elliptical polarisation in the femtosecond pulse due to birefringence. This elliptically polarised pulse will emerge from the quarter wave plate with an altered polarisation, but still elliptical in nature. The Wollaston Prism splits this elliptically polarised beam into unequal orthogonal linear components. It is by measuring the change in the orthogonal beams with a pair of balanced photodiodes that we can indirectly measure the THz radiation. This change in intensity between the photodiodes, though arbitrary in magnitude, is directly proportional to the instantaneous THz electric field strength.

A ZnTe crystal is the most commonly used crystal for electro-optic terahertz detection due to its high second order non-linearity. The sensitivity of a crystal to a given radiation frequency is dependent upon its electro-optic coefficient (second order non-linearity) and thickness. The coherence length is the distance over which the slight phase velocity difference between the THz wave and femtosecond pulse can be tolerated, and therefore is the upper bound for crystal thickness [29]. The bandwidth of a detector is, however, also dependent upon the crystal thickness, with thicker crystals displaying a higher sensitivity but reduced bandwidth. Many other electro-optic crystals exist, and their properties of merit have been considered elsewhere [30].

2.1.2 Durham THz-TDS Arrangement

The Durham THz-TDS set-up uses a combination of a photoconductive antenna for generation and electro-optic ZnTe crystal for coherent detection as shown in Figure 2.1. In a coherent THz-TDS system, a pulsed laser beam is split to be used for both excitation and

detection of THz. When the excitation (pump) beam is incident upon a suitable source, a broadband THz pulse is produced. A lack of suitable materials in the THz region limits the available components for THz manipulation. The resultant THz pulse is collected via parabolic mirrors and either transmitted through, or reflected off, the sample of interest. The transmitted, or reflected, beam is then collected by more parabolic mirrors and focused onto the detector. The optical path length of the detection (probe) beam is set so that the two path lengths are identical; therefore, both pulses are incident upon an electro-optic detector at the same time. By varying the path length of the detection beam, the relative THz electric field strength can be mapped over a ps timescale.

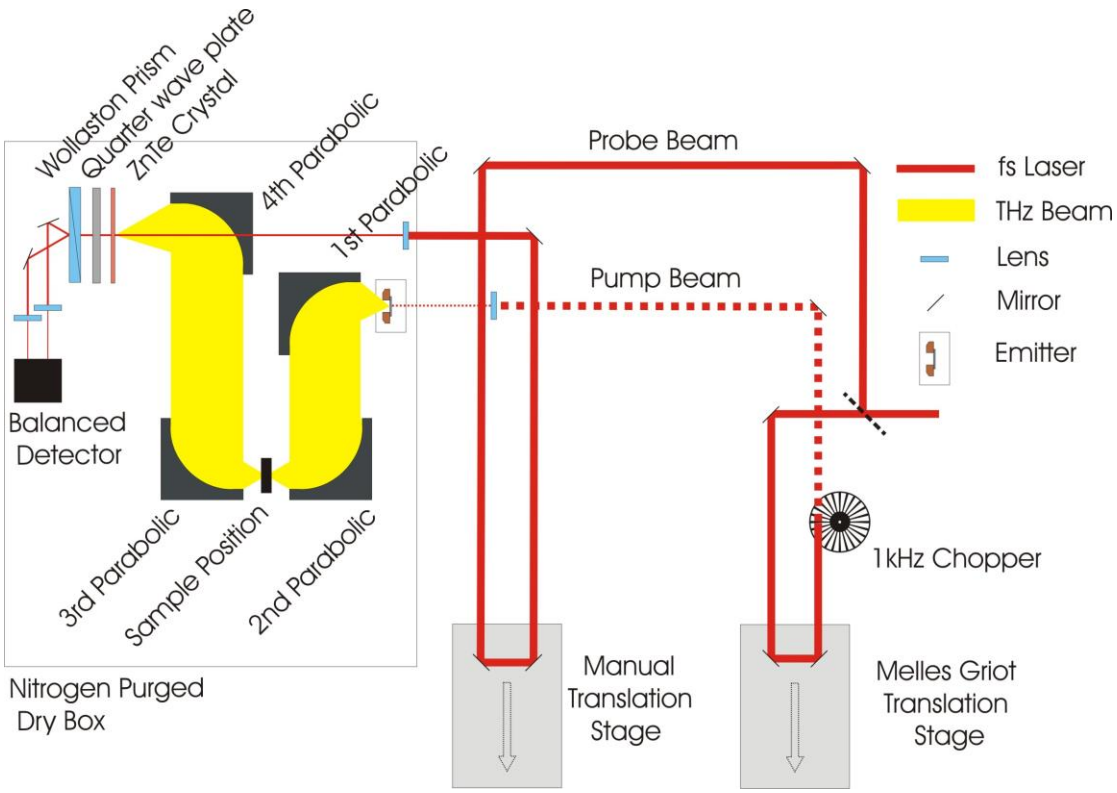

Figure 2.1: Durham THz-TDS setup.

2.1.3 THz-TDS Reference Pulse

In order to make a quantitative measurement of the effect a given sample has upon the THz wave, an investigation begins with a reference scan. For transmission, this is the absence of

a sample, and for reflection, the sample position is replaced by a plane mirror. Another scan is then conducted in the presence of the sample and comparisons between the two recorded waveforms can be made.

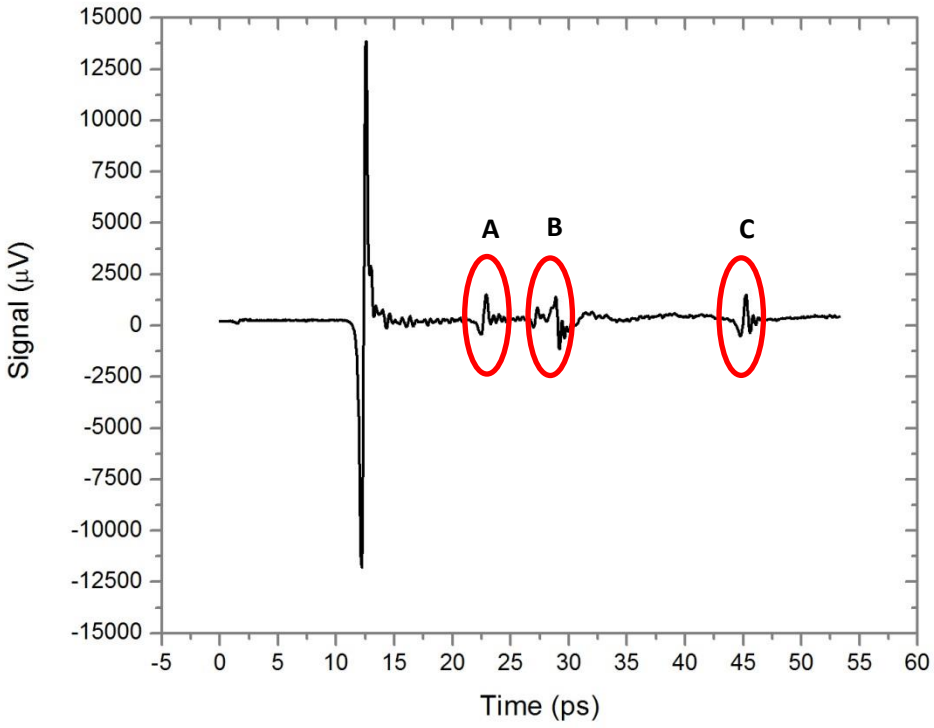

Figure 2.2: Typical THz reference pulse from Durham THz-TDS system.

Figure 2.2 shows a typical THz-TDS reference pulse obtained using electro-optic detection. It can be seen that secondary pulses (system reflections) (A, B, C) exist in the absence of a sample. These system reflections can have a number of possible sources, and removing or minimising them is not trivial. In order to remove, minimise or move a system reflection, its source must first be identified. Figure 2.2 shows three significant reflections with delays of approximately 10, 16 and 34 ps. The most common source of a THz-TDS reflection is a double internal reflection in either the GaAs emitter, as shown in Figure 2.3, or the ZnTe detection crystal.

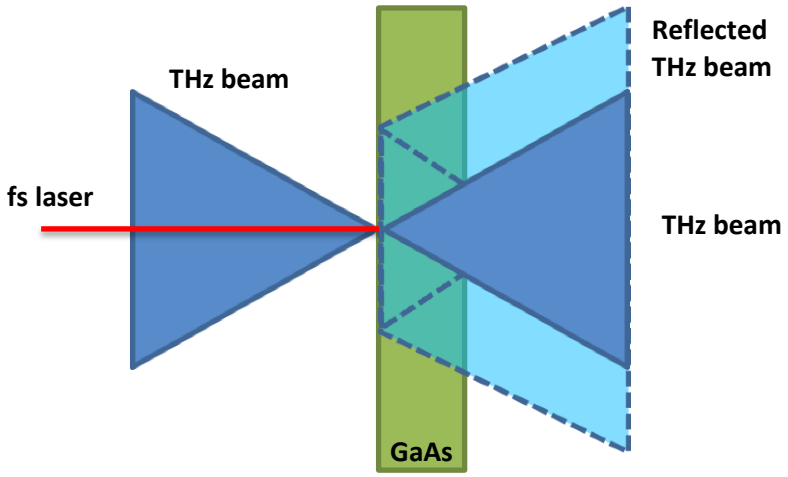

Figure 2.3: Femtosecond laser incident upon GaAs substrate, resultant THz beam and back face reflection.

Internal reflections should vary in magnitude, shape and position as the beam's angle of incident at the interface changes. By varying the angle of both the GaAs emitter and ZnTe crystal, it is possible to determine if they are the source of any of these reflections.

Figure 2.4 shows the effect of altering the angle of the GaAs emitter to be off-axis in the femtosecond beam path. There is a clear change in shape and magnitude of reflections B and C, indicating this system reflection is caused by an internal reflection of the THz pulse at the GaAs-Air interface.

A 600 µm GaAs substrate will incur a 6.8 ps time of flight to a 1 THz beam as shown in equation (2.3).

$$t = \frac{dn}{c} = \frac{600x10^{-6}x\ 3.4}{3x10^{8}} = 6.8\ ps \qquad \textbf{(2.3)}$$

Where t is time, d is distance, n is an approximate refractive index at THz frequencies; c is the speed of light in a vacuum.

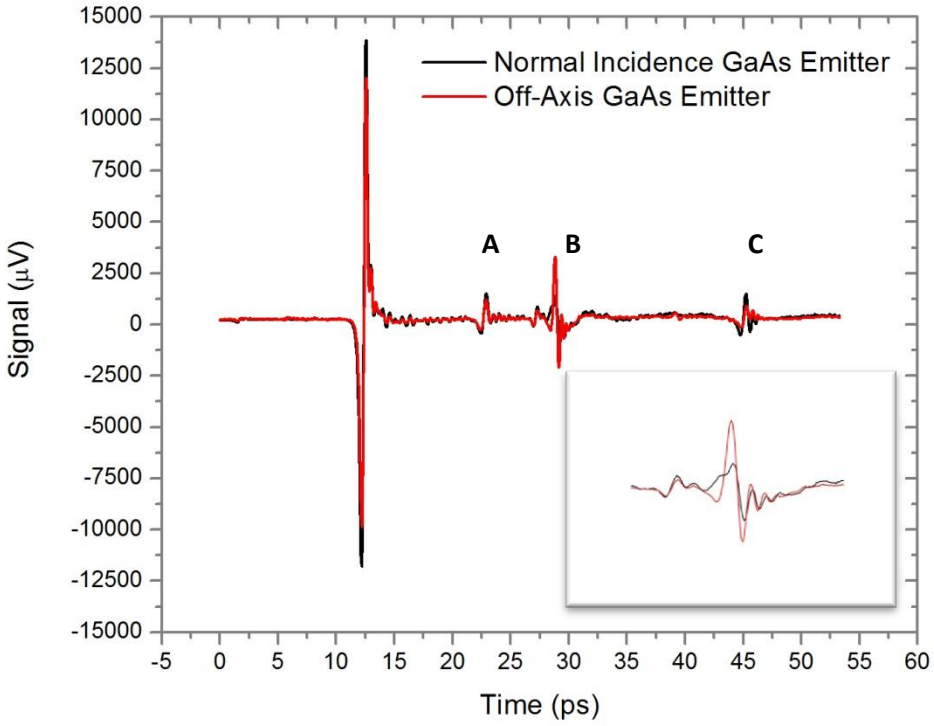

Figure 2.4: THz-TDS reference scan for varied GaAs emitter angle.Insert shows reflection B.

Reflection B exists between 14 and 18 ps after the initial THz pulse. The shortest delay time matches the time of flight of a 1 THz wave internally reflected from the front and back faces of a 600 µm GaAs substrate. This surface of the GaAs substrate is, however, not polished and therefore the THz wave will incur various internal reflection paths dependent upon the exact incident angle at the interface. This explains the irregular shaping of reflection B observed in Figure 2.4.

To reduce the size of reflection B relative to the main pulse, better refractive index matching is required at the interface. An additional layer of the GaAs substrate bonded to the emitter back face provides an exact index match assuming no air gap and a well matched thin bonding film. To test the effect that this additional bonded GaAs layer would have upon the emitter structure, GaAs layers were placed into the free space THz beam focal point (between the 2nd and 3rd parabolic mirrors, as indicated in Figure 2.1). A comparison

between an empty free space path and that containing a GaAs layer provides a close approximation to the effect of adding an additional layer to the emitter.

Figure 2.5 shows the effect of a 600 µm GaAs layer upon a THz beam; a delay of 6 ps in all spectral features can be seen as well as a 40% reduction in peak voltage. A second sample comprised of two GaAs layers bonded by a thin layer of PMMA has also been placed in the focal point. The second GaAs layer introduced a similar response to the first; an additional 6 ps delay and a 40% reduction in peak voltage. The thin film of PMMA used to bond the two GaAs layers together is shown to have no appreciable effect upon the transmission properties of the sample, and no additional internal reflections caused by the GaAs/PMMA/GaAs bond have been observed. An additional 600 µm layer of GaAs bonded by a PMMA thin film to the emitter GaAs substrate should therefore minimise reflection B observed in Figure 2.2.

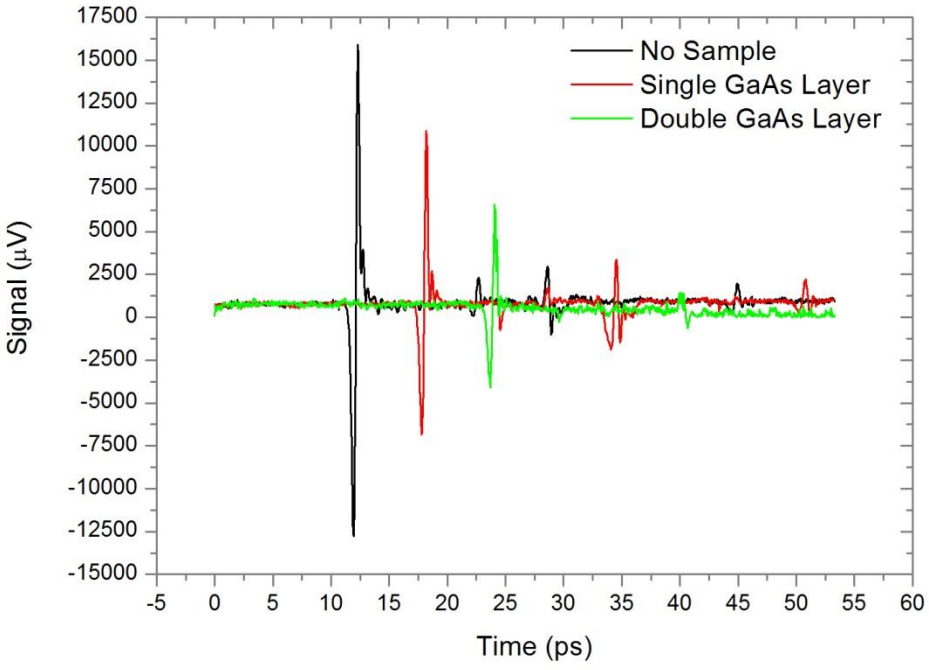

Figure 2.5: Effect of a 600 µm GaAs layer placed in THz beam focal point.

Figure 2.6 shows that by doubling the thickness of the ZnTe crystal used for opto-electric detection reflection A ≈10 ps after the main pulse is moved to ≈20 ps after the main pulse. The introduction of a second GaAs layer, bonded onto the back of the emitter by a thin layer of PMMA, minimises the reflection B; ≈16 ps after the main pulse. The effective length of a scan which is free from significant reflections has been doubled, and no appreciable loss in signal to noise ratio has been incurred. The increased ZnTe crystal thickness, however, reduces the system bandwidth as discussed in section 2.1.1.

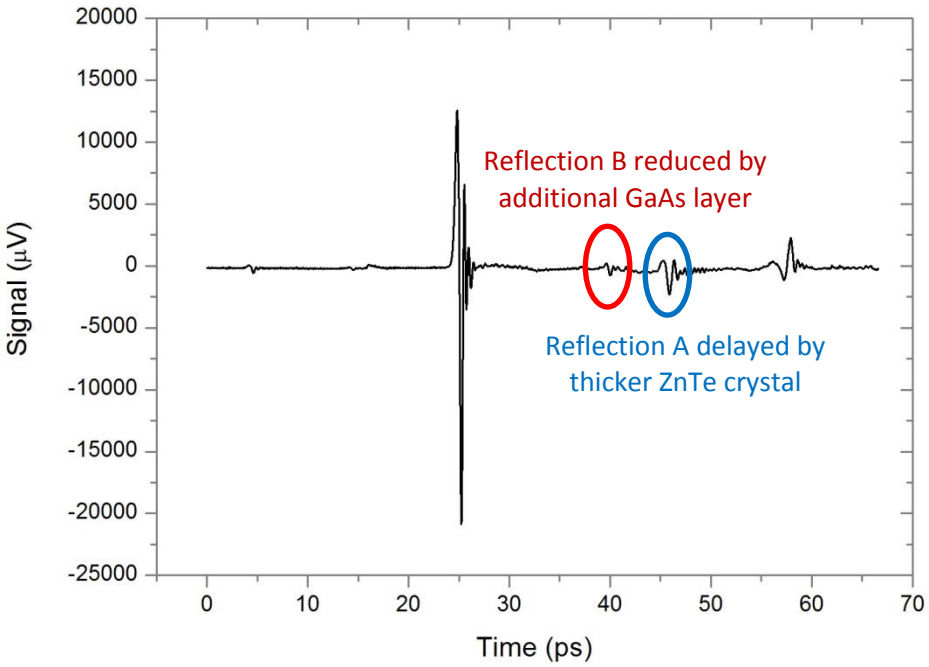

Figure 2.6: THz-TDS reference scan for 1 mm ZnTe Crystal and double layer GaAs Emitter.

2.1.4 Data Extraction

The time domain signal of a sample placed into the THz-TDS beam is a powerful visual aid in analysing a sample's response to a broadband THz pulse. Plasmonic resonances, time delays and changes in pulse shape are all important tools in understanding the physics of how the

sample interacts with THz radiation. However, frequency domain analysis is required for the full characterisation of a material's response to a broadband input.

An FFT is an algorithm used to convert between the time and frequency domains. An FFT is a necessary approximation of a continuous Fourier transform due to the sampled nature of a data set. The degree to which an FFT can accurately approximate a continuous function is dependent upon the sample interval, T_N, and truncation length [31]. For a continuous function containing no frequencies greater than f_c the Fourier transform can be uniquely determined by a sample interval given by, from [32];

$$T_N = \frac{1}{2f_c} \qquad \textbf{(2.4)}$$

If the waveform is sampled at a frequency of at least twice the largest frequency component, there is no loss of information as a result of sampling. An FFT of sampled data cannot, however, exactly recreate a continuous Fourier transform of a function due to its finite length. The introduction of a truncation function to the continuous data set creates ripples in the frequency domain. These ripples cannot be removed, and instead can be minimised, by choosing a truncation function, or sample length, as long as possible.

A range of truncation functions exist beyond a rectangular function of one within the interval and zero outside. The aim of these functions is to reduce the spectral leakage or ripple effect caused by a function of finite length and remove discontinuities at the joining of two functions. A range of functions are normally available in common FFT programs such as rectangular, triangular, Hann, and Hamming.

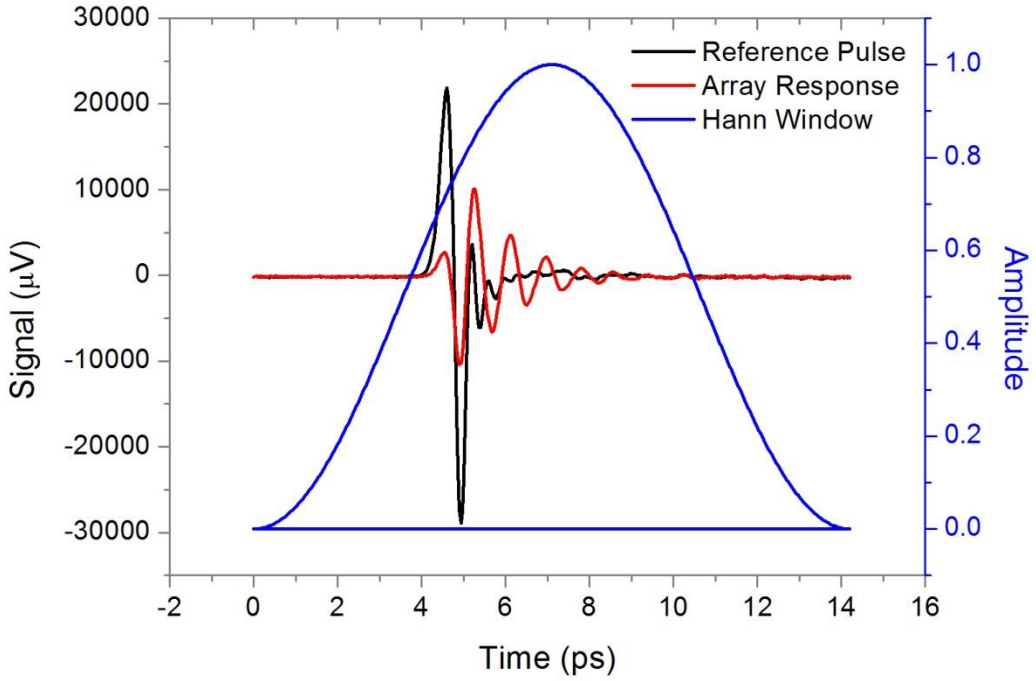

Figure 2.7: Example reference pulse and array response overlaid by Hann FFT windowing function.

Figure 2.7 shows an example THz reference pulse and the resultant aperture array time domain response. Overlaid on to this time domain response is the Hann windowing function as can be applied to each data point during an FFT.

Figure 2.8 shows the frequency domain response to these time domain data sets, applying a Rectangular and Hann window respectively. Under the differing windowing functions the resultant frequency domain features (peak position, bandwidth, FWHM) remain largely unchanged. However, the amplitude response of the Hann windowing function is reduced. All windowing functions, beyond rectangular, multiply each data point by a value between zero and one, reducing the amplitude of each data point depending upon time position. This leads to a reduction in FFT amplitude dependent upon signal position in the time domain. Importantly, the reduction in amplitude of the reference pulse and aperture array response is not matched. This is due to the reference pulse time domain power and array response time domain power not existing over the same data points. As the resonant aperture array

response and reference pulse decay over different time scales, it is unavoidable that they will display differing amplitude reductions when applying a Hann function. The result in this example is the incorrect conclusion that the peak frequency response of the aperture array (≈ 1.2 THz) is greater than the input reference pulse power at that frequency.

When analysing a dataset with finite duration, such as a THz pulse or a sample's response to an impulse, functions beyond rectangular are not required and, as shown in Figure 2.8, can introduce time dependent amplitude inaccuracies. Throughout this thesis rectangular windowing functions have been applied to all time domain data sets, maintaining the relative frequency domain amplitude between reference and array response.

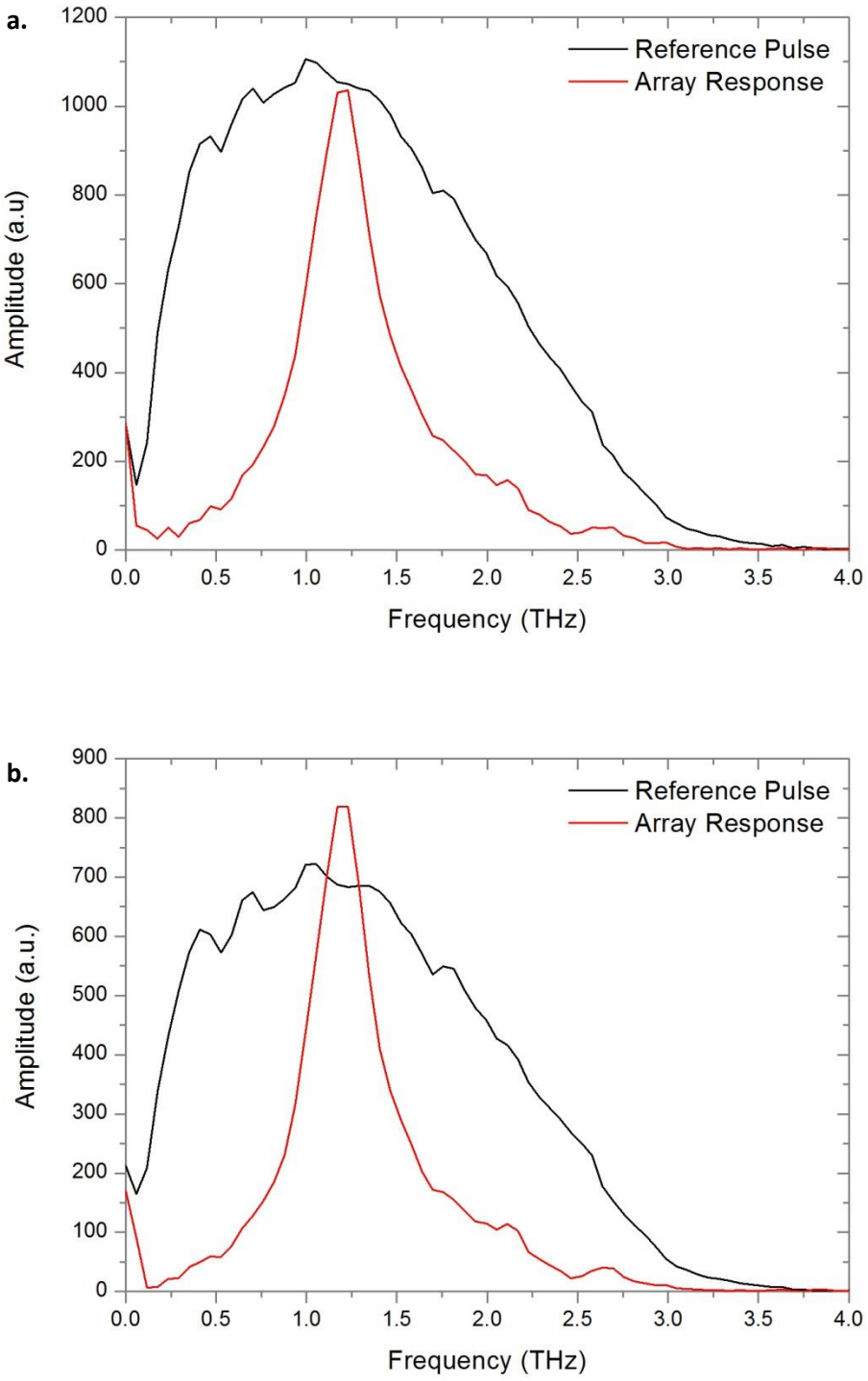

Figure 2.8: FFT response to time domain data given in Figure 2.7 for a. Rectangular FFT window function, b. Hann FFT windowing function.

Zero-padding is a method by which a time domain data set is increased in length prior to an FFT by the addition of zeroes. The increased data set size results in more closely spaced discrete data points in the resultant frequency domain. The FFT's ability to distinguish between adjacent frequencies, however, will not be increased; the net effect is a smoothing of the frequency domain data which, although it may visually look improved, has not increased the accuracy of the frequency response.

The presence of multiple pulses out of phase in a time domain data set creates noise in the resultant frequency domain. The minimising of system reflections discussed in section 2.1.3 also minimises the resultant FFT disturbances and allows for improved signal to noise ratio (SNR). The THz reference pulse data set displayed in Figure 2.9a contains a THz pulse with a 6 mm scan length, equivalent to 40 ps of freespace propagation. The combined photoconductive antenna and electro-optic detection bandwidth is shown in Figure 2.9b.

The timescan and FTT data shown in Figure 2.9 have received no smoothing, dc offset correction, zero padding or additional data processing beyond a rectangular truncation FFT. With a reference pulse of length 40 ps, it is possible to obtain the full response of not only a single resonant aperture array (≈ 8 ps oscillation) but multiple aperture arrays in series without interference from reflections. That these responses have been obtained without any smoothing or data processing removes the possibility of introducing numerical artefacts into resultant normalised frequency domain data.

Figure 2.9b displays broadband frequencies between 0.1 and 3.0 THz, devoid of water absorption lines due to liquid nitrogen purging in a controlled dry box atmosphere. The 40 ps scan length provides a large time domain region in which to observe resonances. The minimising of system reflections in the time domain minimises ripples in the frequency domain data.

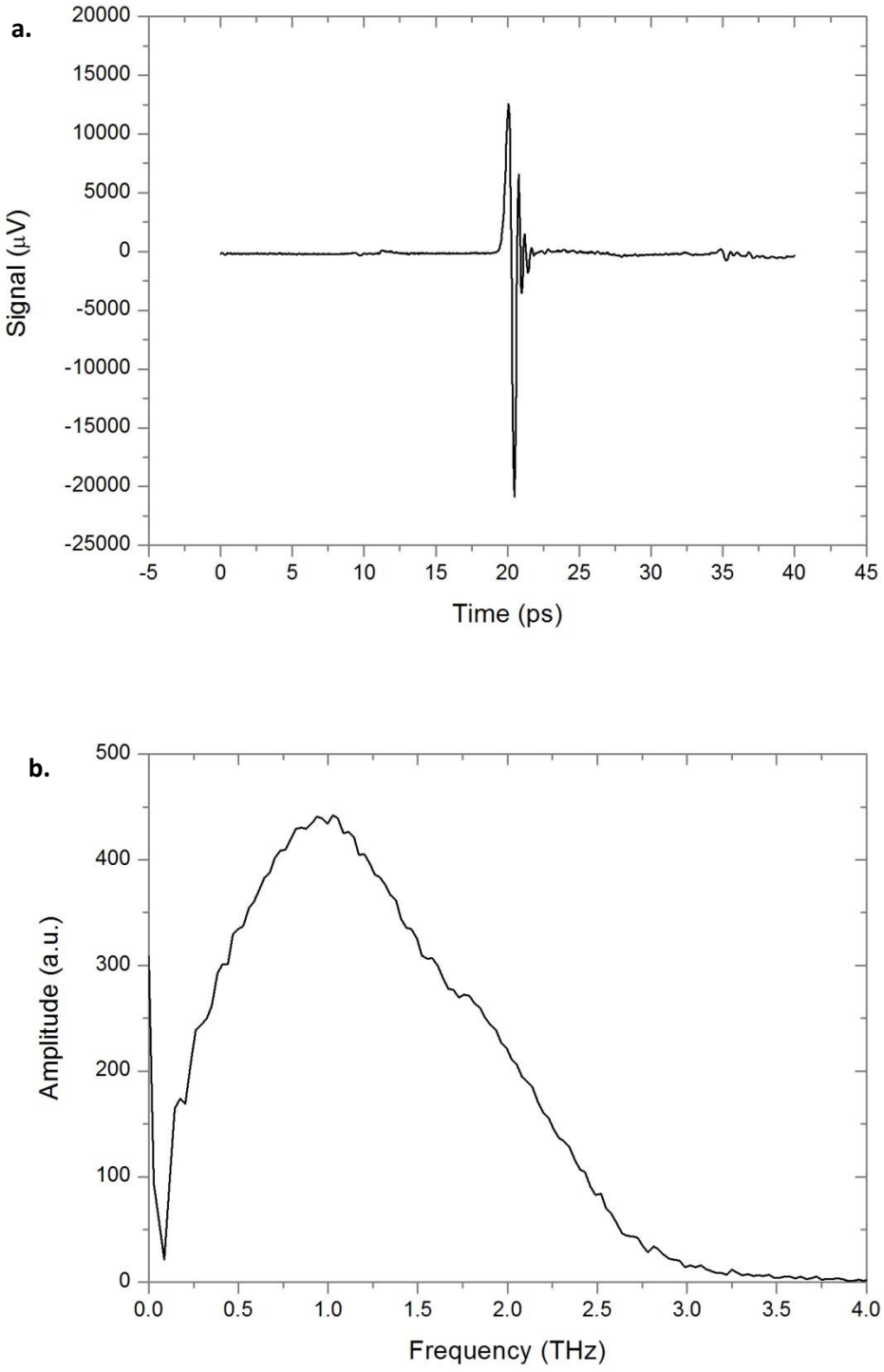

Figure 2.9: a. THz-TDS 40 ps reference pulse. b. Resultant FFT

The SNR of the time domain pulse shown in Figure 2.9a can be defined as the peak to peak amplitude of the THz pulse divided by the pre-pulse noise (0-18 ps). The noise can be defined by its average power, root mean square (RMS). The THz pulse shown in Figure 2.9a has a peak to peak amplitude of 25.6 mV, the pre-pulse noise has an RMS of 57.2 µV. The SNR for this pulse is 450:1.

The frequency resolution, df, is controlled by the sampled signal length;

$$df = \frac{1}{T_N} = \frac{f_s}{N} \quad \textbf{(2.5)}$$

Where T_N is the sample length, f_s is the sampling frequency and N is the number of samples.

From equation 2.5, the frequency resolution of Figure 2.9b is 25 GHz.

2.2 Vector Network Analyser

A VNA is an instrument used to most commonly measure scattering, or S, parameters. The Durham University system uses an Agilent Technologies N5224A PNA with WR1.0-VNAX frequency extension modules [33]. The WR1.0-VNAX extension modules are the current state of the art in high frequency VNA components, using THz Schottky diodes as triplers and subharmonic mixers upon the N5224A PNA's standard specification to achieve a frequency range of 750 GHz to 1.1 THz. This section will outline the calibration procedure undertaken to characterise the measurement range.

For clarity the combined N5224A PNA with WR1.0-VNAX extension modules is defined as the device, while the device with the addition of WR1.0H Diagonal Horn antennas and a pair of parabolic mirrors to produce a free space THz beam is defined as the system. For the purposes of this research the operation of the VNA device beyond a black-box has not been

considered. Only the manipulation and guiding of the THz radiation by the horn antennas and parabolic mirrors, creating the THz test system. Figure 2.10 shows a diagram of the THz VNA device and system, as defined, used to obtain the measurements in this thesis.

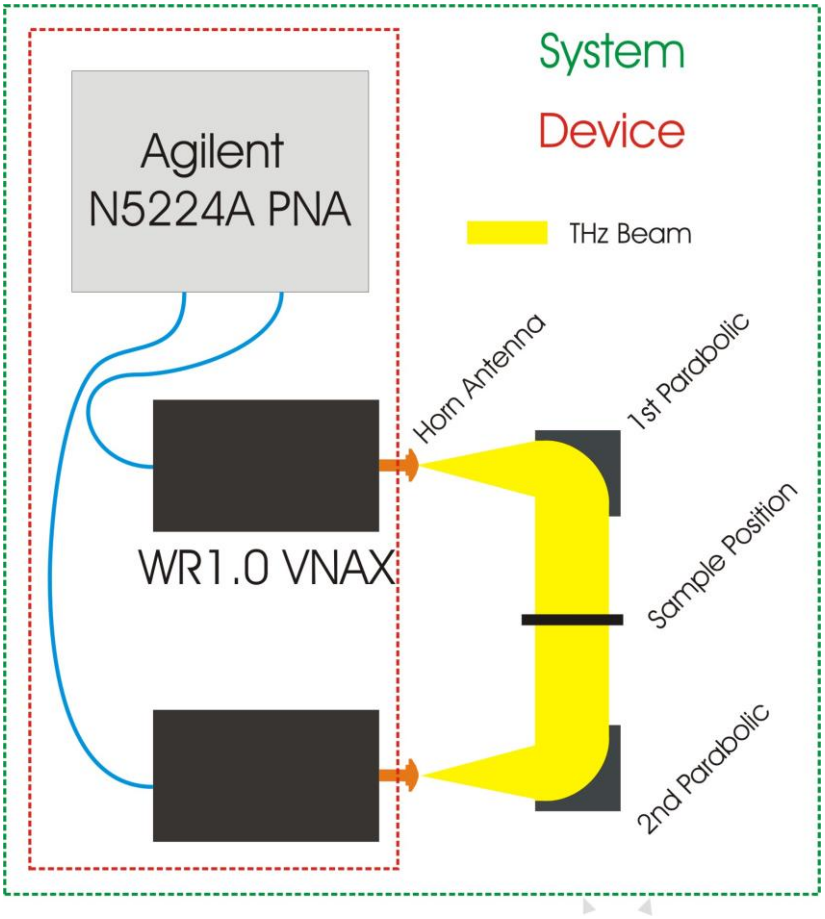

Figure 2.10: Diagram of the THz VNA system and device.

2.2.1 Extension Module Calibration

To calibrate the system losses, from VNA to extension module waveguide end, a standard short, open, load and through method is applied with a Virginia Diodes calibration kit, with a short circuit, a short circuit offset by ¼ wave delay, an absorbing material, and a flush connection as short, open, load and through respectively. This method allows for losses up until the end of the extension modules' waveguides to be accounted for in the VNA

S-parameters. To allow for free space transmission measurements WR1.0H Diagonal Horn antennas with an 11° divergence are added at the end of each extension module waveguide.

To characterise the system, the most important figure of merit for a VNA measurement is the dynamic range. The dynamic range will define the system's SNR over the full frequency measurement range. To obtain the dynamic range a measurement of the noise floor must be compared to that of the system under test conditions. By taking a measurement in free space over the full system range of 750 GHz to 1.1 THz, at 10 Hz RF bandwidth, the noise floor is obtained as shown in Figure 2.11.

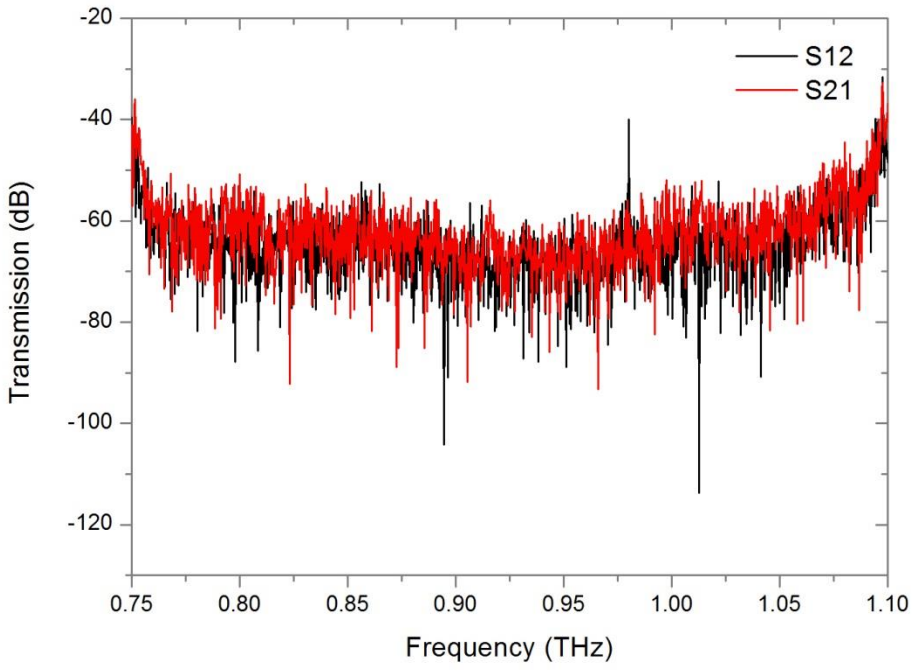

Figure 2.11: Calibrated horn antenna noise floor.

Two 1" parabolic mirrors with 2" focal length are used to collimate and then focus the THz radiation between the two antennas. The transmission losses of the full system are shown in Figure 2.12 without calibration.

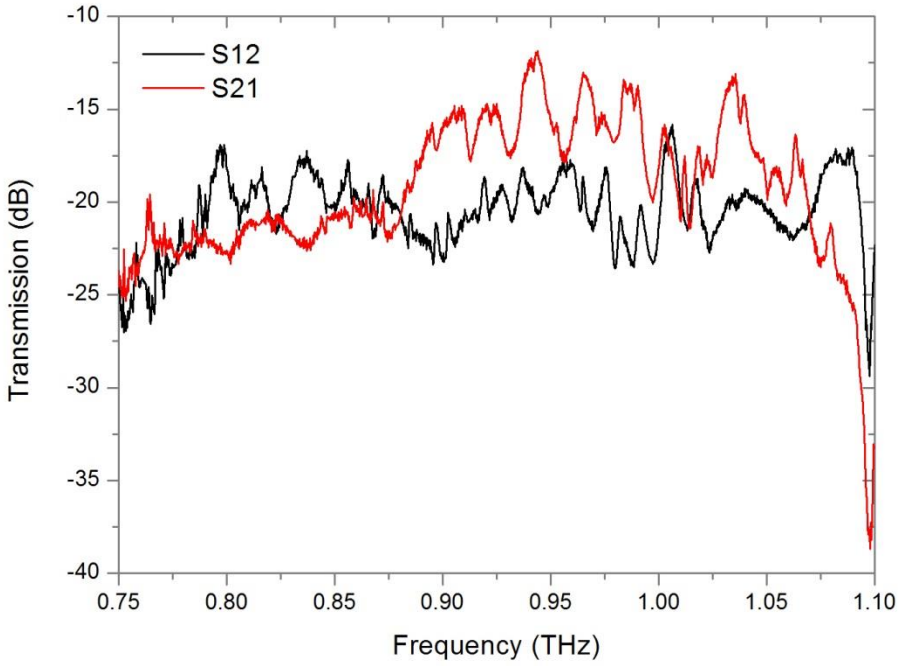

Figure 2.12: S Parameters for horn antenna transmission by two 1" parabolic mirrors.

Figure 2.12 shows the characteristic losses over the full range of the VNA system. The SOLT calibration can account for the losses until the extension module waveguide to horn antenna interface (device). Therefore, applying this calibration provides only the losses from the antennas and free space propagation, as shown in Figure 2.13.

From Figure 2.13, we can see that over the majority of the frequency range we obtain free space and antenna losses ≤6 dB (≤50%). However, these losses quickly increase towards the extreme ends of the measurement range. Atmospheric water absorption can be attributed as the cause of the sharp reduction in transmission close to 1.1 THz: van Exter [22] observed that this absorption line at 1.097 THz is one of three demanding special attention in the THz region.

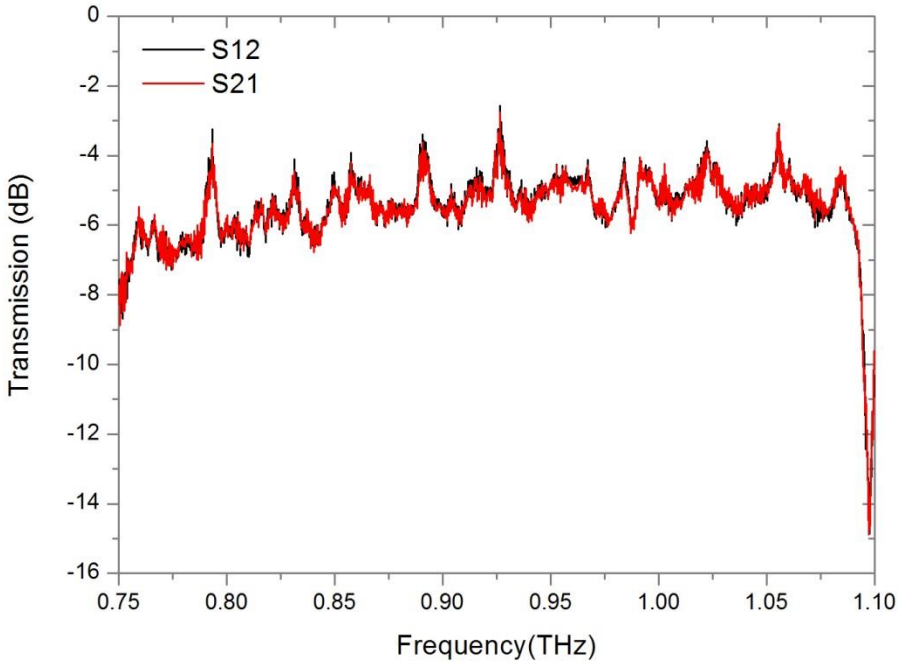

Figure 2.13: Calibrated S Parameters for horn antenna transmission by two 1" parabolic mirrors.

2.2.2. Dynamic Range

With the calibrated free space transmission and noise floor measurements obtained it is possible to calculate the dynamic range of the system. Numerous averaging and statistical approaches exist by which the dynamic range can be defined and can have a large effect upon the figures of merit obtained. No single method of averaging or statistical analyses for the dynamic range, or SNR, has been defined for the THz region. Two methods to define the dynamic range will be applied. The two methods can be considered as a best and worst case definition of the dynamic range, with most manufacturers and users preferring to use the best case when numerically defining the range they have achieved.

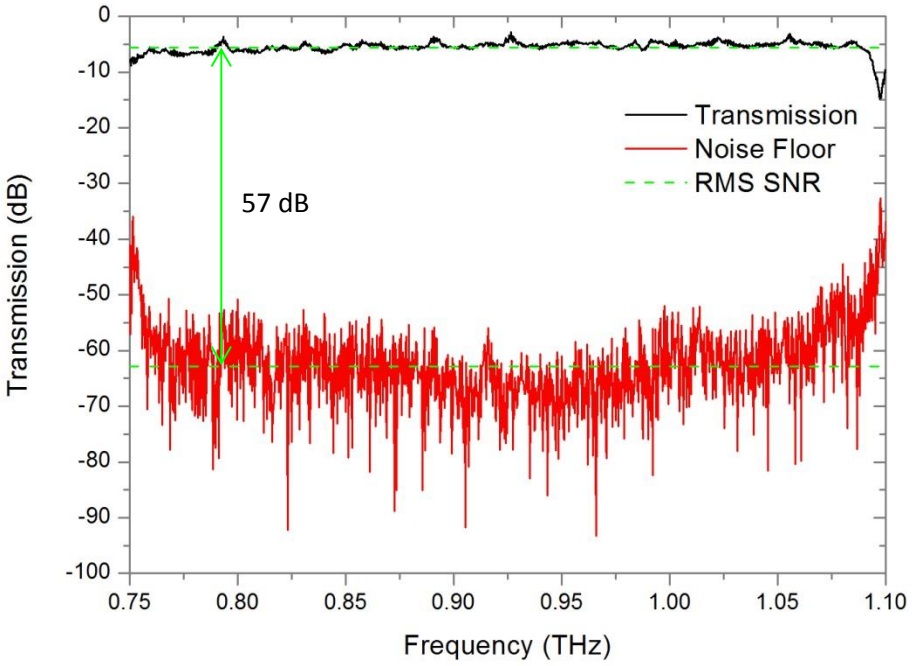

Figure 2.14: RMS Dynamic Range for the full VNA frequency range at 10 Hz IF bandwidth single scan.

Figure 2.14 displays the noise floor and transmission data obtained by a single sweep of the full VNA spectral range. The first method applied to calculate the dynamic range of the system is a calculation of the RMS power of each signal. This method is common in electrical engineering to calculate the average power of a signal. The RMS can be considered as a best case calculation, as a simple comparison of the mean power in each signal does not capture changes in the dynamic range over the spectrum very well.

A more statistical approach to attempt to capture the full difference between the noise floor and transmission data, barring anomalous outliers, is to calculate the mean and variance. For a normally distributed data set, >99% of the data set will lie within three standard deviations, σ, of the mean, μ. The calculation requires conversion from dB to a linear scale before the mean and variance are processed and then conversion back to dB. Instead of calculating the dB difference between the average power of the signals, this approach calculates the dB difference between 99% of Gaussian noise: this is a method to calculate

the lowest SNR over the spectral range rather than the average. It is more accurate to represent a system by its lowest SNR frequency rather than its average SNR over the full range; however it has, in many cases, become common practice to use this numerical value.

The full spectral range of the WR1.0 VNAX shown in Figure 2.14 shows a significant increase in noise floor and reduction in transmission strength at the extreme ends of the frequency range. Reducing the frequency range over which measurements are taken by a small amount can significantly increase the SNR of the system. Taking a frequency range of 0.77 – 1.07 THz largely removes the falling dynamic range experienced at the extreme ends of the full WR1.0 VNAX range. Figure 2.15 shows the RMS dynamic range calculated as previously for this reduced data set.

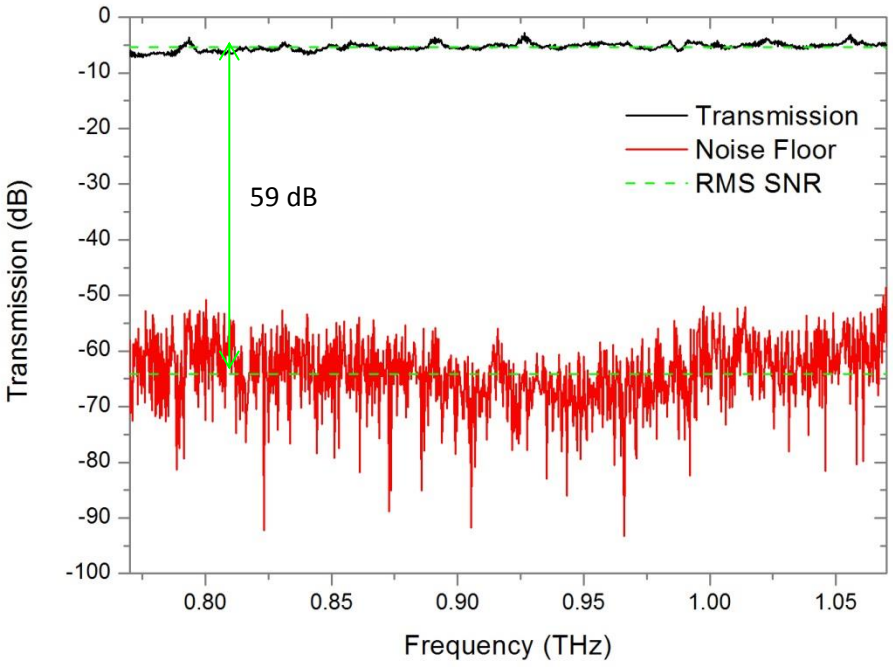

Figure 2.15: Dynamic Range for reduced VNA frequency range at 10 Hz IFBW single scan.

Reducing the frequency range of the data set has little effect upon the RMS dynamic range (+2 dB), but increases the variance in the dynamic range significantly (+10 dB). This, as

previously discussed, is due to the RMS dynamic range having relatively little dependence upon the worst dynamic range in the spectrum. Figure 2.15, however, clearly shows a significantly larger separation between signal and noise floor in the worst case, i.e. the frequency extremes.

Table 2.1 collates the values for noise floor, transmission and dynamic range as calculated by the various means given. Also given is the linear equivalent SNR obtained from the dynamic range in dB. These calculated values are compared to the typical and minimum dynamic range given by Virginia Diodes, Inc, for the WR1.0 VNAX.

Method	***Noise Floor (dB)***	***Transmission (dB)***	***Dynamic Range (dB)***	***SNR***
0.75-1.1 THz RMS	*-63*	*-6*	*57*	*710:1*
0.75-1.1 THz Variance	*-44*	*-9*	*35*	*60:1*
0.77-1.07 RMS	*-64*	*-5*	*59*	*890:1*
0.77-1.07 THz Variance	*-52*	*-8*	*45*	*180:1*
VDI WR1.0 typical	*-*	*-*	*60*	*1000:1*
VDI WR1.0 minimum	*-*	*-*	*40*	*100:1*

Table 2.1. Dynamic Range and SNR calaculated by various methods.

It is apparent from Table 2.1 that the dynamic range achieved by any calculation method does not achieve the typical dynamic range stated for the WR1.0 VNAX device of 60 dB. This dynamic range, however, is taken with a flush waveguide to waveguide configuration; physically aligning the WR1.0 VNAX module waveguides without any free space propagation. The dynamic range given for the system under test, however, also accounts for horn

antenna and free space propagation losses. Free space transmission and antenna losses, which are system specific, are not accounted for in the device's typical dynamic range, which is a measure of the noise floor. In the case of full range RMS noise floor, the obtained 63 dB is above the typical 60 dB given for the WR1.0 VNAX, showing the system is working within specification. It has been made clear that the method used to define the SNR of a system can have a large effect upon the numerical value obtained (710:1 and 60:1) or that using the same method of calculation while slightly limiting the WR1.0 range can significantly increase the worst case (180:1 and 60:1).

Other methods exist which can be used to reduce the noise floor and increase the dynamic range of a VNA signal; e.g. reducing the intermediate frequency (IF) bandwidth, or averaging multiple sweeps. The Agilent N5224A PNA provides control over the filter bandwidth applied during the down-conversion (intermediate frequency) at the receiver chain. A smaller IF bandwidth allows for a higher IF gain before measurement of the signal by the analogue-to-digital converter. The noise floor measured by the VNA receiver is caused by thermal noise in the analyser's receiver chain, directly proportional to the IF bandwidth [34];

$$\mathrm{P}_n = \mathrm{kTB} \qquad \textbf{(2.6)}$$

Where P_n is the noise power, k is Boltzmann's constant, T is the absolute temperature in K, and B is the receiver bandwidth in Hz.

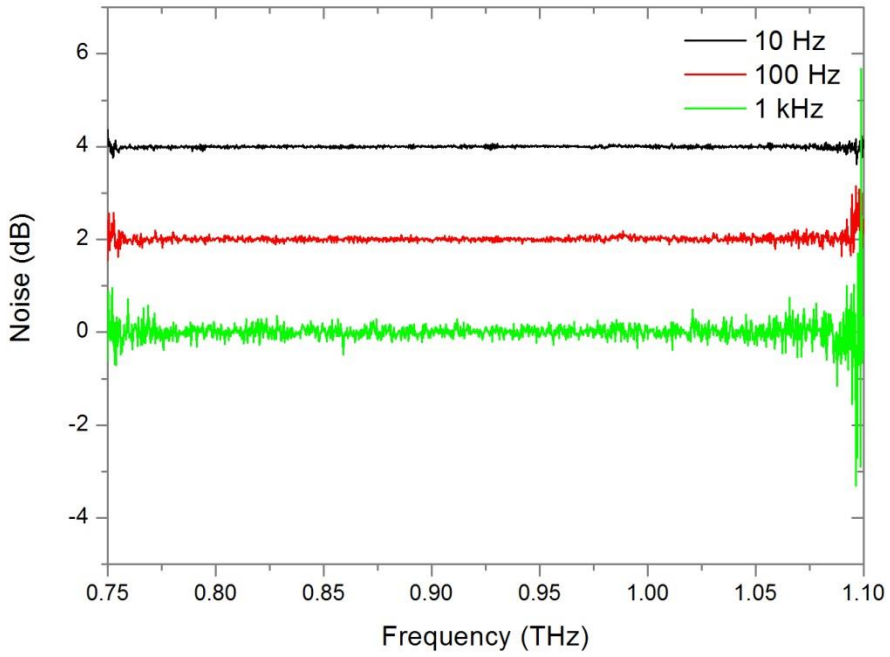

Figure 2.16: Noise in normalised transmission for horn antenna transmission by two 1" parabolic mirrors at varied IF bandwidth, offset by 2dB for clarity.

Point by point normalisation of the transmission by a previous transmission signal is a method by which the noise over the spectral range can be visualised with minimal calculation. Figure 2.16 shows the effect of varying the IF bandwidth upon a normalised two parabolic free space transmission. The low level noise that is present in the analyser's receiver chain is caused by thermal noise; therefore, it is directly proportional to bandwidth [35]. Figure 2.16 shows the effect of increasing the IF bandwidth upon the normalised signal, with 100 Hz and 10 Hz offset by 2 and 4 dB, respectively. The increased noise level at the extreme ends of the frequency range is apparent in all three traces of Figure 2.16, with significantly increased noise across the entire spectrum as the IF bandwidth is increased. A ten-fold increase in IF bandwidth provides a 10 dB reduction in the noise floor; however, it incurs an almost ten-fold increase in scan time. Multiple scan averaging of a coherent signal with uncorrelated noise will cause the noise component to approach zero [35]. VNA

averaging of multiple scans achieves a similar improvement to the noise floor as increasing the IF bandwidth with a similar, marginally higher, increase in total scan time.

The SNR ratio achieved by a two parabolic free space arrangement single scan at 10 Hz IF bandwidth over the range of 0.77 – 1.07 THz has been considered to be the best compromise between scan time, scan range and noise level. A significantly higher dynamic range can theoretically be obtained by further decreasing the IF bandwidth or averaging multiple scans; however, a true measure of the SNR of the data presented in this thesis is that obtained under the conditions presented. Using a statistical approach a worst case SNR of 180:1 has been defined, however, this same data set is defined in the VDI specifications by its RMS noise value of 890:1.

2.3 Conclusions

The details of two different systems capable of measuring THz transmission profiles have been presented. The principles of operation for each system are largely different as are their relative figures of merit;

THz-TDS	***VNA***
Broadband (0.1-3.0 THz)	*Narrowband (0.7-1.1 THz)*
Pulsed	*CW*
450:1 RMS SNR	*890:1 RMS SNR*
25 GHz Frequency Resolution	*0.5 GHz Frequency Resolution*
30 min/measurement	*2 min/measurement*
Time domain measurement	*Frequency domain measurement*
Requires normalisation	*Normalisation applied by VNA*

Table 2.2. Comparison of THz-TDS and VNA measurement systems.

While the VNA system outperforms the THz-TDS system in most figures of merit, the THz-TDS remains a useful tool due to its larger bandwidth and the information provided by a

pulsed time domain response. The usage of both systems throughout the investigations of this thesis provides a powerful tool for observing resonant features over both a broad frequency range and at high frequency resolution.

Chapter 3

Surface Plasmons

Since the first demonstration of Extraordinary Optical Transmission (EOT) [14] in 1998 the role of surface plasmons in the transmission properties of subwavelength apertures has received renewed interest; in particular with, the ability to control and manipulate surface plasmon resonances by the design of periodic features. The existence of 'spoof' surface plasmons in the terahertz (THz) region relies upon this ability to manufacture a plasmonic response below a metal's plasma frequency.

This chapter provides a detailed background to the fundamental principles of surface plasmons. The numerous modes that exist for both ideal and real dielectric boundary conditions in various frequency regimes and fields of research creates a plethora of terms including, but not exclusive to; surface plasmons (SP), surface plasmon waves, surface plasmon polaritons (SPP), Zenneck and Sommerfeld waves, with the prefixes of propagating,

localised and spoof adding further complexity. The definition and use of these terms has not always been consistent over the various frequency regimes and research disciplines. This chapter will first look to establish a consistent terminology which will be used throughout. The various mechanisms that have been exploited to excite and utilise surface plasmons will be discussed, deriving where possible the properties of surface plasmons from first principles. Finally, a summary of the work on surface plasmons and EOT in the THz regime serves to provide a context for the work.

3.1 Formal Definition

The term plasmon was first introduced by Pines [36] to describe the elementary excitation associated with valence electron oscillations. This original definition is still valid. However, the use of the term plasmon has evolved since its initial usage, and it is now used in a much broader context. A more general definition of a plasmon can be given as “a quantum quasi-particle representing the elementary excitations, or modes, of the charge density in a plasma” [37]. Pines [36] used the term plasmon while discussing energy losses in solids; a plasmon is always highly interacting due to its existence in the free electron gas and is therefore ‘lossy’. It is for this reason that a plasmon is referred to as a ‘quasi-particle’.

When an electromagnetic (EM) wave propagates in an optically responsive medium, it excites the internal degrees of freedom of the medium, typically bound electrons. The resulting particle is no longer a photon as it shares its energy with the medium, creating a polariton. The optical response of a metal in the visible and infrared is dominated by the free-electron plasma. Therefore, electromagnetic waves in a metal are called plasmon-polaritons.

When an EM wave is incident upon a metal thin film it is possible to excite a plasma mode which propagates along the metal/dielectric interface. These longitudinal charge density oscillations, called surface plasmons, cannot exist without an associated transverse EM wave. Such a coupled wave, which shares its energy between a photon and plasmon coupled at the interface, is known as a surface plasmon-polariton (SPP). These hybrid surface modes are characterised by an evanescently decaying field perpendicular to the surface, existing either side of the boundary interface. The confinement and lifetime of the SPPs is bound to the dielectric properties of both the metal and the neighbouring dielectric, making them highly sensitive to changes at the boundary.

SPPs can be visualised as a ripple propagating through the free electrons close to the surface of a metal. These oscillations establish an electric field which propagates along the surface. This electric field decays exponentially both into the metal and the dielectric, as shown in Figure 3.1. In an ideal (loss free) conductor, this propagation would continue infinitely. However, in a real metal, electron scattering causes damping, limiting the lifetime.

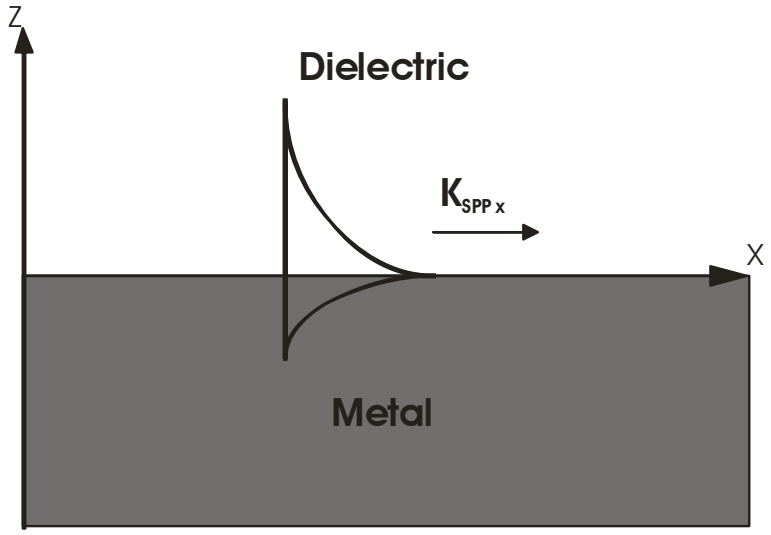

Figure 3.1: SPP electric field at metal-dielectric interface.

The exploitation of the sensitivity of SPPs to surface roughness and dielectric properties in spectroscopy has led to Surface Plasmon Resonance [13] and Surface Enhanced Raman Spectroscopy [38] becoming well established techniques. However, the work presented in this thesis is far more concerned with the role of SPPs in the phenomenon of EOT, particularly at THz frequencies. This topic will be explored in greater detail later in this chapter. However, the origin of SPP excitation and propagation must first be studied, beginning in the optical region and progressing to THz frequencies.

3.2 Origin of SPP Modes

For a complete understanding of SPPs, we must begin from first principles. Doing so allows us to begin with the simple case of light propagating in the x-direction (as defined in Figure 3.1) along a surface, where the electromagnetic wave is defined by its wavevector, relating to its wavenumber, k_x. The energy, E, of such a surface wave can be expressed as:

$$E = \hbar 2\pi v = \hbar\omega = \hbar c k_x \qquad (3.1)$$

Here, c is the speed of light in a vacuum, v is the frequency of oscillation in Hz and ω is the angular frequency in radians, $\hbar$ is the reduced Planck's constant. This dispersion relation describes how the energy and momentum of light in a vacuum are related. SPPs, as has been previously established, exist at the interface between a metal and dielectric and, therefore, do not follow this simple relationship. The permittivity, ϵ, experienced by an SPP at the interface between a metal and a conductor can be approximated by [39]:

$$\epsilon = \frac{\epsilon_m \epsilon_d}{\epsilon_m + \epsilon_d} \qquad (3.2)$$

Here ϵ_m and ϵ_d are the permittivities of the metal and dielectric, respectively. The permittivity of a medium determines the velocity of light passing through it. SPPs follow the more complex dispersion relation given in equation (3.3) due to their reduced velocity when compared to that in a vacuum. Due to the anisotropic nature of the medium, the dispersion for both parallel (k_{SPP_x}) and perpendicular (k_{SPP_z}) to the interface must be separately considered:

$$k_{SPP_x} = \frac{\omega}{c}\left(\frac{\epsilon_m \epsilon_d}{\epsilon_m + \epsilon_d}\right)^{\frac{1}{2}} \quad \textbf{(3.3a)}$$

$$k_{SPP_{z,d}} = \frac{\omega}{c}\left(\frac{\epsilon_d^2}{\epsilon_m + \epsilon_d}\right)^{\frac{1}{2}} \quad \textbf{(3.3b)}$$

$$k_{SPP_{z,m}} = \frac{\omega}{c}\left(\frac{\epsilon_m^2}{\epsilon_m + \epsilon_d}\right)^{\frac{1}{2}} \quad \textbf{(3.3c)}$$

Here the permittivity of the metal, ϵ_m, is complex and varies with frequency. Surface waves can be characterised to exist as a number of different modes under differing dielectric conditions of the conductor [40]. The Drude model, discussed in section 3.5, can be used to approximate the complex dielectric function of the metal conductor.

Three types of SPP mode can exist at a dielectric/conductor interface assuming $\epsilon_d > 1$. The solutions to equations (3.3) are evaluated for a perfect lossless metal, $\Im(\epsilon_m) = 0$, in Table 3.1, adapted from [37], where $\Im(\epsilon_m)$ is the imaginary component of the metal's dielectric function.

Mode	$\Re(\epsilon_m)$	k_{SPP_x}	k_{SPP_z}
Brewster Modes	*> 0*	*Real*	*Real*
Localised SPPs	$0 > \Re(\epsilon_m) > -\epsilon_d$	*Imag*	*Real*
Propagating SPPs	$-\epsilon_d > \Re(\epsilon_m)$	*Real*	*Imag*

Table 3.1: Types of EM modes existsing at a metal-dielectric interface for a lossless metal.

Brewster modes exist for $\Re(\epsilon_m) > 0$, where $\Re(\epsilon_m)$ is the real component of the metal's dielectric function. Not considered a true surface plasmon, these modes radiate in both k_x and k_z. These modes exist above the metal's plasma frequency, ω_p, as discussed in 3.5 and are not encountered at THz frequencies for metal-dielectric interfaces.

Localised SPPs are a non-propagating surface wave, due to the imaginary nature of k_x. For a lossless metal the energy is radiated away from the surface by the real k_z component. However, for a real metal, such modes become evanescent due to the complex solution to k_z.

The mode we are most interested in for this thesis is that of 'propagating SPPs', which exist when $-\epsilon_d > \Re(\epsilon_m)$. For this case, both $k_{z,m}$ and $k_{z,d}$ decay evanescently perpendicular to the surface due to their purely imaginary nature. The non-zero $\Re$ value of k_x describes the propagation of the surface wave. For a real metal, the complex nature of the dielectric function leads to a non-zero imaginary component of k_x, resulting in the propagating wave experiencing damping. It is these losses (due to electron collisions) that limit the distance that an SPP can travel.

3.3 Excitation of SPPs

The dispersion relation given in equation (3.3a) relates the wavenumber, k_{SPP_x}, to the frequency of oscillation, ω, for a propagating SPP, as displayed in Figure 3.2.

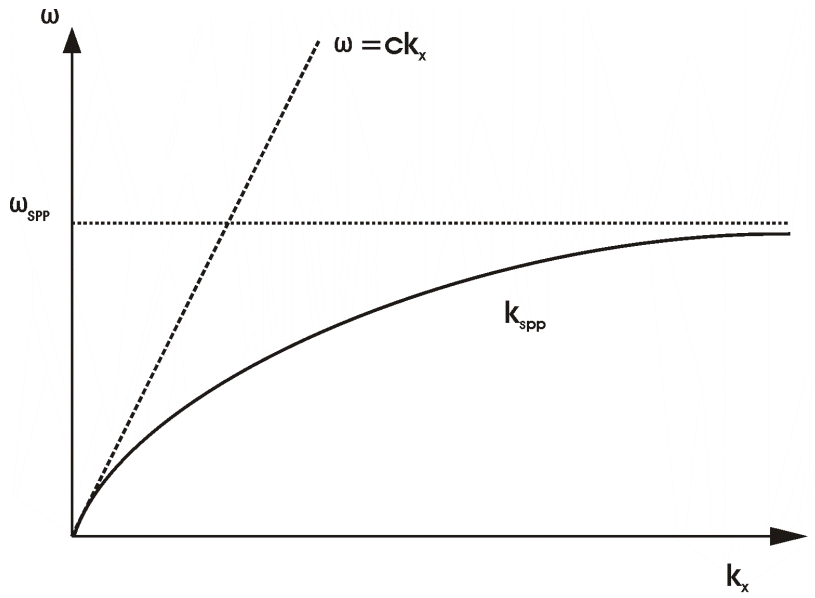

Figure 3.2: Dispersion relation for propagating SPPs. Free space photons exist to the left of the light line, propagating SPPs to the right; this momentum mismatch must be overcome to excite SPPs.

In order to excite an SPP by a photon incident upon a metal/dielectric boundary from the dielectric medium, two properties of the incident photon must be matched to that of the SPP mode; the frequency, and the component of the wavenumber parallel to the surface, k_x. The first condition is easily satisfied; however, as can be seen in Figure 3.2, the SPP wavenumber is larger than the wavenumber of the light in the adjacent dielectric. Thus, photons incident on a metal surface cannot directly couple to SPPs from free space without a mechanism to overcome the momentum mismatch. The photon and SPP wavenumber can be matched by using either total internal reflection geometry (TIR) (Kretschmann and Otto configurations) or diffraction effects.

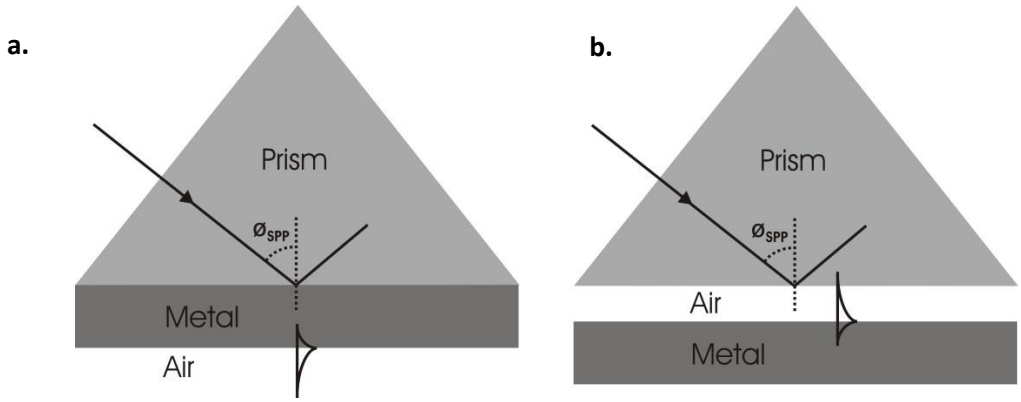

Figure 3.3: a. The Kretschmann and b. Otto configurations for launching propagating SPPs at a metal-dielectric interface.

In the Kretschmann configuration, Figure 3.3a, a metal film is illuminated through a dielectric prism at an angle of incidence which is greater than the critical angle for TIR to occur [41]. The wavenumber of light is increased in the more optically dense medium, which can be visualised by a further dispersion relation shown in Figure 3.4. At an angle of incidence at which the in-plane wavenumber, k_x, of the photon in the prism matches the SPP wavenumber, k_{SPP_x}, for the metal/dielectric boundary, a propagating SPP is excited at the far metal-dielectric boundary with almost 100% efficiency [42].

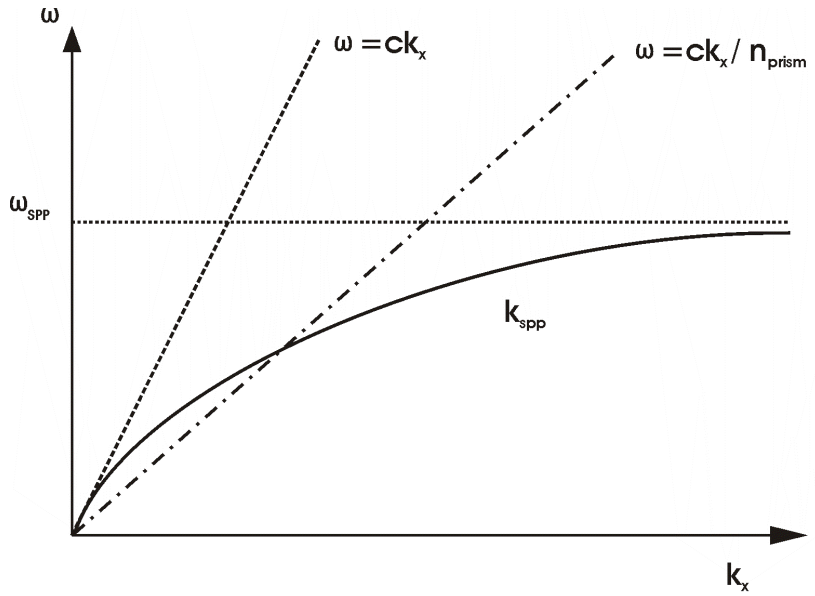

Figure 3.4: Dispersion relation for propagating SPPs. Free space photons exist to the left of the light line, propagating SPPs to the right; this momentum mismatch must be overcome to excite SPPs.

The Kretschmann configuration relies upon resonant light tunnelling through the metal film, and therefore efficiency decreases with increasing metal film thickness. For thick metal films, in which the Kretschmann configuration cannot be used, SPPs can be excited by the Otto configuration, as in Figure 3.3b. In the Otto configuration, the prism is placed in close proximity to the metal surface so that photon tunnelling occurs through the air gap between the prism and the surface [43]. The resonant conditions for propagating SPP excitation are similar to those in the Kretschmann configuration.

Another way to overcome the momentum mismatch between the incident photons and the available SPP modes is to use diffraction effects. If a diffraction grating is created on an otherwise smooth metal film, the components of the diffracted light whose wavenumbers match those of the propagating SPP mode will be coupled to the surface [39]. Depending on the metal film thickness and grating size, SPPs can be excited upon both interfaces of the metal film.

Similar conditions can be met by a randomly rough surface. A randomly rough surface will provide diffracted components of light with all wavenumbers, allowing SPP coupling to an otherwise un-engineered surface [39]. The coupling of light to SPPs in this manner, however, has an ill-defined resonance and low efficiency.

3.4 Losses and Decay Length

Once excited, a propagating SPP will become trapped at the conductor-dielectric boundary. The field decays evanescently from the surface into both media, and if absorption losses are neglected, SPPs will propagate indefinitely.

Losses in the propagating SPP are incurred by damping. Mathematically, dampening arises due to the complex nature of the permittivity in a real metal, resulting in a complex k_{SPP_x}. An excited SPP on a real metal possess a real ω and complex k leading to an evanescent wave with limited propagation, from [39];

$$k_{SPP_x} = k'_{spp_x} + ik''_{spp_x} \quad \textbf{(3.4)}$$

Here, the real component of the wavenumber corresponds to the wavelength of the plasmon, $\lambda_{SPP} = 2\pi/k'_{spp_x}$, whilst the imaginary component represents resistive losses in the metal. If, as for metals in the optical regime, $|i\epsilon_m| \ll |\epsilon_m|$ and the dielectric material is real, equation (3.3a) can be approximated for a real metal, from [39];

$$k'_{spp_x} \approx \frac{\omega}{c}\left(\frac{\epsilon'_m \epsilon_d}{\epsilon'_m + \epsilon_d}\right)^{\frac{1}{2}} \quad \textbf{(3.5a)}$$

$$k''_{spp_x} \approx \frac{\omega}{c}\left(\frac{\epsilon'_m \epsilon_d}{\epsilon'_m + \epsilon_d}\right)^{\frac{3}{2}} \frac{\epsilon''_m}{2\epsilon'^2_m} \quad \textbf{(3.5b)}$$

If the losses are small, for $\epsilon''_m \ll 2\epsilon'^2_m$, the propagation distance can be much greater than the wavelength of the SPP, which is often the case in the THz region.

The confinement of an SPP is determined by the penetration of its electric field into each of the media at the boundary. The decay length of an SPP in the dielectric is of the order of $\lambda/2$, while the decay length into the metal is determined by skin depth. Both the propagation distance and confinement are strongly dependent upon SPP frequency.

3.5 Optical Response of a Metal

Metals such as Au and Cu have different optical properties from standard dielectrics. Phenomena including the reflection of visible wavelengths, as well as good electrical and thermal conduction, all have a root in conduction band free electrons. The delocalisation of free electrons against a crystal lattice of positive ions forms a free electron plasma. It is the manner in which this plasma reacts to external EM radiation which determines a metal's optical properties.

The Drude model is a simple yet accurate model to predict the optical response of metals over a range of frequencies. Its derivation is repeated in many textbooks; however, it will be detailed here for reference and discussion of its implications. The model is based upon the formulation of the Coulomb interactions between the free electron plasma and the positive crystal lattice. The plasma frequency, ω_p, describes the natural oscillation frequency of the free electron plasma in a bulk metal:

$$\omega_p = \sqrt{\frac{ne^2}{\epsilon_0 m_e}} \qquad \textbf{(3.6)}$$

Here, e and m_e are the charge and effective mass of an electron respectively, n is the carrier density and ϵ_0 is the permittivity of free space. The high electron densities in metals result in plasma frequencies residing in the UV part of the spectrum. The Drude model describes the optical response of the plasma to an external source [44];

$$\epsilon(\omega) = 1 - \frac{\omega_p^2}{\omega^2 - i\gamma_0\omega} \qquad \textbf{(3.7)}$$

Where ω_p is the plasma frequency, ω is the frequency of the incident radiation and γ_0 is the damping coefficient associated with the collision of free electrons with the crystal lattice.

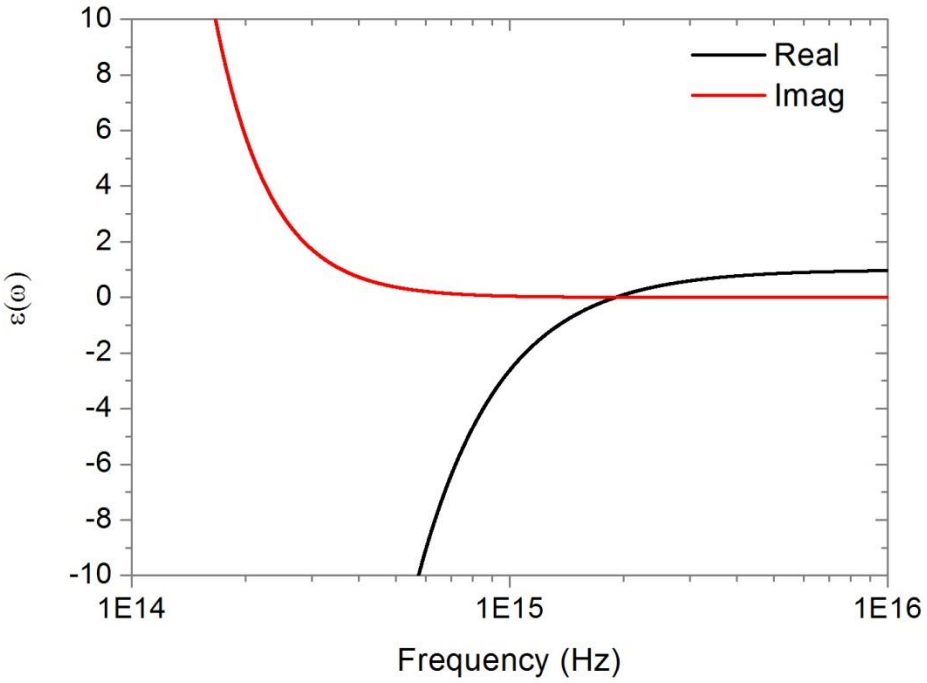

Figure 3.5: Drude model for Au (data extracted from [44]*).*

It can be seen from Figure 3.5 that Brewster Modes, $\Re(\epsilon_m) > 0$, exist above the metal's plasma frequency, ω_p, which for Au is ≈ 2 PHz and exists in the ultraviolet region of the spectrum. For $\omega < \omega_p$, as in the visible region, metals possess a small negative real and positive imaginary component. As $\omega \ll \omega_p$, as in the THz region, both the real and imaginary dielectric components increase in magnitude due to the ω_p^2/ω^2 term in equation (3.7).

3.6 Extraordinary Optical Transmission

The work of Bethe [45] derives the optical transmission through an ideal sub-wavelength aperture existing in an infinitely thin, perfectly conducting substrate. The transmission efficiency, η_B, of such an aperture is derived as:

$$\eta_B = \frac{64\,(\frac{2\pi r}{\lambda})^4}{27\pi^2} \qquad \textbf{(3.8)}$$

Here, λ is the wavelength of the incident light and r is the radius of the aperture. It can clearly be seen from this expression that the transmission efficiency of such a hole is governed by the relation $\left(r/\lambda\right)^4$. Since the work of Bethe, classical optics has considered sub-wavelength holes to be highly inefficient for the transmission of radiation. An important finding by Ebbesen [14] in 1998 reported that, through the periodic arrangement of apertures, a hole transmission efficiency far in excess of that predicted by Bethe was achievable. In fact, more radiation was transmitted than was incident upon the free-space apertures. This phenomenon was termed EOT and began much renewed interest in the area of sub wavelength holes. The exact mechanism by which SPPs can be excited by an array of sub-wavelength apertures is still under investigation [46] [47], that they play an important role in EOT is, however, generally accepted.

The reporting by Wood in 1902 of the discovery of dark bands in the reflection spectrum of a metallic grating is arguably the first experimental discovery of SPPs excited by a metallic grating [48].

Rayleigh was the first to propose an explanation of the phenomena observed by Wood [49]. Rayleigh predicted the existence of Wood's anomalies at wavelengths for which light is scattered by a 1D grating tangentially to the grating surface.

However, Strong later showed that the shape and position of Wood's anomalies are dependent upon the grating metal, something which Rayleigh's grating formula cannot account for [50]. Strong also investigated changing the width of the grating, finding that the

anomalies became stronger as the width approached the incident wavelength. Fano was the next to make a significant breakthrough in the interpretation of Wood's anomalies [51]. Fano's interpretation of the experimental data showed that two distinct types of anomaly can be distinguished; a sharp feature at a well-defined wavelength, as predicted by Rayleigh's grating formula, and a diffuse feature extending to the red from the first created by a 'forced resonance' of 'leaky waves' supported by the grating. It is these leaky waves which we now know as SPP's.

Since the initial work of Ebbesen, there has been a renewed interest in one and two-dimensional sub-wavelength apertures in an attempt to characterise the experimental and theoretical aspects of EOT. These studies cover a wide range of the EM spectrum and employ various experimental and analytical approaches. However, a unified theory detailing the nature of EOT in metal aperture arrays still does not exist. Whilst most works agree that SPPs play a vital role in this anomaly, the precise nature of transmission through a subwavelength aperture array is still debated [46] [52] [53] [54].

3.7 THz Surface Plasmons

At THz frequencies, far from their plasma frequency, metals possess large real and imaginary permittivity. At 1 THz, Au has been measured to possess a $\Re(\epsilon_m)$ = -8.62 x 10^4 and $\Im(\epsilon_m)$ = 6.2 x 10^5 [55]. For a gold-air interface at 1 THz the resultant SPP propagation length can be calculated to be 30 m, 10^5 times longer than its wavelength [56]. This propagation length arises from the weak confinement, 40 nm [56], of the SPP into the metal.

Since the work of Pendry [15] proposed the ability to alter the effective permittivity of a metal perforated with holes and allow the confinement of SPPs with 'almost arbitrary

dispersion in frequency and in space', the possibility to manipulate SPPs at THz frequencies has become a reality. These 'metamaterials', a metal surface perforated with subwavelength features, are able to support and confine 'spoof' SPPs. Incident radiation is insensitive to individual features on a subwavelength scale and, instead, experiences a combined metal-dielectric layer as a single effective medium [57]. Pendry noted that, by patterning the surface of metals which can already support surface plasmon modes, the penetration into the metal will be increased and the frequency of the existing plasmon lowered. For this case, 'it is hard to distinguish between the 'real' and the spoof surface plasmons as they merge one into the other' [15]. It is from this problem that much of the ambiguity in language surrounding THz SPPs arises.

The work of Pendry allows for the manipulation of SPPs in the THz region as long as two requirements are met i) a launch mechanism which can provide the necessary in-plane momentum to excite SPPs, and ii) a patterned surface with which they can be confined. The existence and measurement of SPPs at THz frequencies has been well established in the past decade under numerous geometries.

Excitation by a razor blade brought close to the metal surface [58] [59] is achieved more easily at THz frequencies than in the optical regime due to the wavelength-scale separation required for efficient SPP coupling. The spacing between the surface and the razor edge acts as a diffraction point providing the in-plane momentum, and inversely as a point at which to de-couple SPPs back into free space. Prism coupling methods similar to those in the optical regime have been shown to excite SPPs in the THz [60] and microwave [61] regions.

Sub-wavelength periodic features have been shown to be able to act as both the coupling method and enhance the confinement of THz SPPs. Bulls-eye apertures have become well established in the THz regime for near-field imaging, comprising a single aperture flanked by sub-wavelength periodic corrugations [62]. Each sub-wavelength corrugation has been shown to act as a launch mechanism for an SPP which will arrive at the aperture with temporal separation caused by spatial separation [63]. Transmission through the aperture has been enhanced by corrugations on both the front and back interfaces [64], and changes to the aperture shape [65]. THz SPPs have been directly observed at the centre of a bulls-eye structure, coupled only by corrugations in the metal surface from normal incidence collimated THz radiation [66].

The first demonstration of enhanced transmission through a metal sub-wavelength aperture array at THz frequencies was conducted by Qu et al. [21]. Lithographically patterned aluminium aperture arrays on high resistivity silicon substrates displayed SPP resonances at both the metal-air and metal-silicon interfaces. Sharper resonances have been observed for the case of free standing metal aperture arrays [67]. This is attributed to the increased coupling between the SPPs on the front and back of the array.

Many works have been undertaken to find the optimum conditions for SPPs in two-dimensional aperture arrays at THz frequencies. With many degrees of freedom available in the design and optimisation of such arrays it is unsurprising that, in most cases, each feature is varied in isolation. This approach, though necessary, has led to a fragmented understanding of the physical principles governing EOT. The degrees of freedom in a two-dimensional aperture array include, but are not exclusive to, aperture shape [16] [68] [69] [70], dimensions [71] [72], periodic lattice [73] [74], and film thickness [75]. Again, it is

important to note that THz SPPs have been observed in free standing metals perforated with sub-wavelength holes excited by normal incidence THz radiation [76] and no additional coupling mechanism is required.

3.8 Rectangular Sub-Wavelength Apertures

Early investigations into the phenomena of EOT in both the THz [68] and optical [77] [78] regions showed that rectangular holes exhibit higher transmission than square or circular holes with the same area. This increased transmission has strong polarisation dependence for rectangular and elliptical holes, requiring the longer aperture dimension to be perpendicular to the incident radiation electric field polarisation.

The work of García-Vidal [79] proposed that a single rectangular aperture supports enhanced transmission when compared to that of a square aperture of the same area, dependent upon aspect ratio. As the aperture width, a_x, is reduced for a fixed aperture length, a_y, the transmission normalised to area increases for a wavelength ≈ $2a_y$. This theoretical work is considered frequency independent and linearly scalable to any wavelength.

Ruan [80] continued to investigate the role of high aspect ratio sub-wavelength rectangular slot apertures in transmission spectra. By describing the rectangular hole dominated transmission as a 'localised wave-guide resonance' and attributing it to the cut-off frequency of the basic mode (TE_{10}) in a rectangular waveguide, given by (3.9);

$$\mathrm{f}_r = 0.5\,(^{c}/_{a_y}) \qquad \textbf{(3.9)}$$

Where f_r is the resonant frequency, c is the speed of light and a_y is the long aperture edge length, as shown in Figure 3.6.

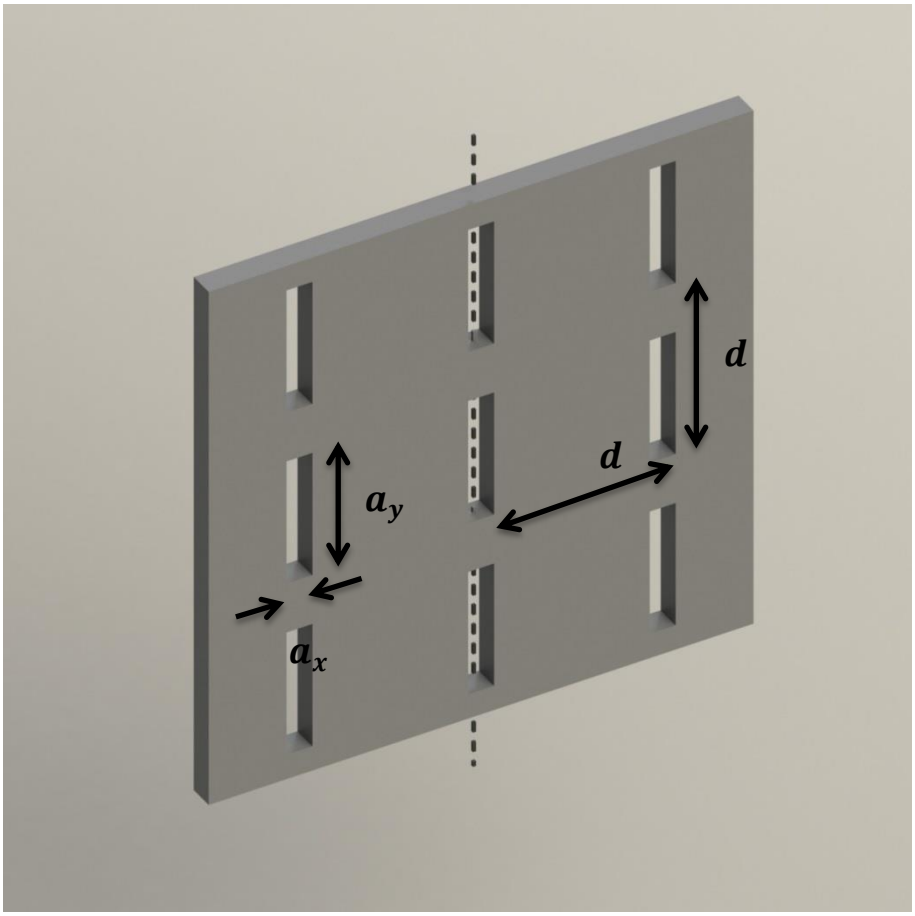

Figure 3.6: Rectangular sub-wavelength aperture array.

Ruan [80] remarks that 'this resonant frequency is almost independent of the periodicity' for the case of a square lattice periodicity equal to 1.11, 1.22 and 1.33 a_y. The second resonant peak observed by Ruan is well described by the concept of a spoof SPP. The resonant frequencies are a function of the lattice constant, and the first resonant frequency is defined by;

$$f_r = (c/d) \quad \textbf{(3.10)}$$

Where f_r is the resonant frequency, *c* is the speed of light and *d* is the square lattice constant.

Continued experimental studies on the transmission spectra of arrays of rectangular sub-wavelength apertures in the THz regime look to manipulate the periodic lattice [81], aperture width [82], aperture length [83] and aspect ratio [84] in an effort to control and enhance EOT.

3.9 Conclusions

The origin of EOT at optical frequencies is believed to lie in the excitation of SPPs. When moving to the THz regime the plasma frequency of metals can no longer support 'real' SPP modes. However, the significant work of Pendry [15] allows for the control and confinement of THz 'spoof' SPPs. Spoof SPPs have been observed under various experimental geometries including normal incidence radiation with no coupling method beyond the sub-wavelength features provided. Further experimental and theoretical work in both the optical and THz regions observe increased transmission and in-hole field enhancement for arrays of rectangular apertures over square or circular apertures. This increased transmission can be attributed to the existence of a resonant mode in a single sub-wavelength aperture, dominated by its length, often referred to as a 'localised resonance'.

The experimental work in this thesis is conducted on metal foils in the THz region; for this case, any discussion of SPPs can be considered to be 'spoof'. The work of this thesis is primarily based around the interaction between the 'localised' slot resonance, with an origin in aperture dimensions, and 'spoof' SPPs, with an origin in the periodic lattice spacing.

Chapter 4

Finite-Difference THz Simulations

The finite-difference time-domain (FDTD) method is one of the most common time domain numerical techniques to solve problems in electromagnetics. Although able to solve many anisotropic and non-linear systems, the FDTD method is, however, computationally intensive. For this reason, FDTD is best employed when the characteristic dimensions of the domain are of the same order as the wavelength. If an object is very large compared to the wavelength many more efficient methods are available which do not require the memory of such a large FDTD simulation.

FDTD simulations have been used to model semiconductor [85] and metal aperture transmission in the THz [86] and optical [87] regions, and 'real' [88] and 'spoof' [89] surface plasmon polaritons (SPPs) in metamaterials. Publications significant to the current study

include that of THz transmission through metal hole arrays attributed to the coupling of SPPs [90] and the increased confinement of THz SPPs by a structured metal surface [59].

This chapter will present examples from the non-commercial FDTD solver, Lucifer, under continued development at Durham University by Claudio Balocco. The increased level of control provided by a non-commercial simulation allows for direct manipulation of the simulation parameters not usually provided by most commercial simulation packages. This level of control, however, requires careful selection of these parameters, requiring an increased level of understanding of the FDTD simulation technique by the user. Lucifer provides full control over the simulation geometry, source and monitor planes, boundary conditions, and dielectric properties.

4.1 Introduction to FDTD

The FDTD simulation results presented throughout this thesis use the same algorithm first proposed by Yee [91]. The Yee algorithm replaces Maxwell's equations with a set of second-order finite difference equations, and then iteratively solves for future magnetic and then electric fields given the currently known electric and magnetic field at adjacent nodes, Figure 4.1. There has been no change in the implementation of FDTD simulations since Yee's first demonstration. However, a significant increase in computing power has allowed for much larger systems to be modelled fully.

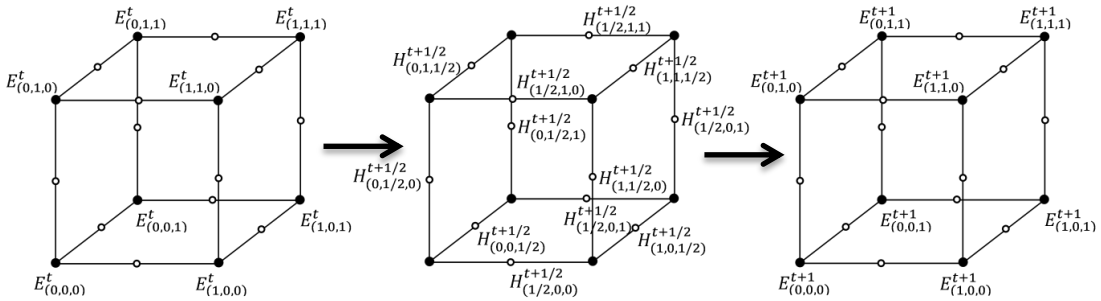

Figure 4.1: Iterative FDTD solving method of a single full timestep. Knowledge of the electric field at t allows for calculation of the magnetic field between nodes at t+1/2, which in turn provides the electric field at t+1.

4.2 Numerical Limitations

Any computer based simulation will introduce numerical artefacts due to a finite number precision. The FDTD algorithm by extension is an approximation of Maxwell's equations to a second-order difference, discounting all higher order terms. However, far more important than the approximations inherently incurred by the implementation of a computer simulation is an FDTD systems' ability to provide a numerical solution which is wrong. That is, just because a numerical solution can be obtained for a given set of conditions and parameters does not necessarily indicate whether or not the result is correct.

One such user defined value which can result in an incorrect numerical solution if not correctly chosen is the courant number, S_c, which can be defined as;

$$S_c = \frac{c\Delta t}{\Delta x} \qquad \textbf{(4.1)}$$

Where c is the speed of light in free space, Δt is a single time step and Δx is a single spatial step. Due to each node being a function of only its next neighbours at each update step, it is required that energy cannot propagate further in a single time step than a single spatial step. Therefore;

$$c\Delta t \leq \Delta x \qquad \textbf{(4.2)}$$

for 1D problems eq. 4.1 and 4.2 combine simply to give;

$$S_c = \frac{c\Delta t}{\Delta x} \leq 1 \qquad \textbf{(4.3)}$$

However, for a 3D geometry the solution is not as simple. For equally spaced x, y and z spatial steps of size Δx, it takes $3\Delta t$ time steps to communicate information across the diagonal of the cube. The distance between these points is $\sqrt{3}\Delta x$, as shown in Figure 4.2.

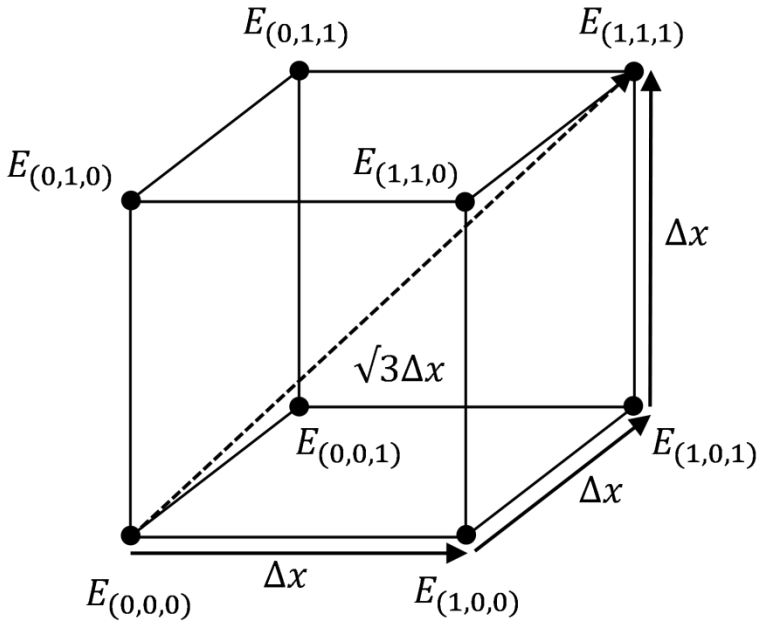

Figure 4.2: 3D FDTD domain and shortest distance across a cube.

Therefore equation (4.2) must now be updated to;

$$c3\Delta t \leq \sqrt{3}\Delta x \qquad \textbf{(4.4a)}$$

$$\sqrt{3}c\Delta t \leq \Delta x \qquad \textbf{(4.4b)}$$

Combining eq. 4.1 and 4.4 gives;

$$S_c = \frac{c\,\Delta t}{\Delta x} \leq \frac{1}{\sqrt{3}} \qquad \textbf{(4.5)}$$

Choosing a courant number as large as is possible, given the limits imposed by (4.5), minimises the time steps required to navigate across a 3D geometry. This both minimises the computing time while also reducing the number of numerical artefacts which are

introduced at each timestep. An FDTD simulation with a courant number equal to 1 is free from any frequency dependent free space dispersion. However, for courant numbers <1 a phase speed difference is introduced by the second order approximation. The ratio between the discretised phase speed and the continuous speed is governed by [92];

$$\frac{\tilde{c}_p}{c_p} = \frac{\pi\sqrt{\mu_r\epsilon_r}}{N_\lambda sin^{-1}\left[\frac{\sqrt{\mu_r\epsilon_r}}{S_c}\sin\left(\frac{\pi S_c}{N_\lambda}\right)\right]} \quad \textbf{(4.6)}$$

Where c_p and $\tilde{c}_p$ are the continuous and discrete phase velocity respectively, N_λ is the number of nodes per wavelength, and μ_r and ϵ_r are material parameters.

For free space ($\sqrt{\mu_r\epsilon_r}$ = 1), equation (4.6) becomes dependent upon S_c and N_λ. For a given set of simulation parameters, a fixed S_c and cell size, the error between the discretised and continuous phase speeds is frequency dependent. As S_c tends to 1 the ratio also tends to 1. In order to minimise the frequency dispersion we must maximise the courant number, S_c, and the number of nodes per wavelength, N_λ, by reducing the node spacing.

4.3 Electromagnetic Source

One of the main features of a FDTD simulation is the ability to model a broad range of frequencies in a single simulation. This requires a pulsed source, similar to that obtained by the THz-TDS system presented in chapter 2. A Ricker Wavelet is the second order derivative of a Gaussian pulse, containing a broad pulse of frequencies about a defined peak value, but unlike a Gaussian pulse, this wavelet has no net DC component. The time domain response of the Ricker Wavelet (Figure 4.4a) is a close approximation to that of the THz pulse produced by the THz-TDS system presented in chapter 2.1.

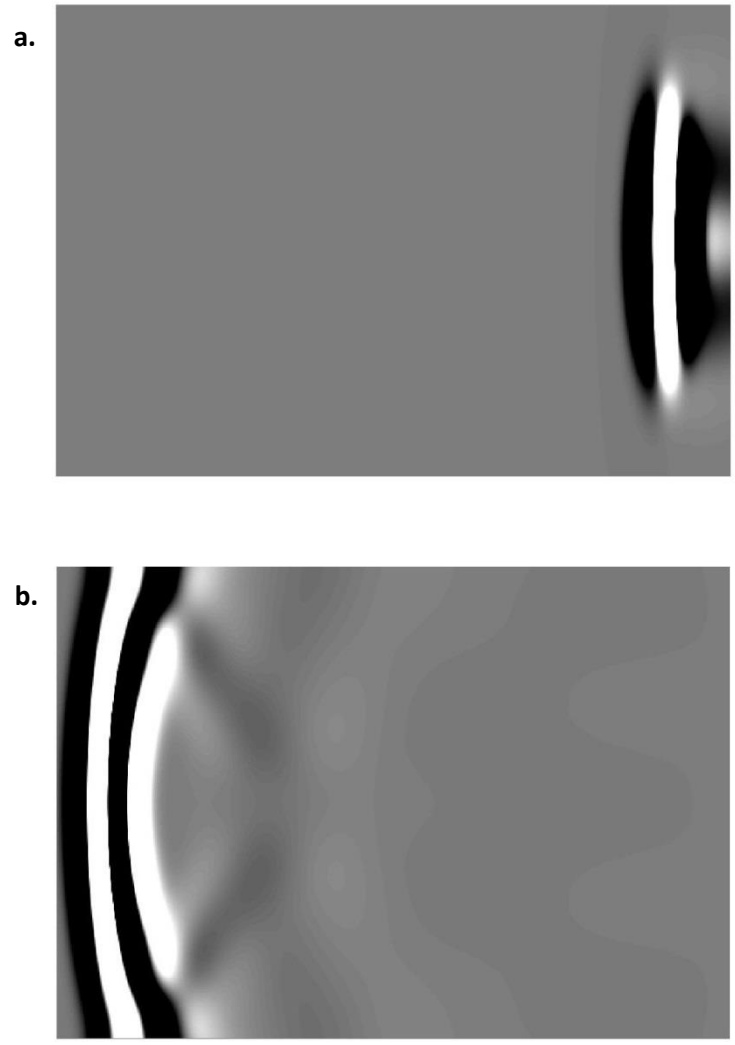

Figure 4.3: X-Z 2D cut plane image of electric field induced by a Ricker Wavelet in free-space at a. t ≈ 1 ps and b. t ≈ 5 ps.

The propagation of the Ricker Wavelet pulse in a free space 3D FDTD domain can be seen in Figure 4.3. The wavelet suffers a small amount of dispersion as it propagates due to a courant number <1, as discussed earlier in this chapter. The summation of the electric field in the z = 1 plane is shown Figure 4.4.a. along with its resultant FFT.

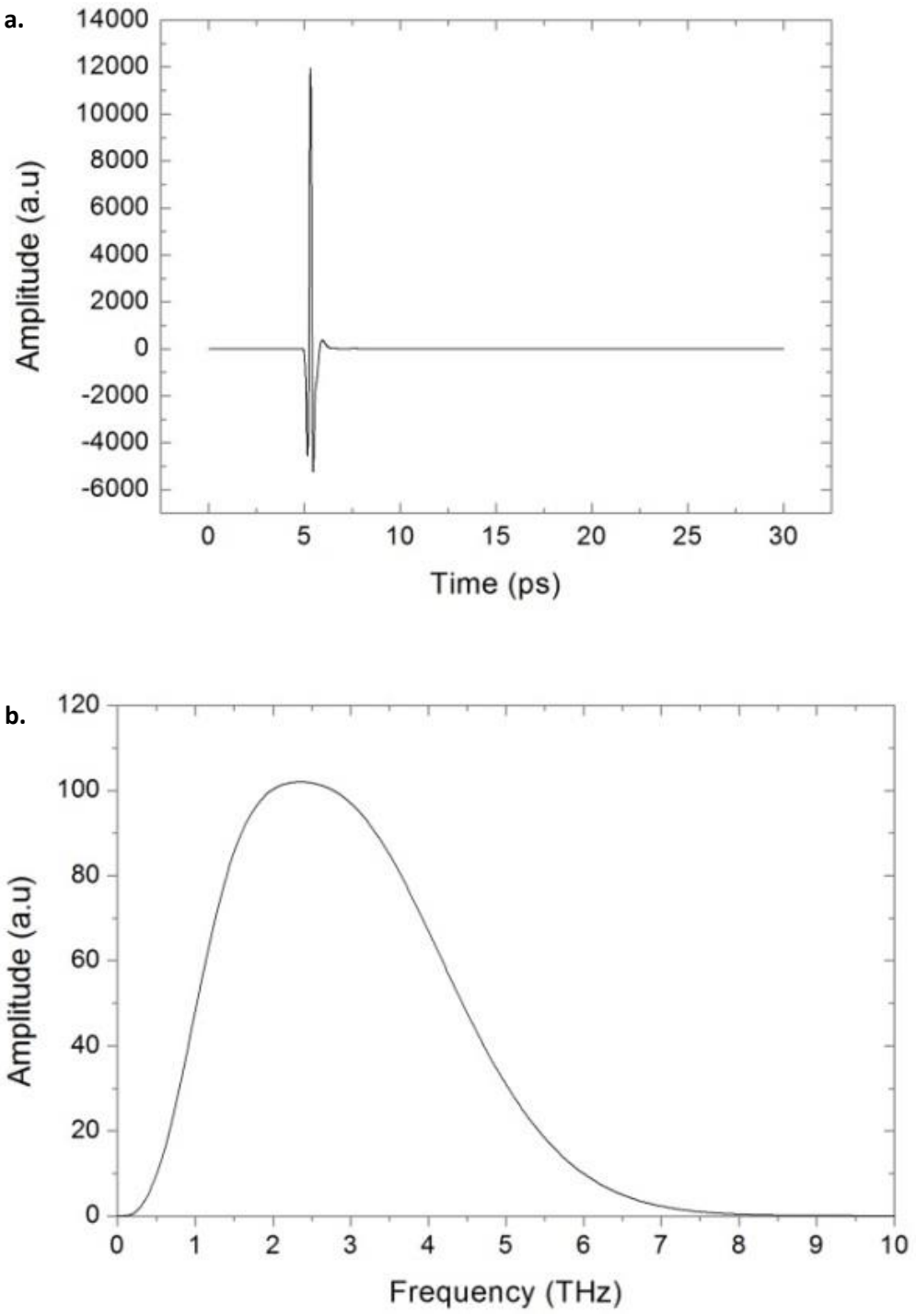

Figure 4.4: a. Lucifer simulation sum of electric field at monitored x-y plane and b. resultant FFT.

A broad frequency pulse has been achieved which propagates across the domain in ≈5 ps, experiencing only a small amount of dispersion. The observed electric field quickly decays to zero with no observable reflections within the 30 ps timescale.

4.4 Perfect Electrical Conductors

Perfect electric conductors (PECs) are ideal materials which possess an infinite conductivity. Such an approximation reduces the complexity of any problem over that of a real metal as an accurate determination of the metal's real and imaginary components over the frequency range is not required.

A PEC approximation has been demonstrated to be able to confine and propagate spoof SPPs under FDTD conditions [20] [59] [93] [94]. Experimentally valid for a range of real metals in the THz region due to their extremely small skin depth (40 nm [56]) at these frequencies, PECs prohibit the penetration of the electric field into the medium. As described in section 3.7 spoof SPPs are a function of subwavelength geometry, and no longer defined by the metal's plasma frequency.

4.5 Simulation Geometry

A standard FDTD approach to a periodic problem, as presented by an aperture array, is to utilise the symmetry to minimise the memory usage. Creating a domain containing a single periodic cell and applying periodic boundary conditions at four of the domain surfaces creates a close approximation to an infinite 2D array. Due to the array being significantly larger than the THz beam in the experimental conditions (chapter 2), this is a reasonable approximation. The single cell periodic approach minimises the computing time and memory requirements for any given problem to which it can be applied.

However, in order to accurately simulate the effect of changing the incident angle between the incoming electric field and the metal foil array, as will be discussed in Chapter 6, a number of constraints are put upon the simulation domain. To create an angle between the electric field propagation and the simulated array two options are available; tilt the array, or

rotate the source about the array (also requiring the rotation of the monitor plane). These two options are shown in 2D (for simplicity) in Figure 4.5.

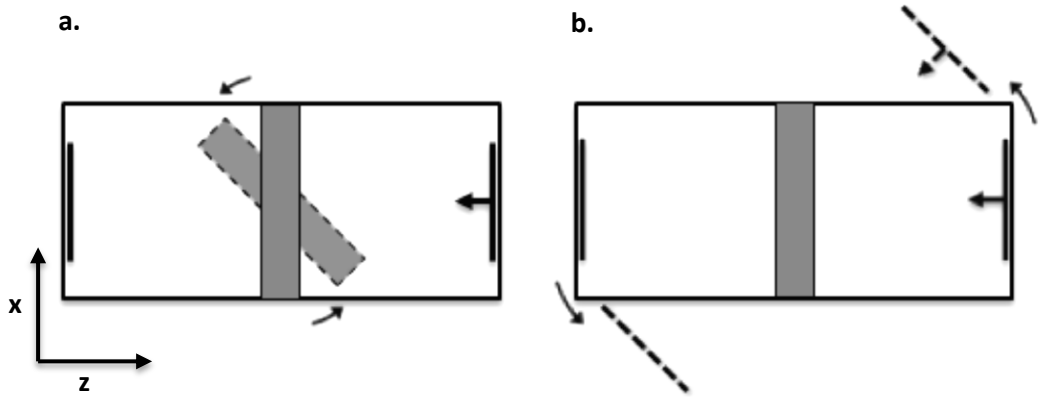

Figure 4.5: FDTD simulation domain for a. Tilted PEC array and b. Rotated montior and source.

It can be seen from Figure 4.5 that both of these solutions incur a problem. By tilting the array (Figure 4.5a), the full array is no longer continuous across the periodic boundary; each cell is separated from the next in the x-direction. Rotating the source and monitor plane about the array (Figure 4.5b) keeps the array continuity but the source and monitor no longer exist inside the simulation domain for the required incident angles at any reasonable far-field distance from the array. It is possible to apply a far to near-field conversion to the source and a reverse for the monitor. However, this adds unnecessary complexity.

If instead the simulation domain contained the entire array (>10^4 cells), then the array could be tilted as in Figure 4.5.a without causing any discontinuities. This approach would create an unfeasibly large simulation domain, requiring a huge increase in all 3 dimensions without allowing for any increased cell size. This approach can still be used, however, if the full aperture array can be reasonably approximated to a smaller size and still maintain its transmission properties without requiring periodic boundary conditions.

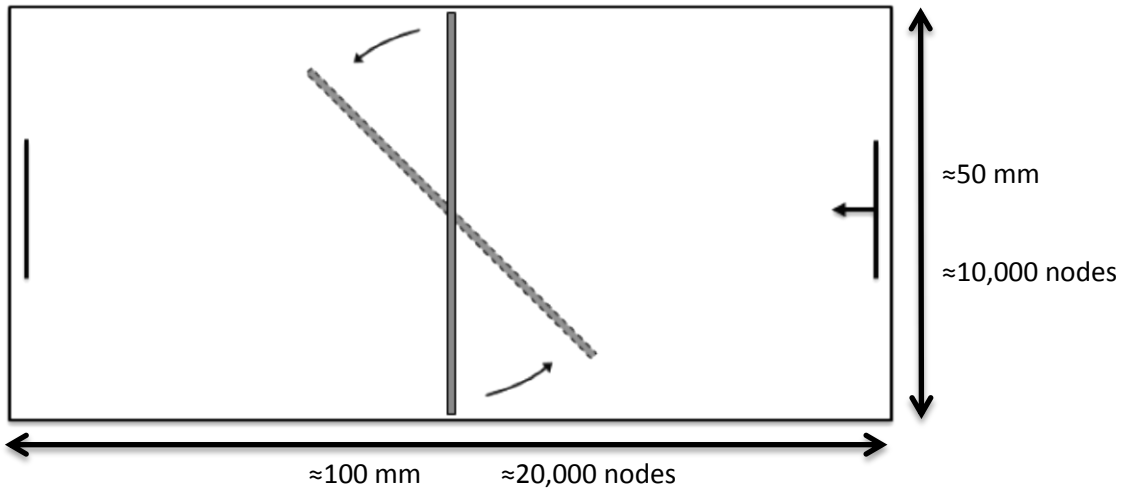

Figure 4.6: FDTD domain with non-periodic boundary conditions for full experimental measurement equivalency.

Figure 4.6 shows the equivalent FDTD domain to simulate the full experimental geometry of a 50 mm wafer placed in a 25 mm collimated beam. This requires approximately $10^4 \times 10^4 \times 10^4 = 10^{12}$ nodes for every timestep.

If the full array is to be approximated to a limited number of cells the largest possible physical size for a given number of simulation nodes is desirable, assuming this node spacing is sufficiently sub-wavelength that significant dispersion is not introduced by reducing N_λ, as described in (4.6). The highest common factor to all the array geometries is 5 µm. Applying this length as the 3D node spacing allows for the largest possible simulation domain for a given number of nodes while still accurately representing all array dimensions.

$$\Delta x = \Delta y = \Delta z = 5\ \mu m \qquad \textbf{(4.8)}$$

As discussed in section 4.2 the courant number is limited to $S_c \leq \frac{1}{\sqrt{3}}$ for a 3D domain, therefore $S_c = 0.5$ is a common number used for 3D FDTD, giving;

$$S_c = \frac{c\Delta t}{\Delta x} = 0.5 \qquad \textbf{(4.9a)}$$

$$\Delta x = 2\Delta t c \qquad \textbf{(4.9b)}$$

Equation (4.9b) shows that with a courant number of 0.5 the timestep, Δt, is set such that it takes two complete iterations for energy to travel a full spatial step.

The previously presented Figures 4.3 and 4.4 show that this N_λ and S_c combination does not introduce unreasonable dispersion during the full propagation of a THz Ricker Wavelet through a 410 x 410 x 600 node domain.

Approximating the full aperture array to a 7 x 7 hole region allows the creation of a 400 x 400 x 425 node domain; equivalent to a 2 x 2 x 2.125 mm region. A domain of this size is already computationally intensive for an FDTD approach; any smaller and the source and monitor could not be considered in the far-field, ≈ 2λ, and the apertures would not demonstrate an array-like response.

4.6 Simulation Screenshots

As previously discussed, due to the nature of numerical simulations, an FDTD can produce an incorrect numerical solution if numerical artefacts introduced at any given step become overwhelming. The stability of an FDTD simulation can be maximised by the correct selection of the courant number, S_c, and node spacing, Δx. However, it is always possible for some domain geometries to create instabilities.

4.6.1 Unstable Geometry

Visualisation of the simulation can help ensure that no instabilities are present and, if they do arise, what their origin is. With knowledge of the electric field at every node for every timestep of the simulation it is trivial to visualise the electric field in any 2D cut plane. Taking an x-z cut plane in the centre of the y-axis shows the propagation of the electric field through the domain as shown in Figure 4.7. The electric field at each node is grey scaled;

with white as +1, black as -1, and grey as 0. The absolute values of the electric field are arbitrary due to the arbitrary magnitude of the input Ricker wavelet and the consistent normalisation of time domain signals.

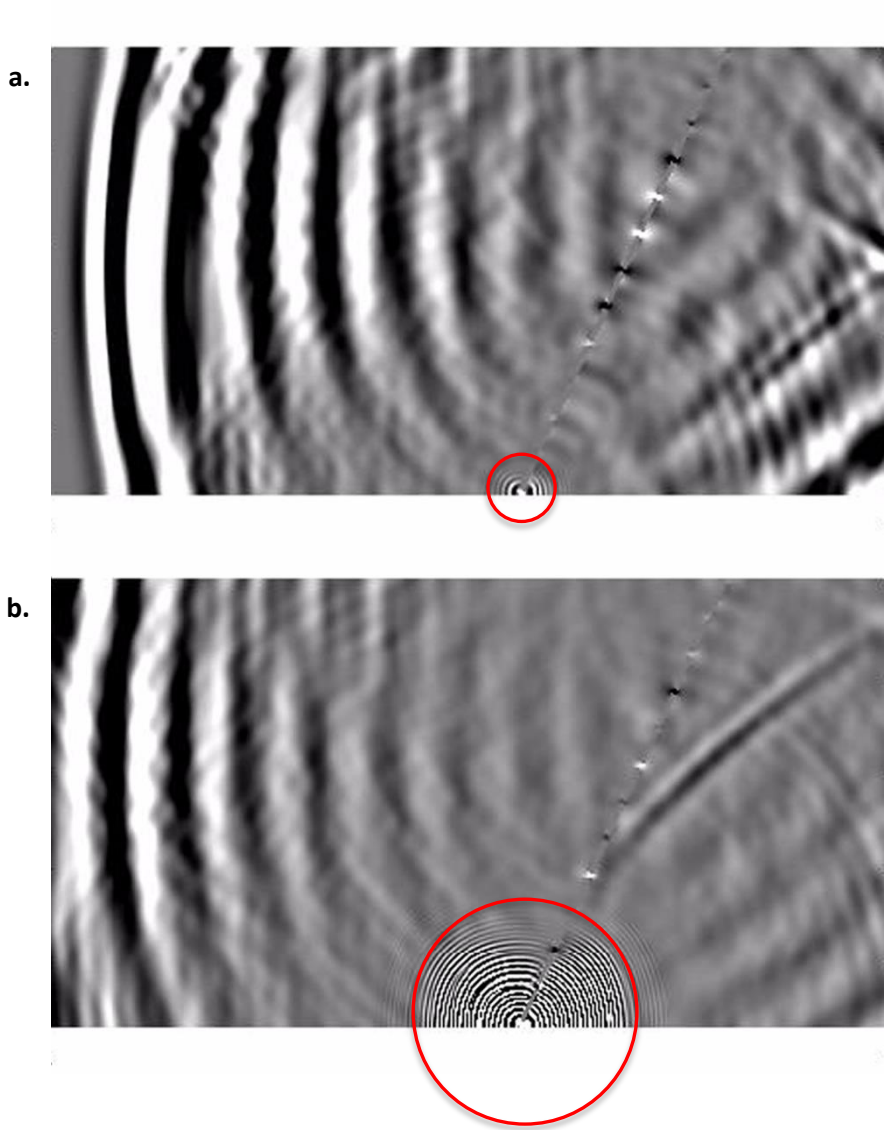

Figure 4.7: X-Z 2D cut plane of electric field for initial 25 degree incident angle FDTD simulation attempt at a. t ≈ 7 ps and b. t ≈ 8 ps.

The first attempts at implementing an incident angle by rotating the array inside the FDTD domain were dominated by instabilities. Figure 4.7 shows that the origin of these instabilities lies where the PEC array meets the boundary as highlighted in red. As the angle between the boundary and the PEC moves further from normal, this instability has been

found to appear at earlier timesteps. The cause is the propagation of a high electric field into a small number of cells bounded on 2 sides by a PEC and upon the third by the absorbing boundary condition. Unable to effectively dissipate the electric field at all frequencies, a high frequency instability begins to resonate and grow until it dominates the simulation.

4.6.2 Normal Incidence

To remove the instability, a space is introduced between the PEC array and the boundary of the simulation domain. In order to not introduce a wavelength scale feature between the metal array and the boundary, this gap must be sufficiently large such that it does not act as a resonant feature itself. The propagation of the electric field through a 7 by 7 PEC aperture array at normal incidence is shown in Figures 4.8-4.11.

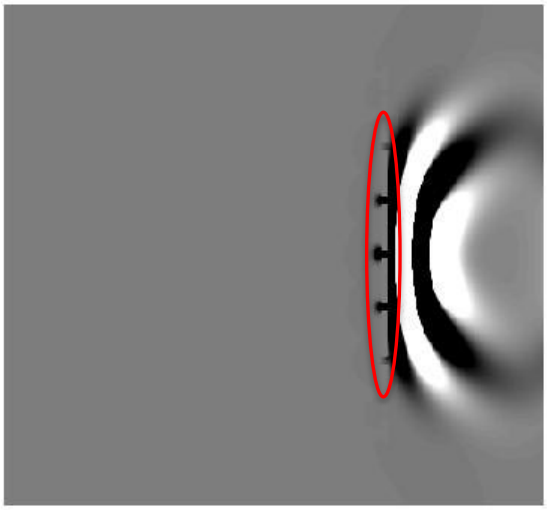

Figure 4.8: X-Z 2D cut plane of electric field for normal incident angle FDTD simulation at t ≈ 1.5 ps.

Figure 4.8 displays the 2D electric field after ≈ 1.5 ps when the Ricker Wavelet source reaches the PEC aperture array. The frequencies resonant to the slot apertures are accepted into the free space between the PEC regions. The PEC retains zero electric field, as shown by

the grey colour, despite the large electric field in the apertures; which can be clearly seen in the highlighted red area.

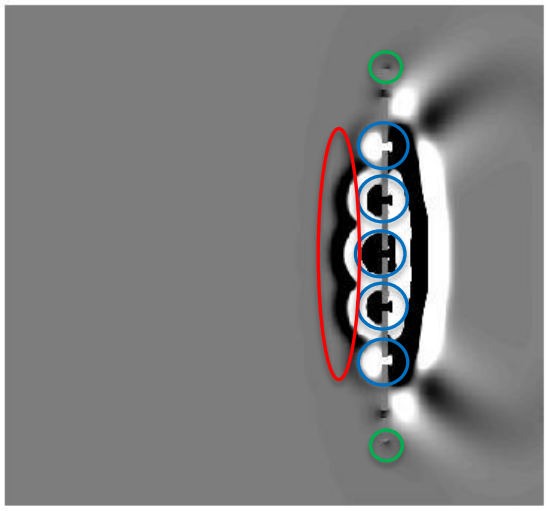

Figure 4.9: X-Z 2D cut plane of electric field for normal incident angle FDTD simulation at t ≈ 2 ps.

Figure 4.9 displays the 2D electric field after ≈ 2 ps when the apertures begin to oscillate at their resonant frequency producing a transmitted wave. Each aperture acts a point source, emitting an electric field in all directions as it decays, seen in blue highlighted areas in Figure 4.9. The point sources combine to reproduce a transmitted wave as seen in the red highlighted area. The edges of the PEC array can be observed in the green highlighted areas, as a small electric field propagates around these points.

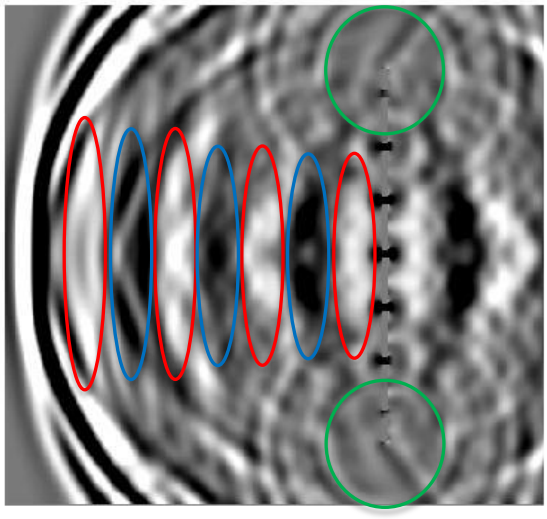

Figure 4.10: X-Z 2D cut plane of electric field for normal incident angle FDTD simulation at t ≈ 5 ps.

Figure 4.10 displays the 2D electric field strength after ≈ 5 ps. At this time, the initial array transmission reaches the monitor plane. The red and blue highlighted areas show successive positive and negative envelopes forming in the far field. These envelopes sum to produce the characteristic oscillations of aperture array transmission. The green highlighted area shows the array edges acting as a diffraction edge and a weak electric field can be observed oscillating from these points. These oscillations contain all frequencies of the initial Ricker Wavelet and have no observable effect upon the monitored pulse.

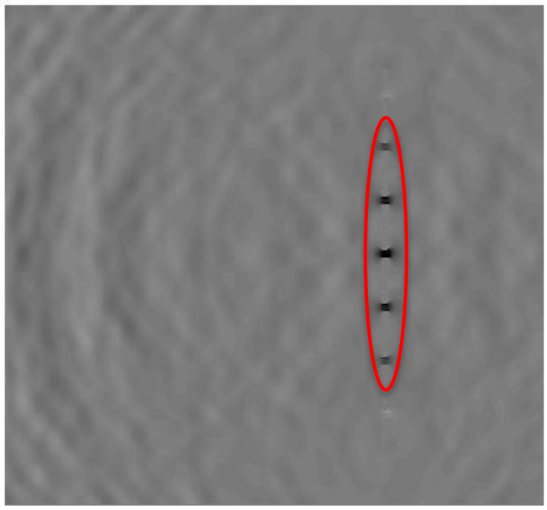

Figure 4.11: X-Z 2D cut plane of electric field for normal incident angle FDTD simulation at t ≈ 9 ps.

Figure 4.11 shows the electric field after the aperture array emission has decayed to the point at which the pulse train is barely observable. The red highlighted region shows that the apertures still retain a relatively high electric field confined to the free space holes; however the emission is such that the transmission is no longer significant.

4.6.3 Angular Incidence

Using an identical geometry and domain structure to that shown in 4.5.2, except for a rotation in the aperture array about its centre point in the y-axis, produces an incident angle between the electric field and the PEC array. The changes to the electric field propagation by comparison to a normal incidence array will be shown and discussed in Figures 4.12-4.15.

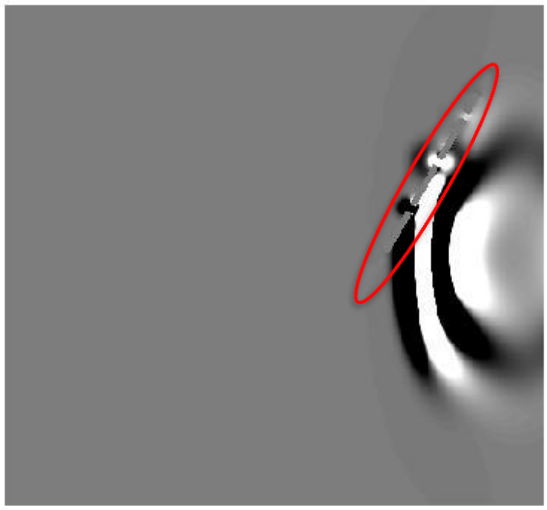

Figure 4.12: X-Z 2D cut plane of electric field for 30 degree incident angle FDTD simulation at t ≈ 1.5 ps.

Figure 4.12 shows how the Ricker Wavelet arrives at the apertures at different timesteps due to their varied special positioning in the z domain. The free space aperture holes in the PEC array accept the resonant frequencies defined by their geometry; however, due to the temporal variance in the arrival of the wavelet, they begin to oscillate out of phase, as shown in the highlighted red area.

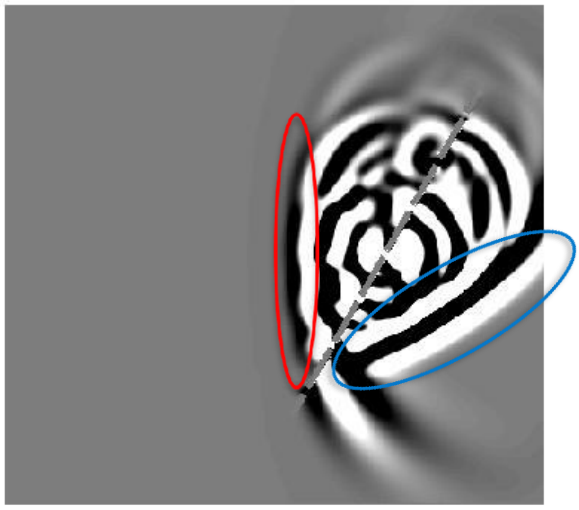

Figure 4.13: X-Z 2D cut plane of electric field for 30 degree incident angle FDTD simulation at t ≈ 2 ps.

Figure 4.13 shows how those frequencies, which are not accepted by the apertures, are reflected from the surface at 60° degree for a 30 ° degree incidence between the array and incoming wavelet, as shown in the blue highlight area. The transmitted wave however retains its pre-array directionality; recombining the emission from each aperture, each acting as a point source this time with a varied spatial position matched by a varied temporal phase.

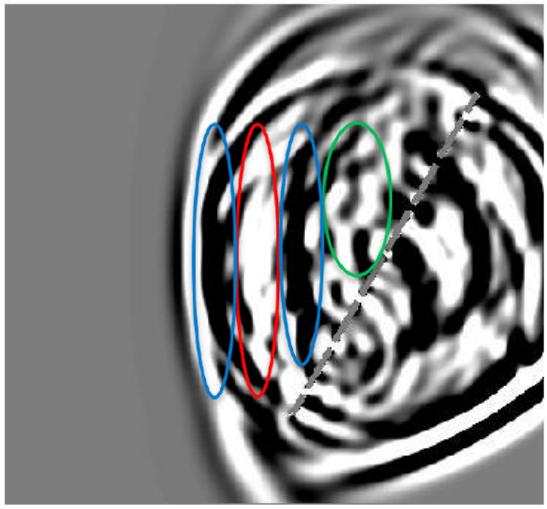

Figure 4.14: X-Z 2D cut plane of electric field for 30 degree incident angle FDTD simulation at t ≈ 3 ps.

Figure 4.14 shows as the emission moves into the far field the successive positive and negative envelopes form, as seen in red and blue highlighted areas. The resultant transmitted wave is very similar to that observed in Figure 4.10 for a normal incidence PEC aperture array. The green highlighted region shows how in the near-field, before the different aperture emissions have propagated far enough, the envelopes are not yet recognisable.

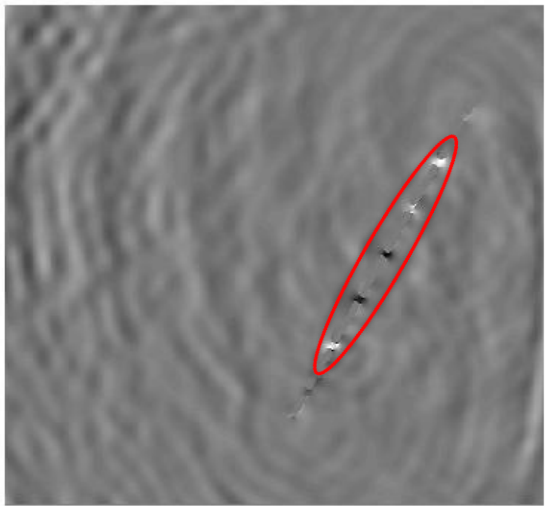

Figure 4.15: X-Z 2D cut plane of electric field for 30 degree incident angle FDTD simulation at t ≈ 9 ps.

As previously shown in Figure 4.11, Figure 4.15 shows the electric field is still relatively well confined inside the apertures, after the emission has long decayed below an observable level. In this case, the apertures still remain out of phase, however, as shown in the red highlighted area.

4.7 Commercial Simulation Comparisons

Two commercial simulation packages have been used as comparisons to Lucifer. Comparing the data produced by Lucifer to data obtained by measurement and other simulation packages helps to assess the strengths and limitations of the solution.

In chapter 5 data produced by a commercial FDTD simulation package named Lumerical is compared to that of Lucifer. Lumerical provides an easy to use interface for creating geometries, adding source and monitors, controlling cell size. Optimisation of the solver process reduces the computational intensity of the simulation, providing a solution in approximately a quarter of the time taken by Lucifer. Graphical tools provided by Lumerical

provide visualisation of the solution. However, extraction of the raw data for analysis proves to be laborious.

In chapter 6 when data provided by both Lucifer and Lumerical were found to not accurately represent the measured data, a third simulation package, Computer Simulation Technology (CST), was provided by Imperial College London. The CST solution applies a frequency domain solver providing significantly different results.

Further analysis of the simulation data produced by the three programs is provided as the results are presented in chapters 5 and 6.

4.8 Conclusions

An FDTD geometry has been developed and used to simulate the effects of geometrical changes to the transmission properties of an aperture array in the THz region. The propagation of a broadband Ricker Wavelet has been observed. The electric field for a 2D x-z cut plane for every timestep of the simulation are recorded as well as that reaching the x-y plane monitor. This electric field can be turned into images, of which a selection have been shown in this chapter, and collated into a video allowing for a visual check of the simulation for instabilities and errors.

Applying a PEC approximation for the metallic structure in the THz region has been determined as a reasonable approach to reduce the complexity of the solution. Limited by computing resources available, a 7 x 7 array of apertures has been chosen as a reasonable approximation of a full array in the absence of a suitable periodic boundary solution. Geometrical instabilities, caused by the tilting of the PEC array, have been overcome producing a powerful tool to interrogate the source of various resonant features in sub-wavelength aperture arrays.

The simulation results have been extensively compared to measured THz-TDS and VNA data, as well as Lumerical and CST commercial solutions, and will be presented in chapters 5 and 6 along with experimental measurements.

Chapter 5

Transmission Mechanisms

Since the first observation of EOT by Ebbesen [14], the optimisation and control of the transmission spectra of two dimensional aperture arrays has been under investigation. This chapter will present the experimental results obtained using the Terahertz Time-Domain Spectroscopy (THz-TDS) system outlined in chapter 2 for a free standing metal foil array perforated with sub-wavelength apertures. A systematic approach has been undertaken to vary individual design parameters in an attempt to control the shape and position of the resonant peak produced. To obtain as 'clean' an experiment as possible, it is beneficial to create a free standing metallic foil array, with no change in dielectric material in the THz beam path the possible sources of resonant features and reflections are reduced. A free standing array within a single dielectric material, usually air, removes reflections at dielectric/dielectric interfaces and creates identical resonant conditions at both the front

and back interface. This largely reduces the complexity of the problem, the source of resonances can be more readily identified and the transmission is increased.

5.1 Fabrication

Aperture arrays, composed of rectangular holes in a copper foil, were fabricated by electro-deposition. Aperture dimensions were controlled by standard lithographic techniques and used to create pillars of photoresist of the order of tens of μm. From a fabrication perspective, THz is an ideal region of the spectrum in which to work. This is mostly due to the ease at which modern lithography can pattern objects at a similar scale to the wavelength of THz waves (1 THz ≈ 300 μm).

5.1.1 Lithography

AZ9260, a positive 'thick' photoresist, was used in a three layer deposition process followed by a hardbake to create a layer in the region of 40 μm thick. The spin-bake process is as follows;

1. AZ9260 deposition
2. Spin at 500 rpm for 10 sec increasing to 1500 rpm for 50 sec
3. Wait for 1 minute
4. Softbake for 7 minutes at 95 ^{o}C
5. Wait 2 minutes
6. Repeat steps 1-5 twice more
7. Edge-bead removal
8. Hardbake for 1 hour at 95 ^{o}C

Once the deposition is completed, the resist has become dehydrated due to the hardbake process step. In diazonaphthoquinone (DNQ) resists, such as AZ9260, water is required during exposure to transform the ketene photoproduct into indene-3-carboxylic acid [95]. Ketene also reacts with Novolak polymers present in the resist to form a Novolak matrix. In

the presence of water the slow Novolak reaction can be discounted. However, in a water deficient resist, it becomes dominant, and a cross-linked Novolak matrix is formed. For near vertical side wall profiles and high levels of aperture shape control, any cross-linking must be minimised. Therefore, a rehydration step is the key to maintaining a high level of precision over the fabrication.

In thin films of resist, rehydration via diffusion occurs very quickly. Therefore, water deficiency is not an issue. In thick films, however, diffusion from the resist/air interface means that this process can take several thousand times longer. Simulations have shown that, for a 40 µm thick AZ9260 resist, a hydration time in the region of 18 hours is required, dependent upon relative humidity level [96]. For this reason, a wait period of 18-24 hours is given between hardbake and exposure. Once this rehydration period has passed, the resist can be developed in a solution of deionised water:AZ400K at a 3:1 ratio for 10-12 minutes.

Once the AZ9260 thick resist has been deposited, exposed and developed, an array of resist structures, 40 µm high with varied dimensions and spacing, upon a Ti/Au seed layer is left. Figure 5.1 shows SEM images of such resist patterns.

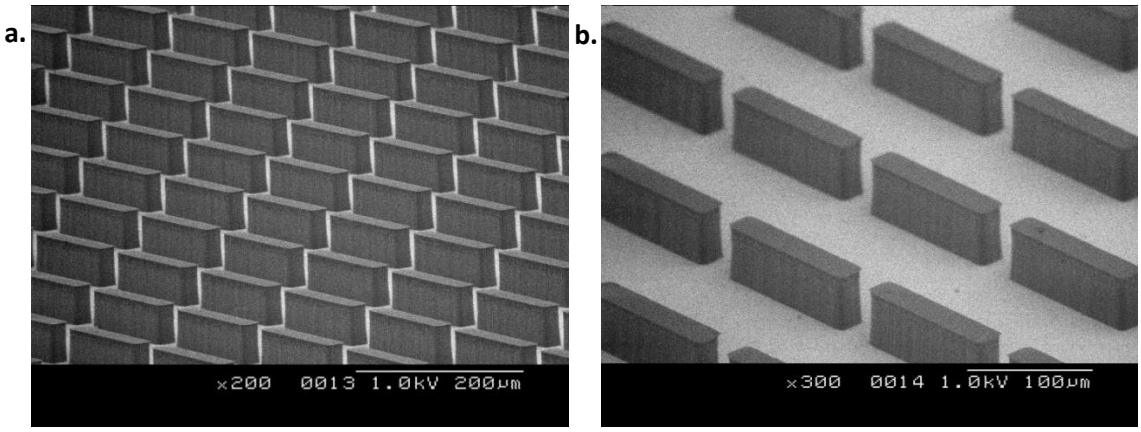

Figure 5.1: SEM image of lithographically patterned AZ9260 at; a. 200 and b. 300 times magnification.

5.1.2 Copper Electroplating

A commercial electroplating solution, InterVia Cu 8540, was used in conjunction with a sacrificial Cu anode to deposit a thin copper layer. 15 mA/cm^2 constant current was applied across the sample cathode and sacrificial copper anode, which were suspended 3 cm apart in the plating solution, achieving a deposition rate of approximately 0.5 µm/min. Electroplating for a one hour period produced a copper foil of 25-30 µm thickness, thick enough to achieve the strength and stiffness required to be free-standing.

Maintaining a high quality electroplating surface finish requires careful maintenance of the electroplating solution and equipment. Continuous filtration of the solution is performed during the plating process, by an automated pumped system, to remove any debris. After fabrication of each sample the InterVia Cu 8540 solution is replenished with 10 ml/L of Intervia 8540 Additive, a brightening agent commercially available with Intervia Cu 8540.

Manual removal of Cu build-up on the electroplating contacts is necessary to minimise debris which can lead to defects in the surface finish. Deviation from this strict routine results in steadily declining fabrication quality and rising defect levels.

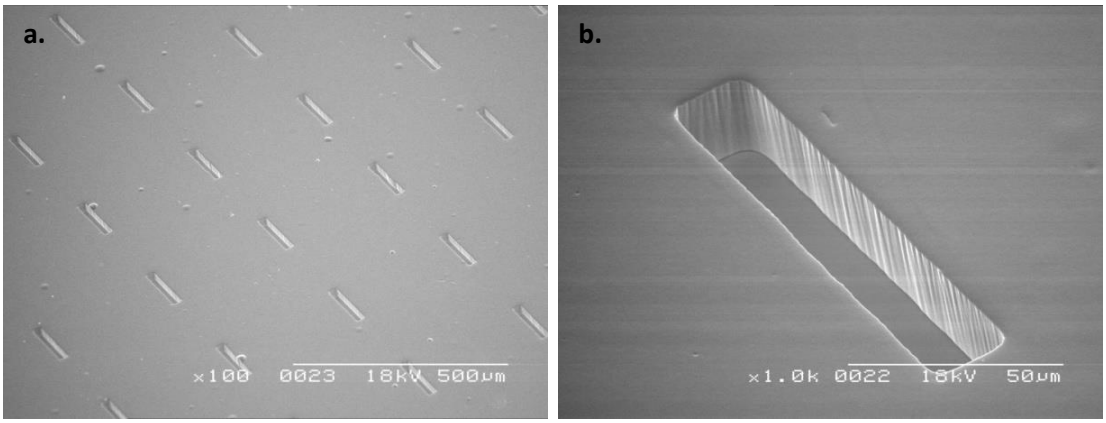

Figure 5.2: SEM image of Cu thin film aperture array fabricated via electroplating at; a. 100 and b.1000 times magnification.

Once the electroplating was completed, the photoresist pillars were removed by acetone producing the metal foil shown in Figure 5.2. Cu and Au have a low level of adhesion, allowing the Cu layer to be separated from the Au layer by simply peeling the thin Cu foil to leave a free standing Cu aperture array.

5.2 Fixed Ratio Arrays

By fixing the ratios between all aperture array dimensions; aperture width and length, periodic spacing x and y, it should be possible to create arrays with similar resonant features over a range of frequencies. A range of aperture sizes with a fixed 5:1 aspect ratio in a square lattice with a periodicity of 7 times aperture width, from now on described as 5:1:7 aperture arrays, have been designed to display slot antenna resonances between 1.0 and 1.5 THz.

Using the THz-TDS techniques presented in section 2.1, the frequency domain response of the apertures can be obtained by FFT of the time-domain response to a broadband THz pulse. The frequency response of a range of 5:1:7 ratio arrays at multiples of 20.0, 22.5, 25.0, 27.5 and 30 µm is shown in Figure 5.3, each spectra showing the normalised transmission strength obtained as discussed in section 2.1.4.

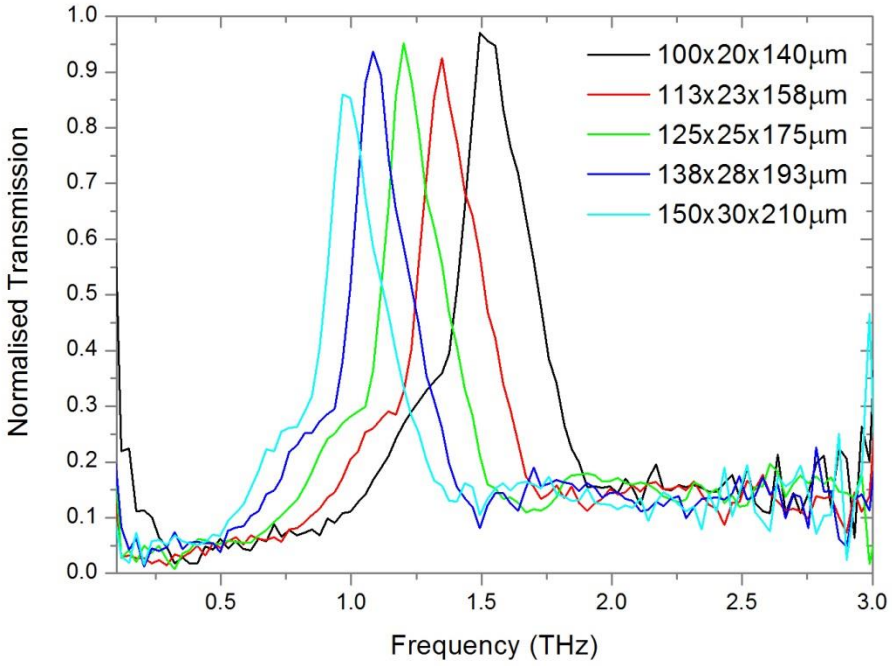

Figure 5.3: Normalised THz-TDS transmission of 5:1:7 ratio aperture arrays.

Figure 5.3 shows that the arrays at a fixed 5:1:7 ratio display the same spectral features, each with a resonant peak transmission related to half the free space wavelength of the slot antenna as discussed in section 3.8. No resonant transmission is observed. However, at the lattice constant (relating to ≈ 2.14, 1.90, 1.71, 1.55 and 1.43 THz for 140, 158, 175, 193 and 210 μm respectively), as would be predicted for a THz SPP defined transmission phenomena.

The aperture array free space density for these arrays is ≈10%, yet the transmission achievable is >95% at resonance. If the transmission is normalised to free space density, then the transmission strength approaches 10 times that incident upon free space apertures, as shown in Figure 5.4. This transmission is significantly above the initial case for EOT [14], which reported; 'more surprising is that the absolute transmission efficiency, calculated by dividing the fraction of light transmitted by the fraction of surface area occupied by the holes, is >2 at the maxima'. Possibly more significant is that this

transmission exceeds the transmission predicted for a single 5:1 aspect ratio aperture (≈ 6) by Garcia-Vidal [79].

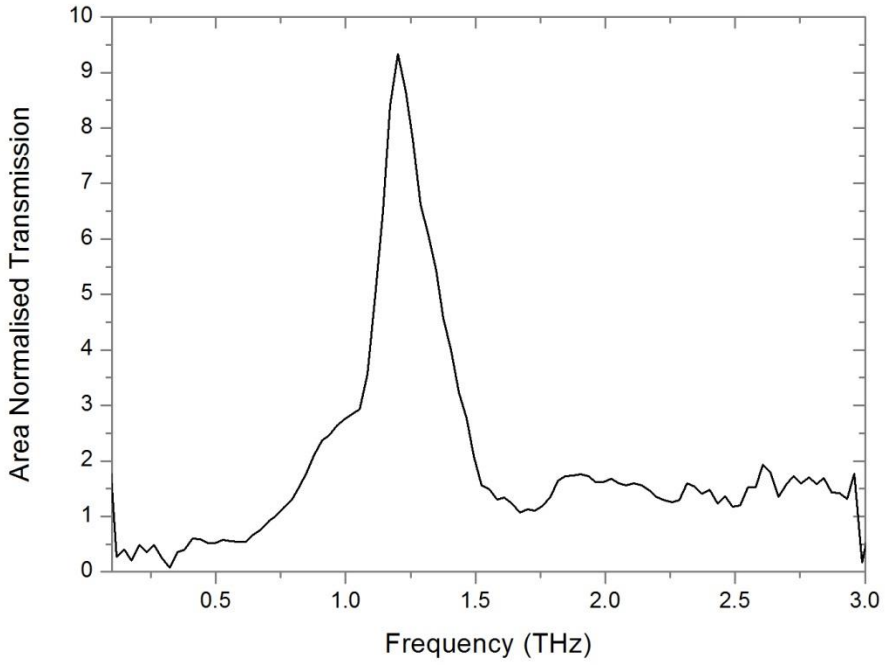

Figure 5.4: Free space aperture area normalised THz-TDS transmission of 125x25x175 µm aperture arrays.

The time domain response of the aperture arrays to a THz reference pulse show a long decay in transmission over ≈ 10 ps, Figure 5.5. Comparing the time domain response of the 20 and 30 µm ratio arrays we observe that the response of both arrays decay over a similar time period. Between 20 ps and 27 ps we observe 12 oscillations for the higher frequency 20 µm array, but only 8 for the 30 µm array.

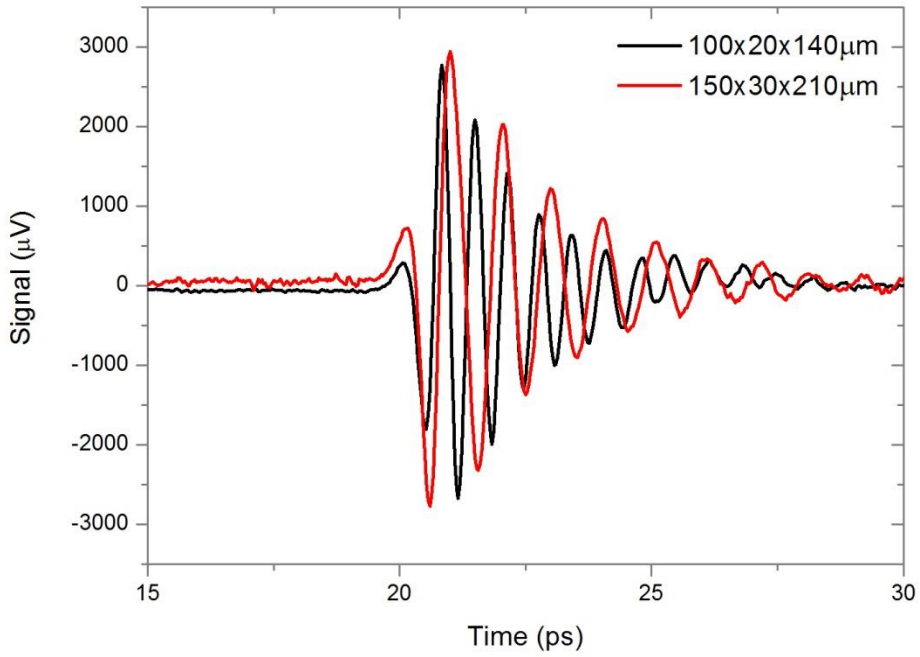

Figure 5.5: Time-domain response to a broadband THz-TDS pulse.

The repeatability of this measurement, especially across different physical samples, is of importance. Figure 5.6 shows the transmission spectra of two different 125x25x175 µm arrays, each individually fabricated, aligned in the system and measured. We observe near identical transmission peak strength, position and shape for the two separately fabricated aperture arrays. However, a difference in the spectra can be observed at ≈ 1.7 THz. This dip in the transmission spectra is closely related to the periodic spacing (1.7 THz ≈ 175 µm) as would be expected for a THz SPP. The origin of this feature, and its impact upon the EOT of rectangular aperture arrays in the THz region, will form much of the discussion in this chapter. A possible cause for the difference between the two observed spectra will be discussed in section 6.2.

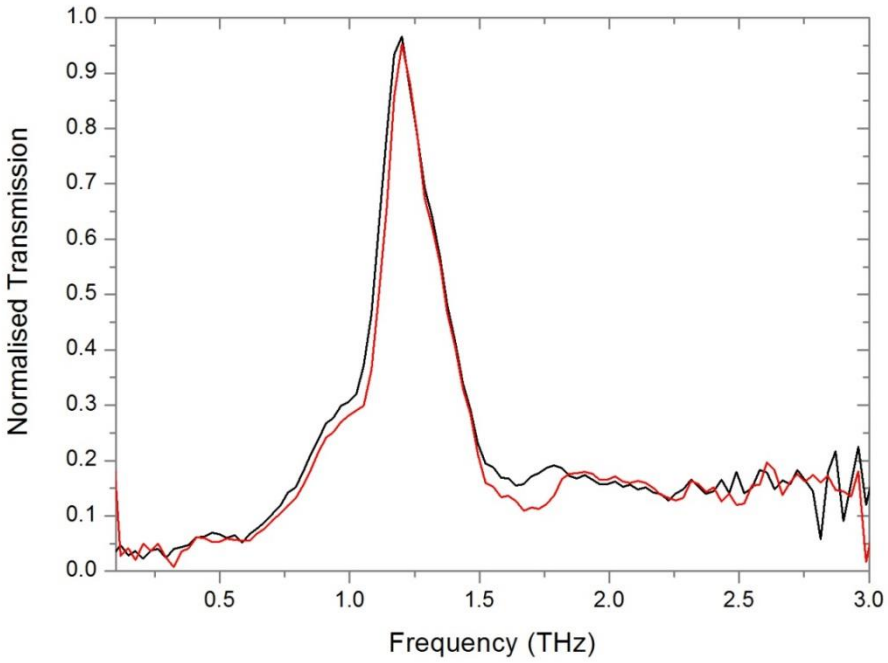

Figure 5.6: Normalised THz-TDS transmission of separately fabricated and tested 125 x 25 x 175 µm arrays.

5.3 Fixed Apertures Varied Square Lattice

Rectangular apertures with a 5:1 aspect ratio; width 25 µm, length 125 µm, have been fabricated with various periodic spacing in a square lattice. Keeping the aperture dimensions constant, the periodic spacing of the square lattice is varied from 300 µm to 150 µm, a 4 fold increase in aperture density. Figure 5.7 shows the normalised FFT transmission spectra for these arrays.

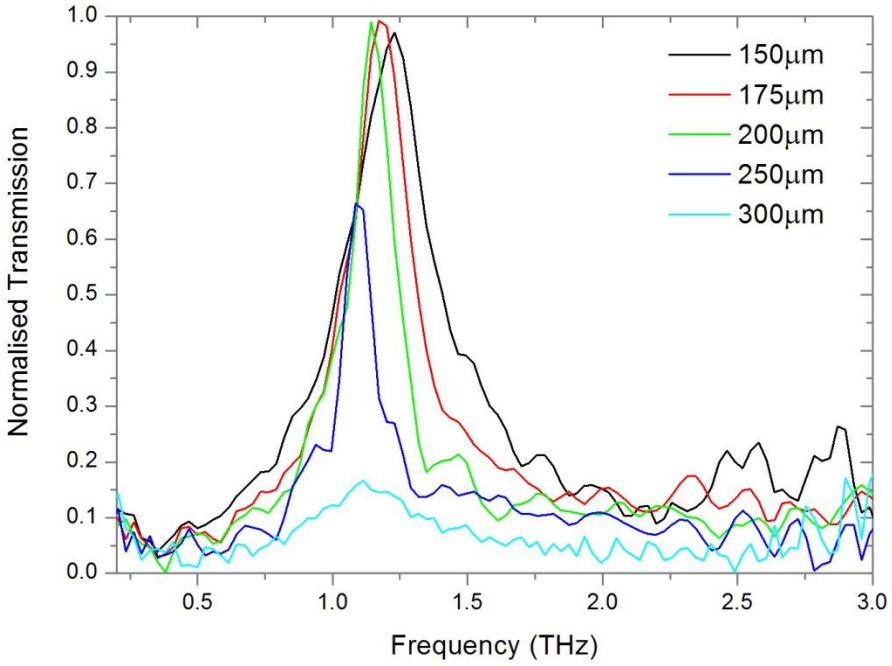

Figure 5.7: Normalised THz-TDS transmission of 125 x 25 µm aperture arrays with varied periodic square lattice spacing.

It can be seen from Figure 5.7 that for a periodic spacing ≤ 200 µm rectangular apertures of 125 µm by 25 µm display peak transmission >95%, despite free space area as low as 8%. As the periodic spacing increases beyond 200 µm, the transmission peak strength reduces. Peak transmission frequency can also be seen to vary as the periodic spacing changes. This transmission can again be applied to the definition of EOT by normalising to the free-space aperture area as in Figure 5.8.

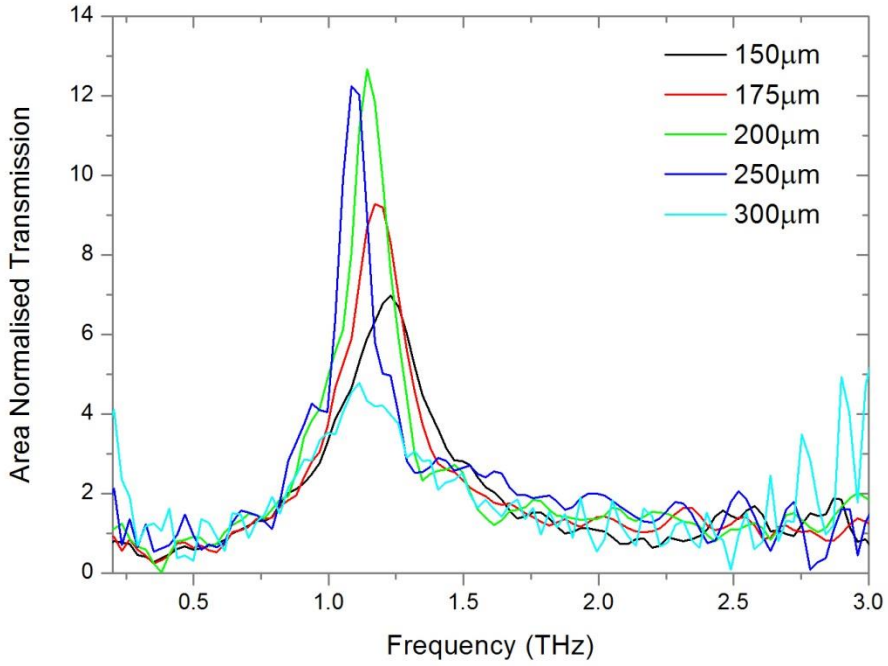

Figure 5.8: Free-space aperture area normalised THz-TDS transmission of 125 x 25 µm aperture arrays with varied periodic square lattice spacing.

In Figure 5.8 transmission is observed at > 12 for the normalised free space aperture area when in a 200 µm square lattice. The area normalised transmission achieved by that 150 µm periodic lattice is similar to that predicted by Ruan [80] for a 4.5:1 ratio rectangular aperture in a square lattice, 1.2 times the long aperture edge. The trend observed by Ruan (increasing area normalised transmission for increased periodic spacing) holds until a square lattice ≈ 200 µm (1.6a as defined by Ruan).

From Figure 5.9, we can see that the lower aperture density of the 200 µm periodicity array leads to a lower magnitude first oscillation than that of a 150 µm periodicity array. A longer resonance, produced by a slower decay in each subsequent oscillation, allows for similar (near unity) peak transmission strength for the 200 µm periodicity array despite the lower strength first oscillation. We observe a full 11 oscillations over a period of 10 ps after the initial pulse for the 200 µm periodicity array. However, the 150 µm array has decayed to

within the noise level in 7 oscillations and <6 ps. Greater initial transmission is provided by the higher density of apertures. However, as a linear system, the decay of these apertures is limited by the input power at that frequency. Large initial transmission is followed by fast decay, limited to ≤ 100% of the power at that frequency incident upon the array. Lower density arrays compensate for lower initial transmission, with longer decay times provided by greater localisation of the electric field in the aperture [79].

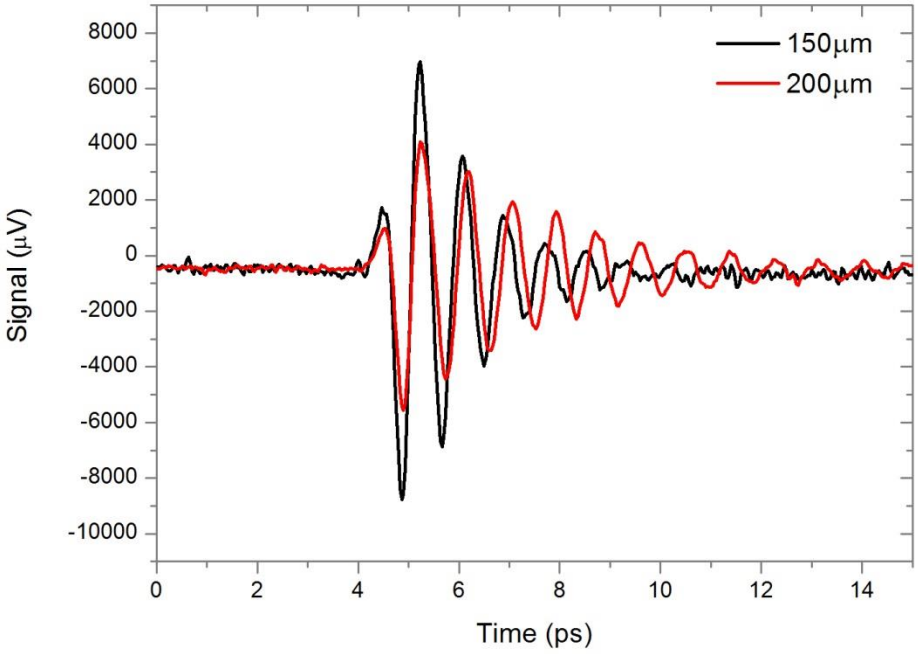

Figure 5.9: THz-TDS timescan for 125 x 25 μm aperture array with varied periodic spacing.

Figure 5.10 compares the transmission spectra obtained by THz-TDS measurement to that obtained by FDTD simulation as discussed in chapter 4 (Lucifer), as well as that obtained by Lumerical as outlined in section 4.6.

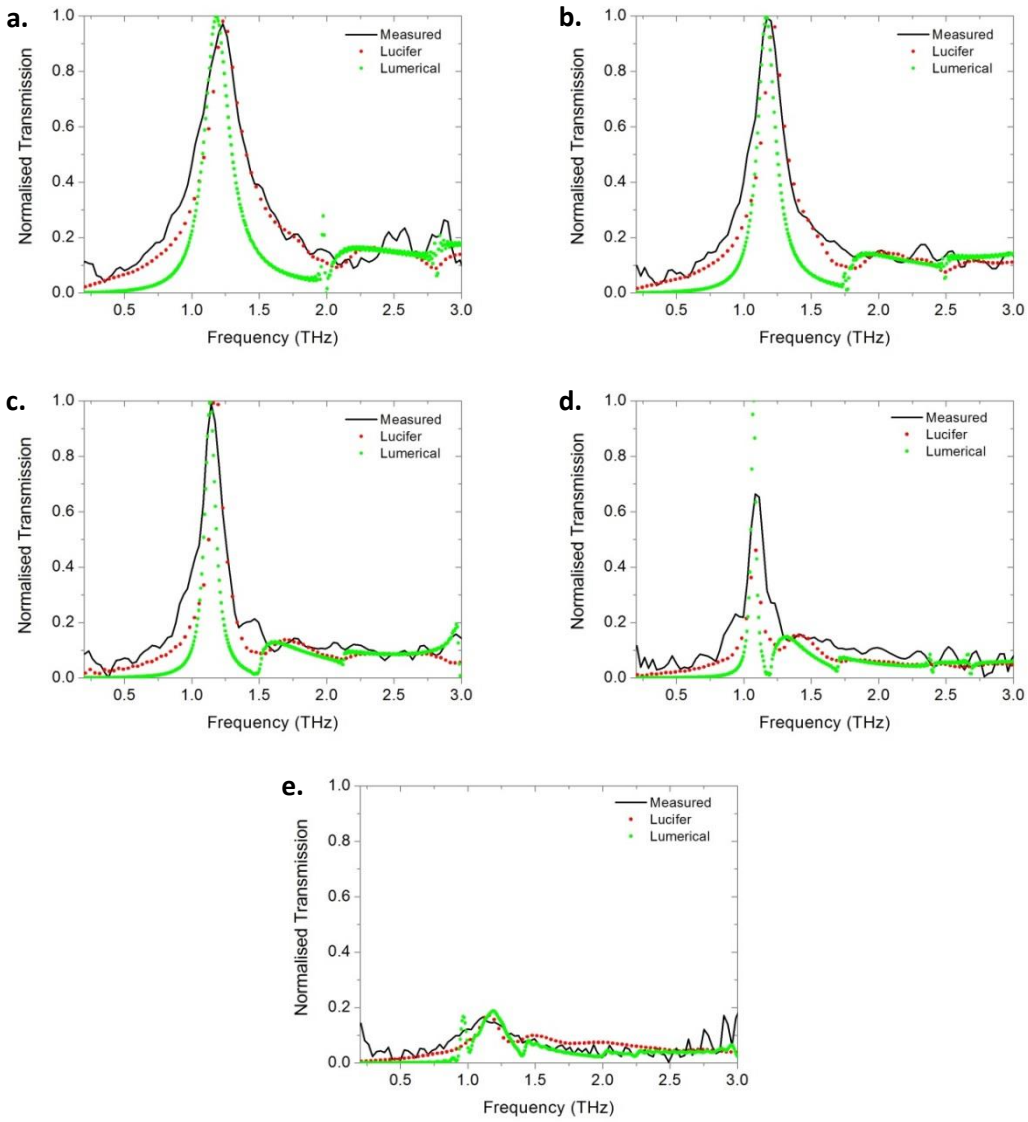

Figure 5.10: Normalised THz-TDS transmission of 125 x 25 µm aperture arrays with varied periodic square lattice spacing compared to two FDTD simulation methods. Periodic spacing; a. 150 µm, b. 175 µm, c. 200 µm, d. 250 µm, e. 300 µm.

Figure 5.10 shows that Lucifer accurately predicts the spectral shape and transmission strength of the free standing copper foil arrays. Lucifer more closely describes the measured THz-TDS spectra than Lumerical in terms of peak width and fall in transmission strength above 200 µm periodicity. Both simulation packages introduce a spectral feature at a frequency relating to the periodic spacing; in the case of Lucifer, this feature is a dip in

transmission strength, and for Lumerical this is a very sharp peak followed by a minimum and then a small rise in transmission.

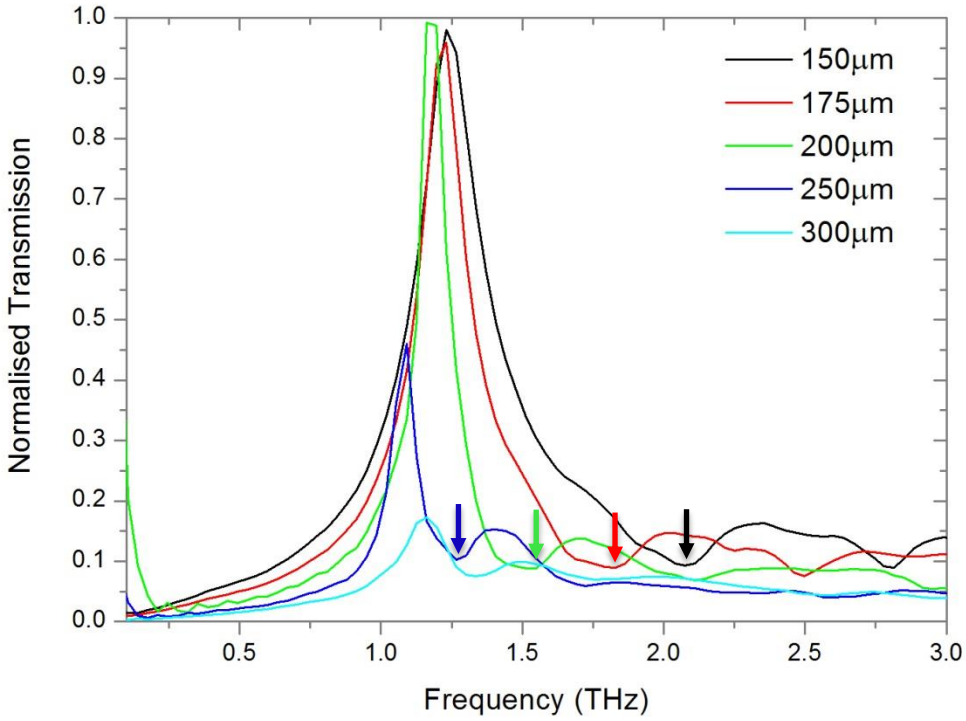

Figure 5.11: Normalised FDTD transmission of 125 x 25 µm aperture arrays with varied periodic square lattice spacing obtained by Lucifer. Coloured arrows indicate minima.

Figure 5.11 compares the normalised transmission obtained for each periodic square lattice spacing (Lucifer FDTD simulation). The arrows point to the frequency location of dips in transmission strength, each closely related to the periodic spacing of the array square lattice by free space wavelength. Beginning at 150 µm, the minimum (≈ 2 THz) is far enough away from the resonant transmission peak created by 125 µm slot antennas (≈ 1.2 THz) to not affect the transmission peak. As the periodic spacing increases, the frequency of the minimum is reduced. As the minimum first approaches the resonant peak, we observe a narrowing of the transmission peak along with a small shift in peak frequency, 175 and 200 µm. As the periodic spacing reaches double the slot antenna length, the minimum and

transmission peak are very closely spaced. At this point, the transmission peak is largely suppressed in strength by the minimum. As the periodicity continues to increase we no longer observe a clear transmission peak with maximum transmission < 20%.

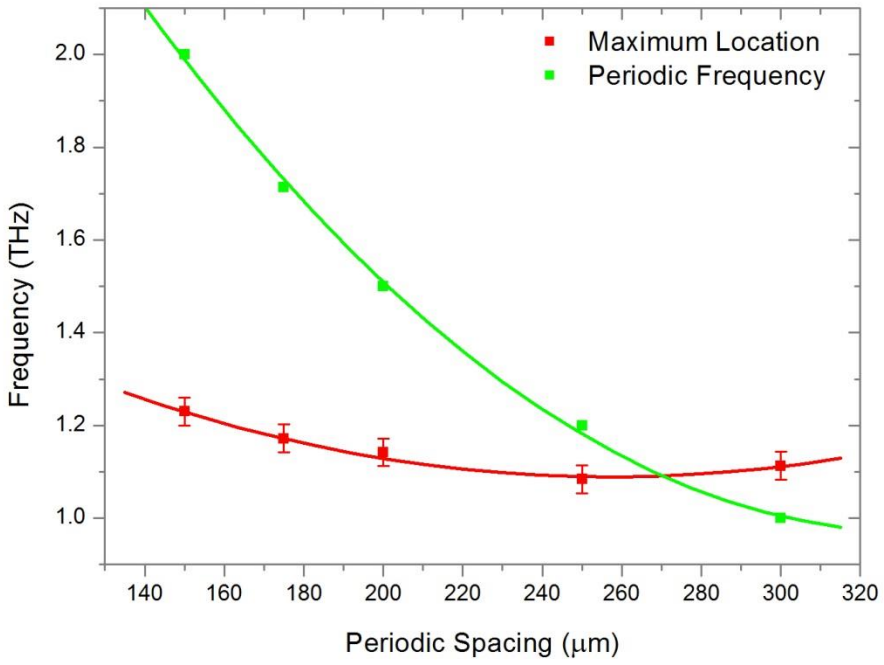

Figure 5.12: Frequency of peak transmission and periodic spacing of 125 x 25 μm aperture array at various periodic square lattice spacings.

Figure 5.12 shows the trend in peak transmission and minimum location as the periodic spacing is varied. As the minimum approaches the peak transmission it shifts to a lower frequency, until the two features cross and the peak returns to its position as described by the antenna waveguide mode, at largely suppressed transmission strength. The location at which the maximum and minimum are predicted to meet is 270 μm, an array with an approximate 5:1:11 ratio, or a periodicity slightly above double the aperture length.

A similar experiment has been conducted at the two extremes of the THz-TDS frequency range achieved by the Durham THz-TDS system. Using 5:1 ratio apertures of 200 x 40 μm and 75 x 15 μm size creates transmission peaks at 0.75 THz and 2 THz respectively, spaced in

various periodic square lattices of similar ratio to those of the 125 x 25 µm apertures. The measured normalised transmission spectra are shown in Figure 5.13 and show a similar trend to that observed in Figure 5.7.

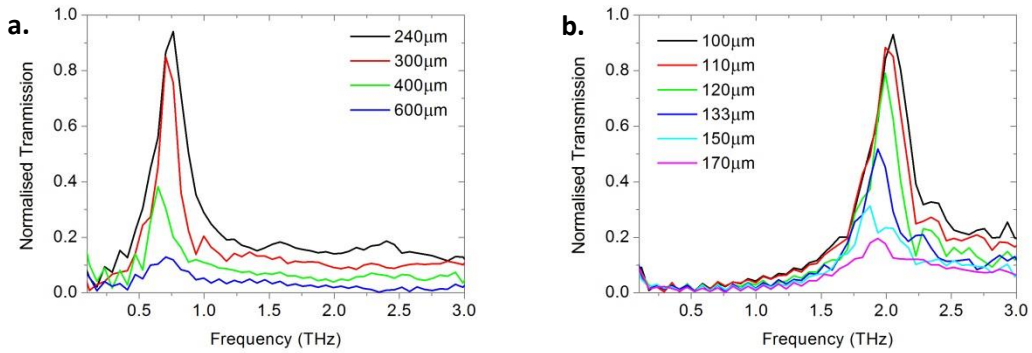

Figure 5.13: Normalised THz-TDS transmission of; a. 200 x 40 µm and b. 75 x 15 µm aperture arrays with varied periodic square lattice spacing.

From the spectra shown in Figure 5.13 we can obtain a similar measure of the crossing point of the transmission maximum and minimum locations for these varied aperture sizes, as shown in Figure 5.14. We again observe the movement of the maximum transmission location away from its aperture defined frequency as the minimum approaches until they meet and the transmission is mostly extinguished.

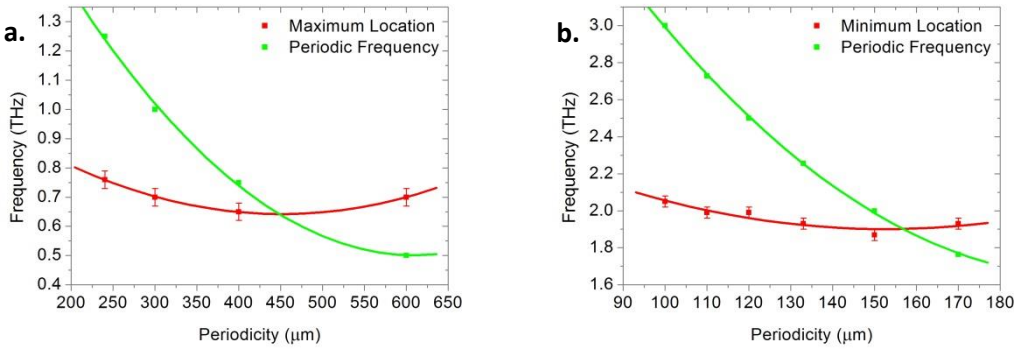

Figure 5.14: Frequency of peak transmission and periodic spacing of; a.200 x 40 µm and b. 75 x 15 µm aperture arrays at various periodic square lattice spacings.

Figure 5.14 shows the corresponding meeting points for the maximum and minimum locations for 200 x 40 µm and 75 x 15 µm, respectively, to be 450 µm and 157 µm. These locations both closely relate to the previously observed approximate 5:1:11 ratio.

Comparison of the relative transmission peak strengths across all the measured aperture arrays can be achieved by normalising against the array's ratio. By defining each array by its periodic spacing as a ratio to its 5:1 aperture size, we obtain Figure 5.15.

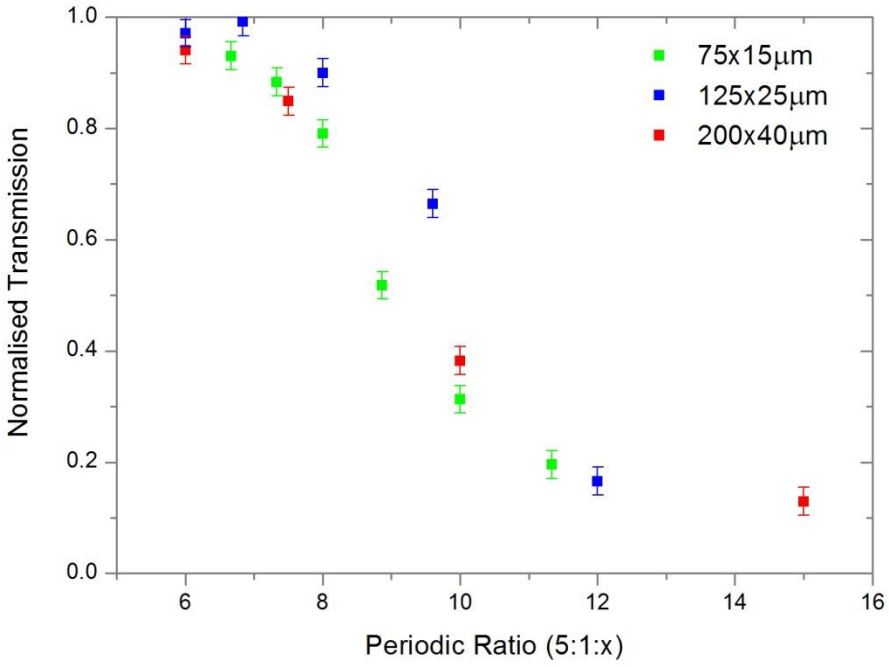

Figure 5.15: Normalised THz-TDS transmission peak strength of 5:1 apertures of various sizes at varied periodic spacings.

From Figure 5.15 we can observe that all measured 5:1 aspect ratio periodic aperture arrays display a similar trend in normalised transmission peak strength in the measured region. At a square lattice periodic spacing of approximately 7 times the aperture width a reduction in peak transmission strength begins, falling to < 20 % transmission once the periodic spacing is > 11 times the aperture width. This fall in transmission strength has been attributed to the existence of a minimum in transmission defined by the free space wavelength of the periodic spacing.

5.4 Periodic Rectangular Lattice

Decoupling the x and y periodic spacing allows for further investigation into the source of the previously observed minimum. For a 125 x 25 µm 5:1 aspect ratio rectangular aperture array a minimum periodic spacing of 135 µm is imposed in the y direction as 10 µm of metal between apertures is at the lower limit for the fabrication outlined earlier in section 5.1. In the x direction, aperture width periodicity can begin as low as 35 µm. Setting the periodic spacing in the y-direction, normal to the electric field, at 135 µm and varying the periodic spacing in the x-direction creates aperture arrays with a rectangular periodic lattice.

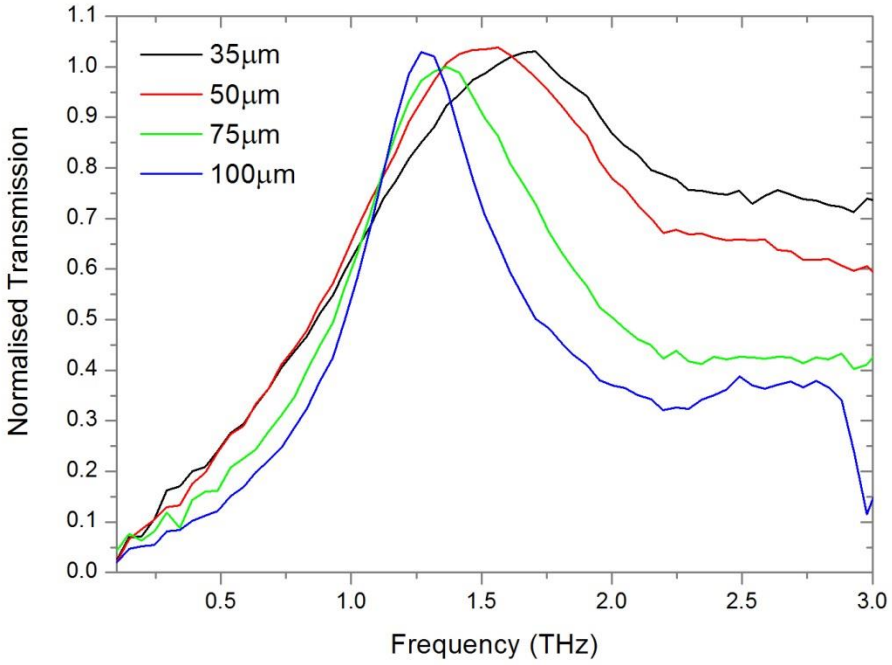

Figure 5.16: Normalised THz-TDS transmission of 125 x 25 µm aperture arrays with fixed 135 µm y-direction periodicity and varied x-direction periodic spacing. For 100 µm x-direction periodicty a clear minimum is observed at 3 THz.

In Figure 5.16 no strong minimum can be observed at a frequency related to the 135 µm y-direction periodic spacing (≈ 2.22 THz); however, for a 100 µm x-periodicity we observe a sharp minimum at 3 THz. With only 10 µm of metal between individual 125 µm high apertures in the y-direction and small x-periodicities the aperture density of the array is

high. Therefore, there is a high transmission of frequencies above the aperture waveguide resonance. This high transmission makes it possible to observe minima more clearly. Figure 5.17 shows the normalised transmission for these aperture arrays calculated by Lucifer FDTD simulation. Lucifer shows a small but consistent dip in transmission close to 2.22 THz, relating to the y direction periodicity, as shown by the dashed black line. While displaying the characteristic minimum at 3.0 THz for a 100 µm periodicity, Lucifer presents a large resonant feature immediately before this minimum, similar to that previously observed for the Lumerical FDTD solutions. However, this feature is not observed in THz-TDS measurements, presumably due to losses in the real metal.

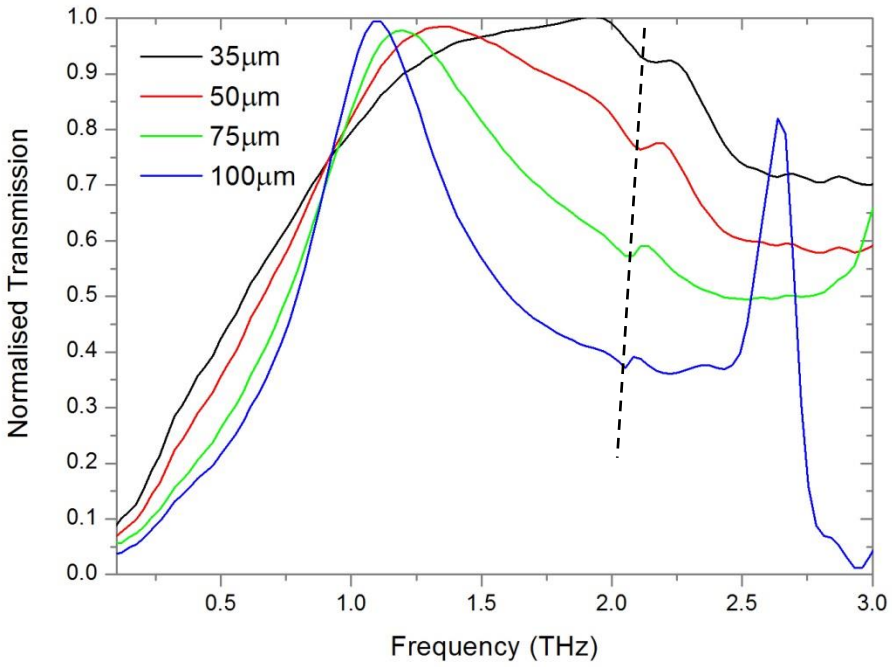

Figure 5.17: *Normalised FDTD transmission of 125 x 25 µm aperture arrays with fixed 135 µm y direction periodicity and varied x direction periodic spacing obtained by Lucifer. For 100 µm x-direction periodicty a strong resonance followed by a minimum is observed just below 3 THz.*

Figure 5.18 once again shows good matching between THz-TDS measurements and Lucifer FDTD simulations in terms of general spectral shape. However the peak position is less well

matched to those in Figure 5.9. With only 10 µm of metal between the free space apertures in the y-direction, it is assumed the real metal arrays experience loading between neighbouring apertures. The transmission peak shifts to a higher frequency than that defined by a single aperture waveguide as the array approaches the 1D slot case [84].

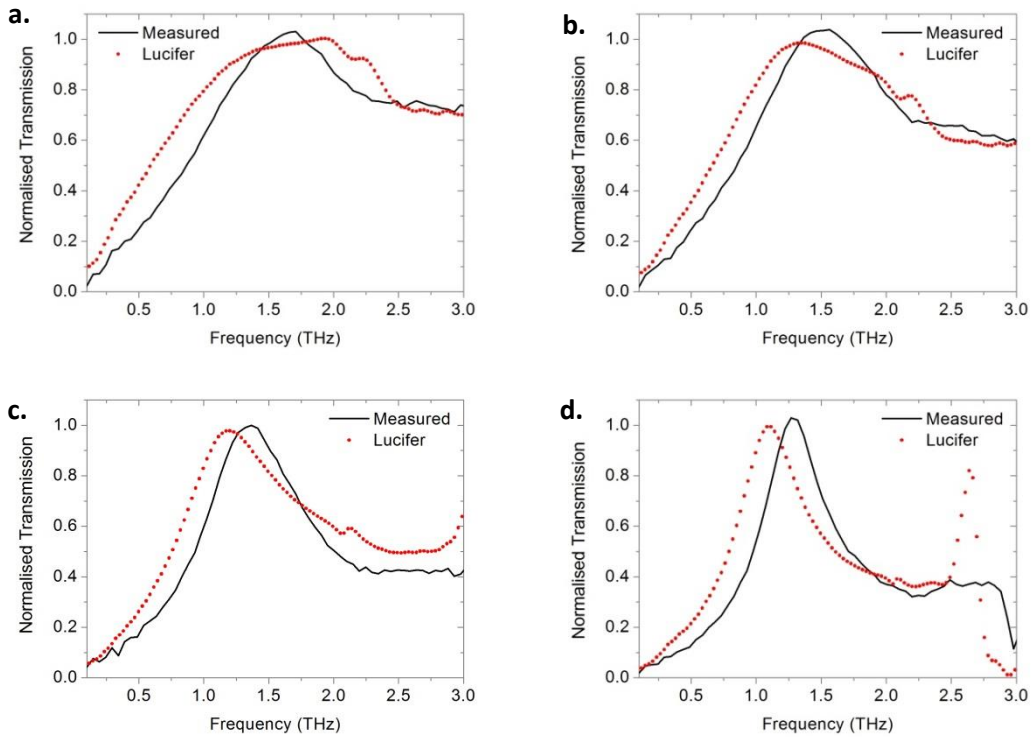

Figure 5.18: Normalised THz-TDS transmission of 125 x 25 µm aperture arrays with fixed 135 µm y direction periodicity and varied x direction periodic spacing compared to Lucifer FDTD simulations. X direction periodic spacing; a. 35 µm, b. 50 µm, c. 75 µm, d. 100 µm.

5.5 Conclusions

The transmission properties of periodic arrays of 5:1 aspect ratio slot apertures have been extensively measured by THz-TDS techniques and compared to FDTD simulations. The transmission peak has been found to be well defined by the aperture waveguide mode as discussed in section 3.8 and achieves > 95% transmission at this peak frequency for well-matched periodic spacings. The greatest observed transmission normalised to free space aperture area is >12, achieved by a 125 x 25 µm rectangular aperture spaced at

200 μm in a periodic square lattice. This transmission respective to free space area is greater than that predicted for a single 5:1 aspect ratio rectangular aperture [79]. For a periodic square lattice of ratio 5:1:≤7 the predictions of Ruan [80] match the experimental results well.

The x-direction, parallel to the electric field and short antenna edge, periodic spacing has been shown to introduce a minimum, well defined by the free space wavelength. This minimum, determined to be the excitation of the fundamental THz SPP mode, has not been found to enhance the transmission properties of the free-standing metal array, which shows > 95% peak transmission when far removed from SPP resonant frequencies.

As the minimum approaches the location of the slot antenna resonance the transmission peak is shifted to a lower frequency and the peak sharpened. At a periodic spacing found to be ≈ 11 times the slot width for a 5:1 aspect ratio the maximum and minimum locations intersect and the transmission peak is effectively extinguished. All of these transmission properties are well-matched by FDTD simulations using PEC approximations for the free standing aperture array.

Chapter 6

Controlling SPP Minima

By introducing an angle of incidence between the THz beam and free standing copper aperture array, it is possible to change the frequency of excited SPPs. This was demonstrated in 1902 [48]. The interaction of surface plasmon modes with the localised shape resonance dominated transmission spectra, as presented in chapter 5, will be investigated further by manipulation of the SPP frequency. The VNA measurement techniques discussed in chapter 2 will be used to provide high frequency resolution measurements, allowing for accurate observations of small changes in spectral shape.

While the localised shape resonance of a single rectangular sub-wavelength aperture depends solely upon its height and width, an array of such slot antennas causes coupling between adjacent antennas. The extraordinary optical transmission (EOT) of such an aperture array is determined in chapter 5 to be coupled to the periodic arrangement of the

aperture (and, by extension, the existence of SPPs). However, its resonant transmission does not arise from periodic spacing, and a single slot displays a strong resonance. The excitation of SPPs in the terahertz (THz) region relies upon the periodic patterning of a metallic surface in order to manipulate the metal's effective plasma frequency.

The localised aperture resonant frequency is only loosely coupled to the angle of incidence between incoming radiation and the metal surface; however, it is critical to the frequency of excitable SPP modes. By varying the angle between the free standing metal foil and incident THz radiation, it is possible to vary the interaction between these resonant modes and further study the role they play in the EOT of rectangular aperture arrays.

6.1 Varying Incident Angle

The placement of the aperture array in the collimated 1" VNA free space THz beam, as outlined in chapter 2.2, allows for measurement of its transmission characteristics. With the electric field orientated to the x-axis and rotating about the y-axis, as shown in Figure 6.1, the incident angle between the THz beam and metal/dielectric interface can be altered. Starting at a normal incidence between the incoming THz beam and the metal foil, as in all chapter 5 measurements, the incident angle is increased in 5 degree increments up until 35 degrees. 35 degree is determined the upper bound for fully containing the 1" free space beam within the ~2" array to ensure the free space normalisation is valid. As the incident angle is altered the changing transmission of the aperture array is measured. The interaction between the aperture resonance and SPP mode is controlled and studied.

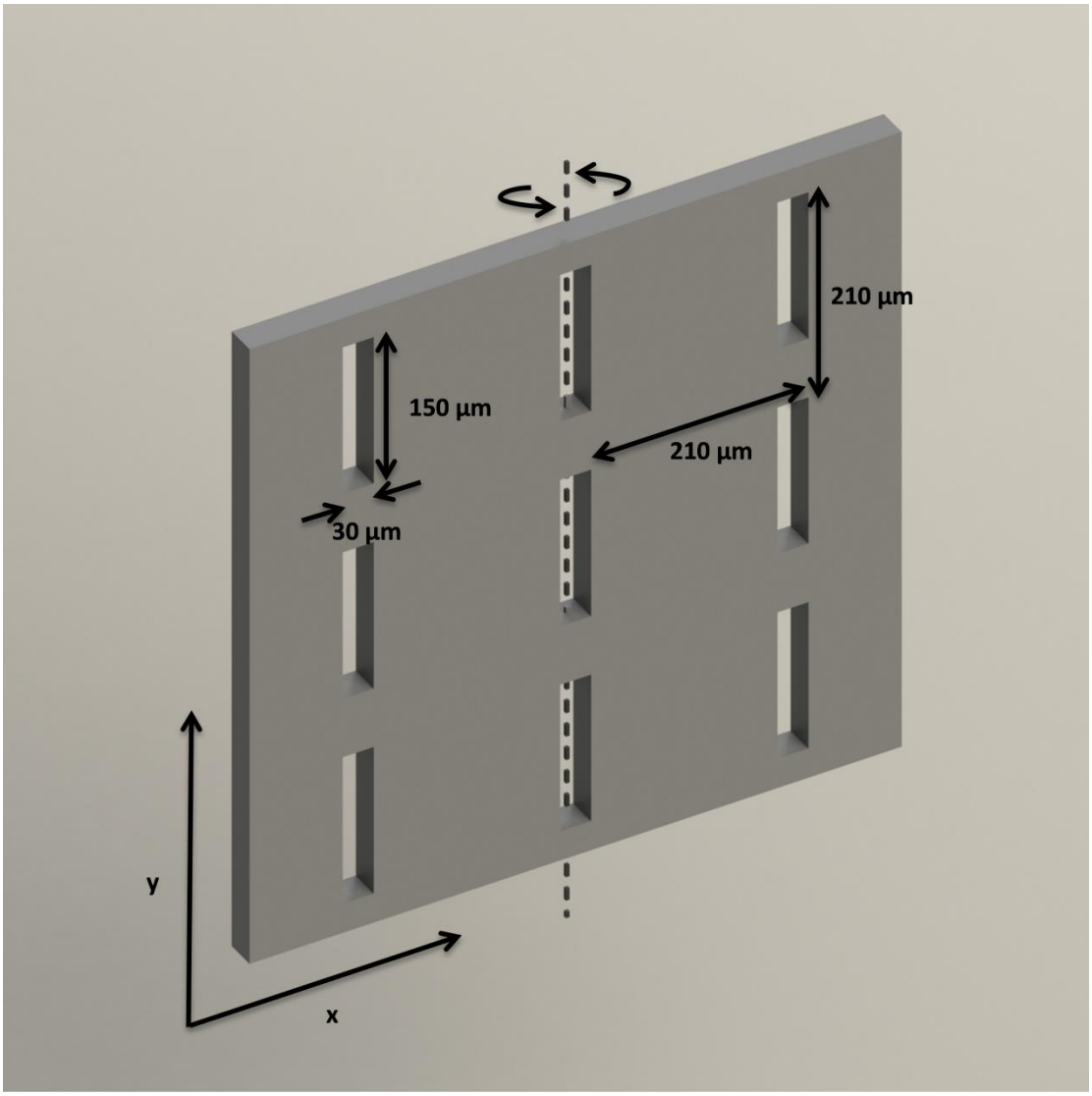

Figure 6.1: Experimental orientation of free standing copper aperture arrays.

From the previous investigation into the origin of transmission features at normal incidence, chapter 5, a ratio of slot width : slot height : periodic spacing of 5:1:7 is known to give a slot antenna resonance with >90% transmission at a wavelength very close to double the slot height. Setting the slot height to 150 µm, giving a slot width of 30 µm and square periodic lattice of 210 µm, creates a resonant TE_{10} waveguide mode of 300 µm, or 1 THz, and an SPP frequency of 1.43 THz.

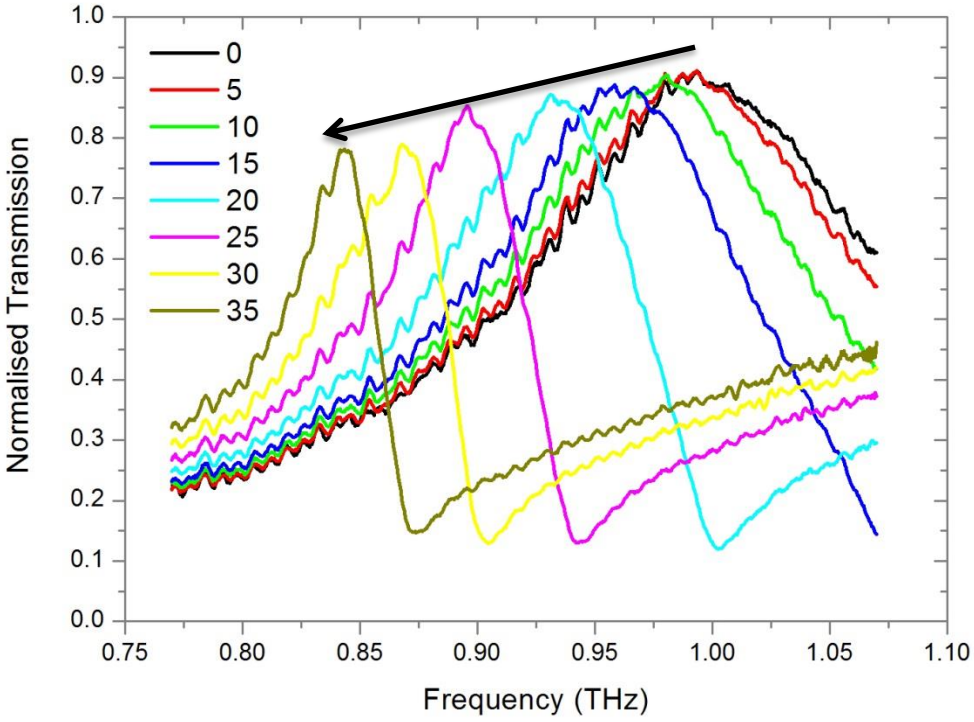

Figure 6.2: 210 x 210 µm square lattice aperture array at varied incident angle to electric field.

Figure 6.2 shows a characteristic slot antenna array resonant peak at 1 THz when normally incident to the collimated electric field, (black trace, 0^{o} incident angle). As the free standing array is rotated about its y axis, as shown in Figure 6.1, the peak's maximum transmission falls by 13% while the frequency is reduced by 150 GHz. This change in peak strength and position is caused by the changing frequency of the SPP induced minimum with angle dependence. The changes in peak transmission strength and position are accompanied by the introduction of a sharp minimum as the incident angle increases, observed for 20 degree incident angles and above in the VNA range. As the incident angle is increased, the frequency at which the minimum occurs approaches that of the maximum causing a steep roll-off to the right-hand side of the maxima. This change in spectral shape is very difficult to observe in a THz-TDS FFT, as used in chapter 5, due to the high frequency resolution required to observe such a sharp minimum.

The implementation of an incident angle between a periodic aperture array and the incident electric field in an FDTD simulation is, as discussed in chapter 4, difficult due to the inability to rotate either a single cell or the source about a single cell. However, the implementation of such a simulation has been achieved for a 7 x 7 array of such sub-wavelength apertures. Figure 6.3 shows that Lucifer FDTD simulations do not accurately capture the changes in transmission peak shape observed by THz-VNA for real arrays as the incident angle is changed. Over the VNA's limited frequency range the Lucifer FDTD solution does not capture the introduction of the SPP minimum or the large changes to transmission resonances caused by it.

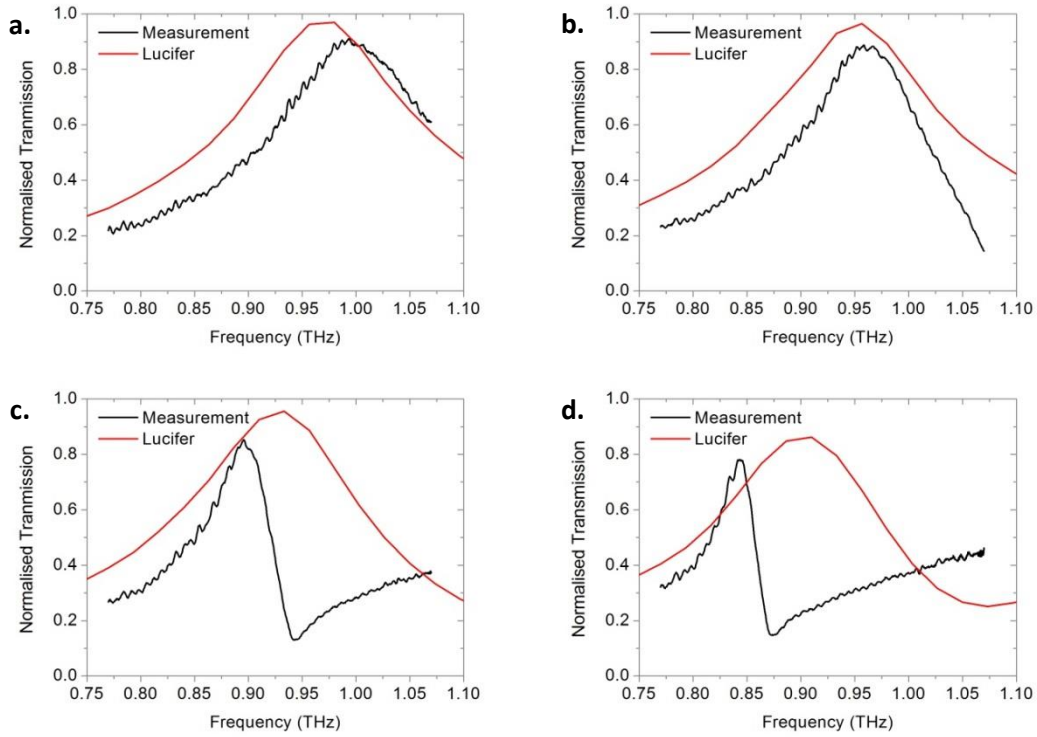

Figure 6.3: 210 x 210 µm square lattice aperture array as measured by THz-VNA and Lucifer FDTD transmission at; a. Normal, b. 15 degree, c. 25 degree and d. 35 degree incident angle.

Figure 6.4 shows that minima are present, and strongly angle dependent, in the Lucifer FDTD solutions when viewed over a larger frequency range. FDTD comparisons to THz-TDS data in

chapter 5 (Figure 5.18) show that Lucifer is able to accurately match experimental observations for the location of SPP minimum at normal incidence.

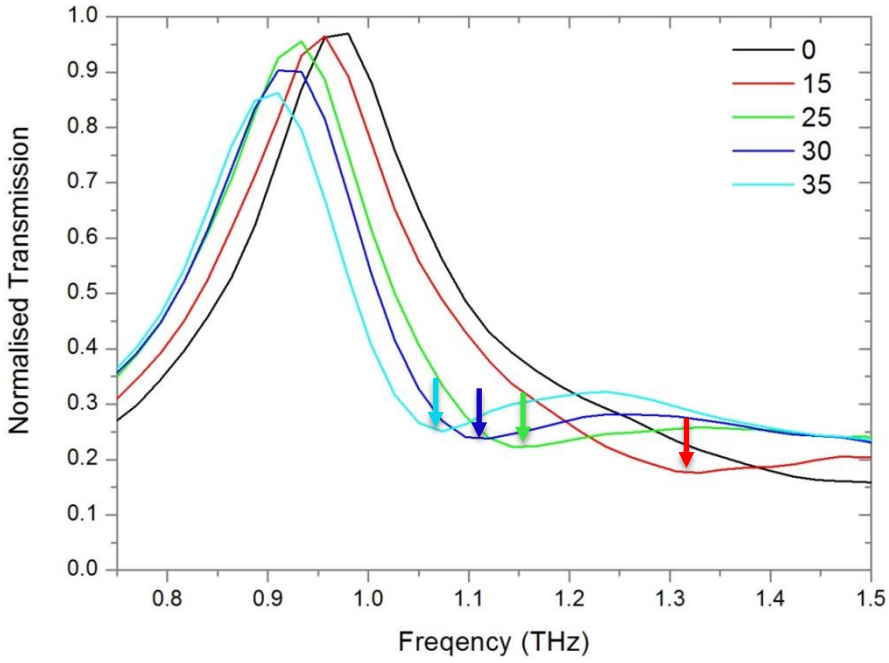

Figure 6.4: Lucifer FDTD simulation of 210 x 210 µm square lattice aperture array at varied incident angle to electric field. The location of SPP induced minima is indicated by the arrows.

Concerns that the differences observed for increasing incident angle arise from differences in the CW frequency domain measurements used in THz-VNA methods and the time-domain measurements used by FDTD are disproved by a similar simulation run at Imperial College London under CW frequency domain conditions. Produced by another commercial simulation package, Computer Simulation Technology (CST), the CW results show broadly similar trends to Lucifer, with a resonant peak mostly insensitive to angle, accompanied by a strong feature at a higher frequency, reducing in frequency as the incident angle is increased, (Figure 6.5).

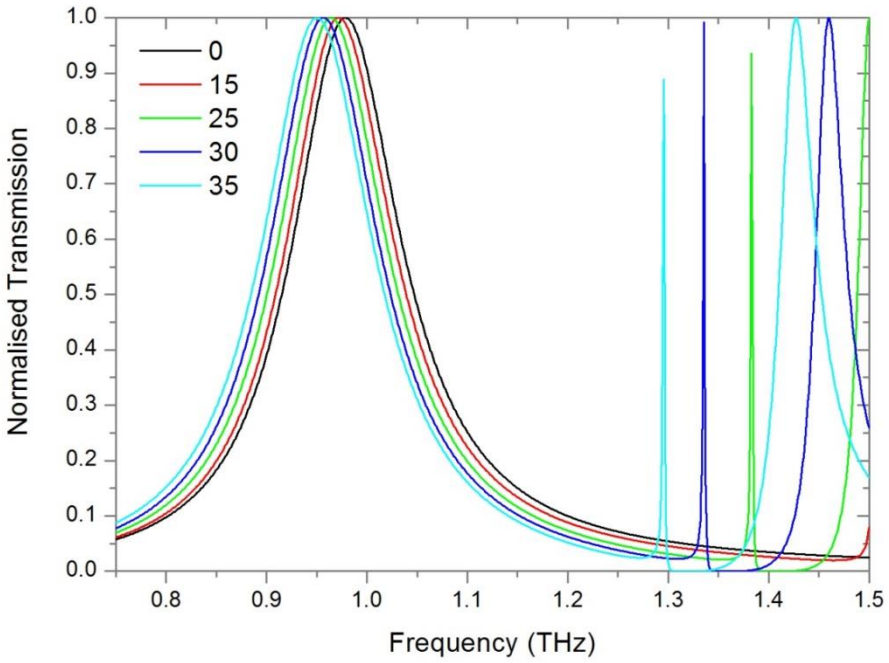

Figure 6.5: CST frequency domain simulation of 210 x 210 µm square lattice aperture array at varied incident angle to electric field.

Presented in CST as a very strong resonance, approaching unity in strength but extremely narrow, THz SPPs are a dominant resonant feature of these simulations.

The CST CW solution finds a steady state response, as opposed to a pulse response produced by FDTD, in which infinitely propagating (due to the PEC approximation) SPP modes can approach unity in strength. Such a mode in a real array is limited by its non-infinite structure and decay losses in a real metal. This explains why such strong, sharp resonant modes have not been observed for real arrays measured in this thesis. However, it does not explain the discontinuity between the observed and simulated SPP resonance dependence upon incident angle.

6.2 Effect of Surface Quality

If the minima observed in this chapter are due to the excitation of THz SPPs, these surface modes should be dependent upon the conditions at the metal-dielectric interface on both the front and back faces of the free standing array, as discussed in chapter 4.

Relating back to the initial observations of chapter 5, Figure 5.6, the transmission peak for two independently fabricated and tested arrays was found to be extremely well matched. Differences are observed however in the transmission at ~1.7 THz, now attributed to an SPP minimum. This minimum is found to be far more sensitive to differences in samples than the transmission peak controlled by aperture resonance.

Throughout this thesis, the fabrication process presented in section 5.1 and used for all the aperture arrays in this work has strived to minimise array defects. Minimising the number of defects in the copper foil, created during the electroplated process, is dependent upon introducing as few defects as possible at each stage of the fabrication. However, the process is not perfect and some defects are apparent in Figure 5.2a.

In an attempt to gain a greater understanding of the role these defects may play in the transmission properties of the free-standing copper arrays, more defects were introduced deliberately to the copper arrays. The most controlled method of increasing the number of defects in the copper surface is to change the electroplating conditions given in chapter 5.1. By increasing the current density applied, from 15 mA/cm^2 to 25 mA/cm^2, while maintaining a constant total current, it is possible to create a copper foil of the same thickness with more defects upon the top face. The surface quality of the copper under the various plating conditions can be seen in Figure 6.6, imaged by a Zygo white light interferometer.

The number of defects upon the opposite face is controlled by the surface quality of the Ti/Au seed layer onto which the foil is electroplated; it is, therefore, far smoother than the foil's top face under any plating conditions.

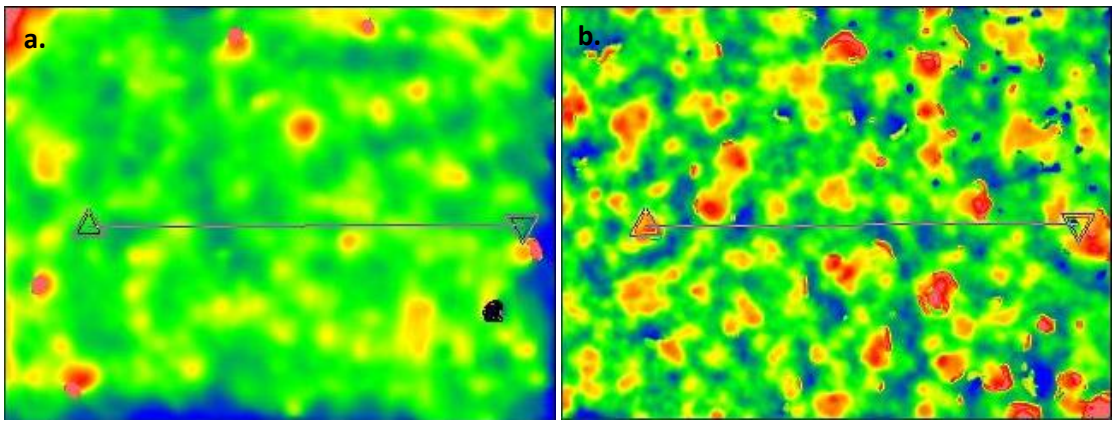

Figure 6.6: White light interferometer images of the copper foil surface under; a. normal conditions b. increased current.

Sample	RMS (nm)	Ra (nm)
15 mA/cm^2 Top Surface	30.5	17.3
15 mA/cm^2 Seed Layer Surface	1.0	0.8
25 mA/cm^2 Top Surface	106	80.3
25 mA/cm^2 Seed Layer Surface	0.9	0.7

Table 6.1: Surface roughness of copper foils under varing depositions parameters.

Table 6.1 gives the figures of merit produced by the Zygo white light interferometer for the copper foils under different fabrication conditions. The top surface produced at a higher plating current has been found to contain 3-4 times as many defects as that under normal plating conditions, and 100 times those found upon the seed layer surface.

It can be seen from Figure 6.7a that the surface quality of the copper causes no observable effect upon the transmission spectra of the array at normal incidence. The localised aperture resonance is unchanged by the surface properties of the array when far removed from the SPP resonance. As an increasing incident angle is introduced, Figure 6.7b-f, we observe a clear difference between the higher plating current sample (high defect density) and the

array with normal plating conditions (low defect density). The high defect array shows lower minima, constant around 12% transmission for the observable range, by comparison to 15% for the low defect array. Despite showing near identical normal transmission spectral shape and strength, the minima of the high defect array is observed at consistently lower (~50 GHz) frequencies than the low defect array. The alignment of the high defect side to be facing either the source (defects front) or receiver (defects back) can be seen to have no noticeable effect upon the minima or transmission peak.

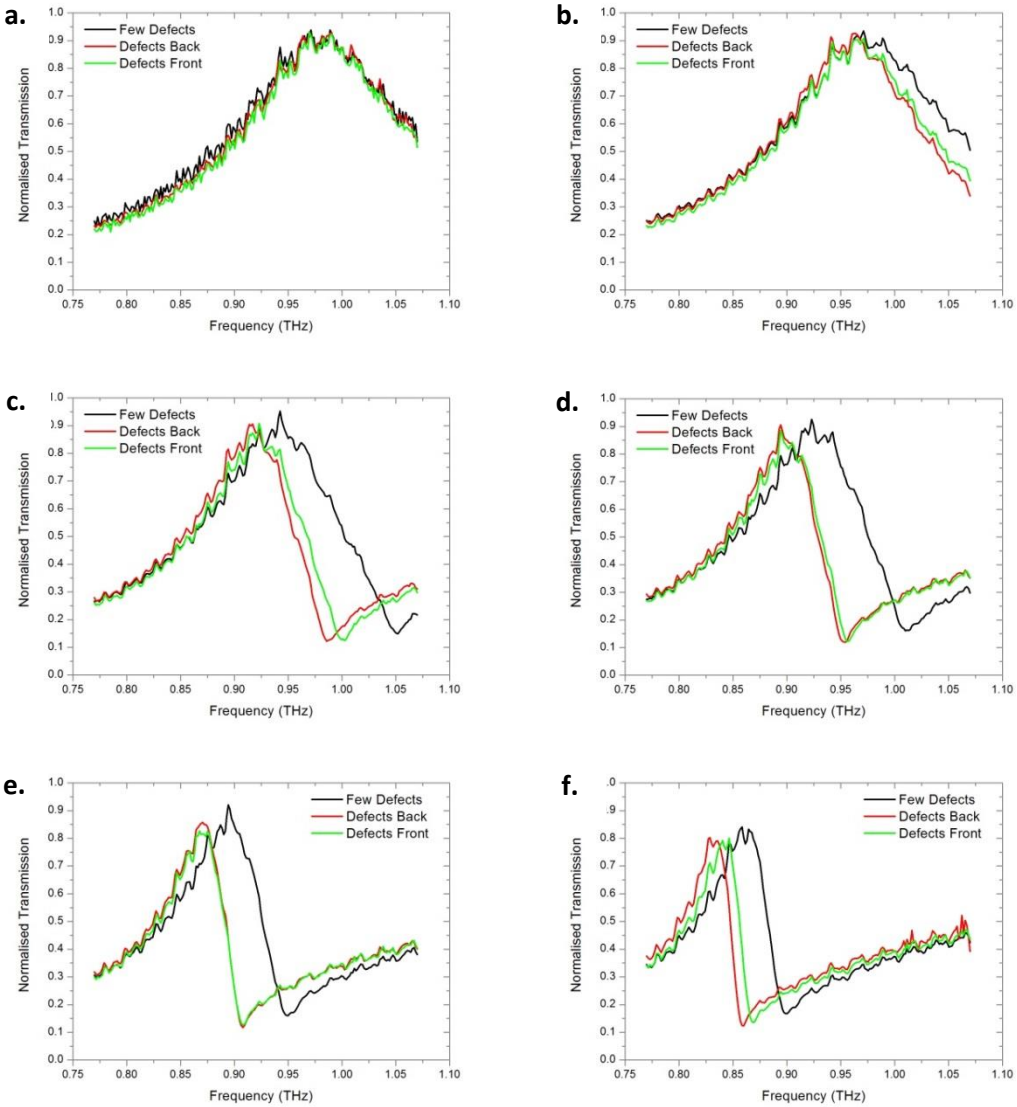

Figure 6.7: Effect of surface quality on transmission spectra at varied incident angle a. Normal b. 15 degree c. 25 degree d. 30 degree e. 35 degree f. 40 degree.

The observed trend in Figure 6.7 gives a good indication as to the source of discrepancies between the simulated and measured position of the SPP minimum as the incident angle is varied. A copper array containing a higher number of surface defects on either face has been found to shift the minima location and increase its strength over that of an array where defects are minimised. This is consistent with SPP sensitivity to the conditions at the metal-dielectric boundary. This result indicates that the discrepancies between Lucifer and VNA measurements could be due to the unavoidable defects in the real free standing copper array. The perfectly flat PEC approximation used by Lucifer cannot account for the increased confinement of the SPP into the metal caused by random deeply sub-wavelength features.

Continued development of Lucifer and Lumerical simulations looks to implement such deeply subwavelength features. However, it requires complex meshing solutions to achieve the required resolution without vastly reducing the cell size, and therefore increasing the memory requirements.

6.3 Randomly Located Aperture Array

If the resonant transmission peak of a free standing copper aperture array can be attributed to the localised aperture geometry, and a limited interaction with its neighbouring apertures, then the array should continue to show EOT with the removal of any periodic arrangement. However, if the sharp minima previously observed in this chapter are a result of the periodic pattering of a metal to allow the excitation of SPPs at THz frequencies, then removal of the periodic pattern should remove the minima.

To achieve an array with aperiodic spacing of aperture, a 5 x 5 set of 150 x 30 µm apertures in a 210 µm square lattice was chosen. Each aperture was then randomly located in its 210 x 210 µm cell by the application of a random (multiple of 5 µm) x and y movement from its

centre point, limited to ±25 µm and ±85 µm respectively. This random arrangement of 5 x 5 apertures maintains the same aperture density as previously used square lattice arrays with a ratio of 5:1:7. The individual shape of each aperture is maintained keeping 10 µm minimum of metal between each aperture but no fixed period can be established between neighbouring features.

The resultant 5 x 5 aperiodic arrangement of apertures is shown in Figure 6.8. This random 5 x 5 arrangement is then repeated to create an array >1", therefore larger than the THz beam. Creating a pseudorandom array with no fixed spacing between apertures but an overall repetition on a mm scale.

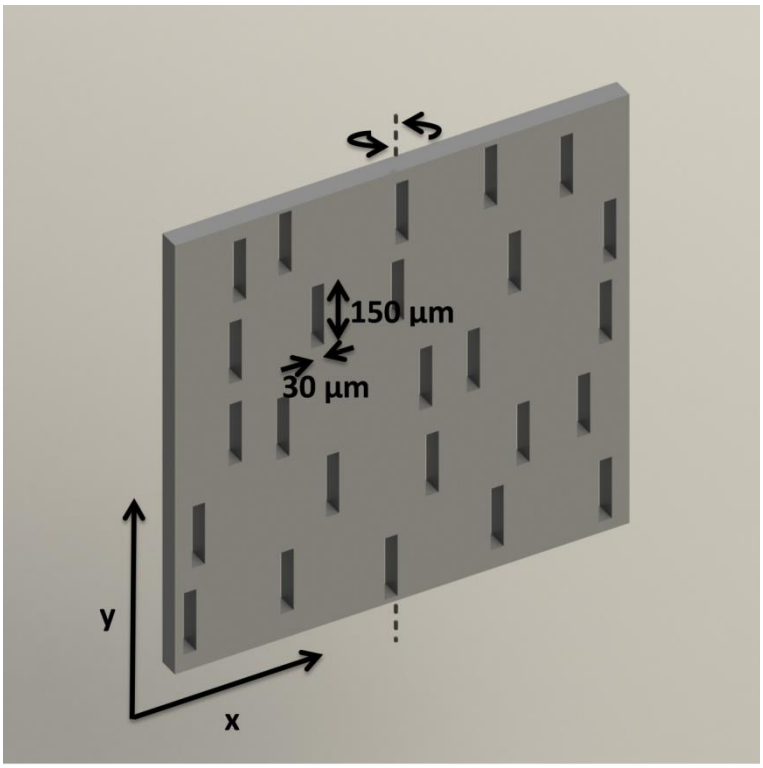

Figure 6.8: Repeating pattern of 5 x 5 randomly located 150 x 30 µm apertures.

Figure 6.9 shows the transmission spectra obtained for the random array, as given in Figure 6.8, as the angle of incidence to the electric field is varied. The random array of 150 x 30 µm apertures displays a resonant transmission close to the 1 THz predicted by localised aperture

resonance. The transmission peak strength is reduced to 68.1% by comparison to 93.6% achieved by the array given in Figure 6.2. These arrays share identical aperture size, shape and density. However, due to uneven spacing of the random array, each aperture does not have the same effective area due to neighbouring apertures. Therefore, not all apertures are able to achieve the same level of localised field strength.

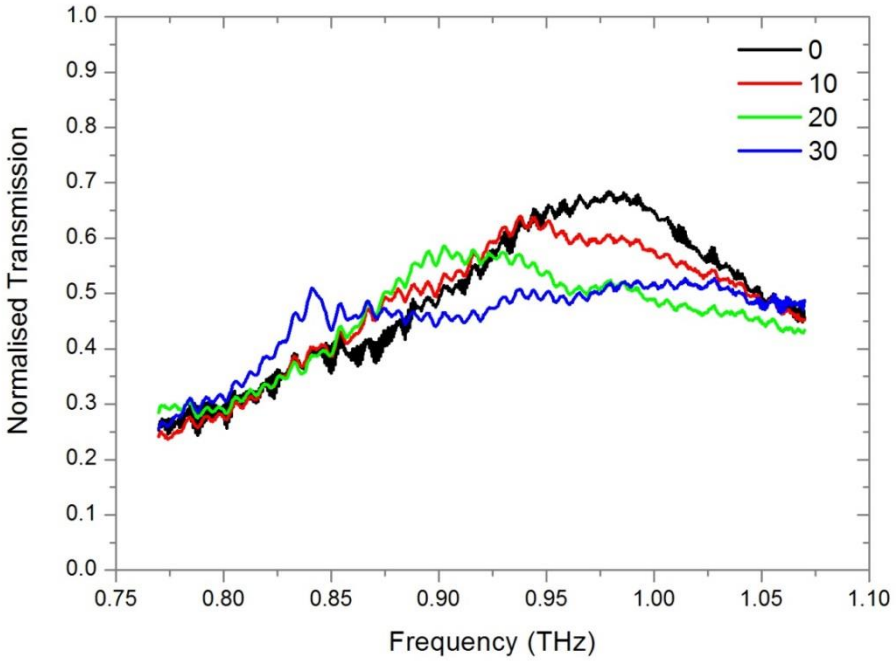

Figure 6.9: Aperiodic array of 30 x 150 µm apertures at varied incident angle to electric field.

As an angle of incidence is introduced, no sharp minima can be observed, and any small dips and changes in spectral shape can be attributed to random periodic spacings, allowing for some limited SPP excitation. These excitations are however controlled by many different spacings and therefore distributed across many frequencies.

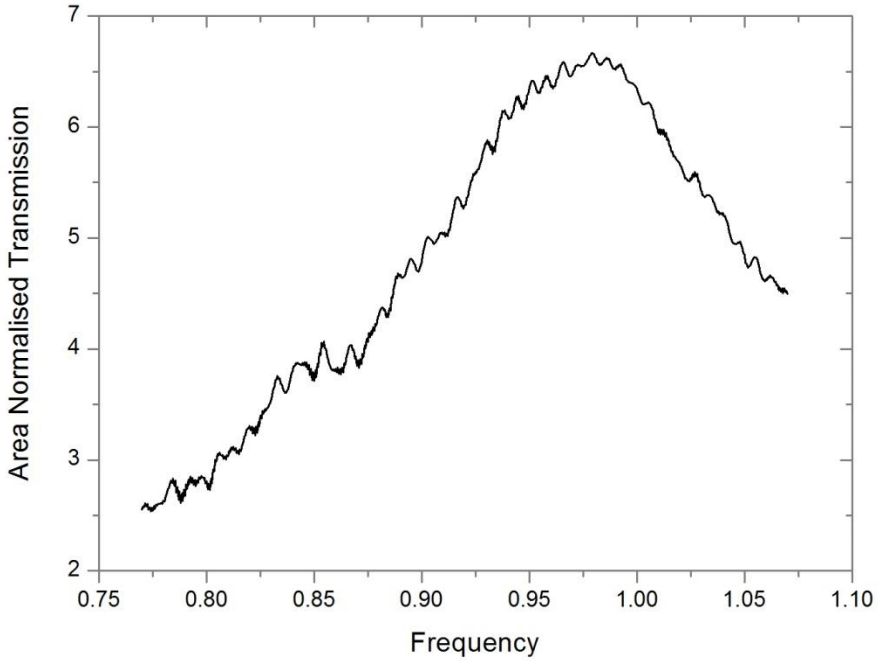

Figure 6.10: 5 point moving average of the tranmission from an aperiodic array of 30 x 150 µm apertures oriented perpendicular to the electric field, normalised to free space aperture area.

The transmission of the random array when normalised to aperture free space area is, as previously for all periodically arranged aperture arrays, significantly >1 and well within the definition of EOT, Figure 6.10. The EOT phenomena is, without a doubt, possible in the absence of a fixed periodic structure, a key requirement for THz spoof SPP excitation. Controlled by aperture dimensions, the TE_{10} waveguide mode of 5:1 aspect ratio rectangular apertures has been observed to provide the necessary transmission mechanism for EOT.

6.4 Varied Periodic Spacing

To manipulate the resonant frequency of SPP modes in the THz region a change in the periodic spacing parallel to the electric field, x-axis as shown in Figure 6.11, is required. A systematic variation in x-periodic spacing, keeping all other geometry constant, allows for

the spacing, or level of interaction, between the aperture resonance and SPP minimum to be varied.

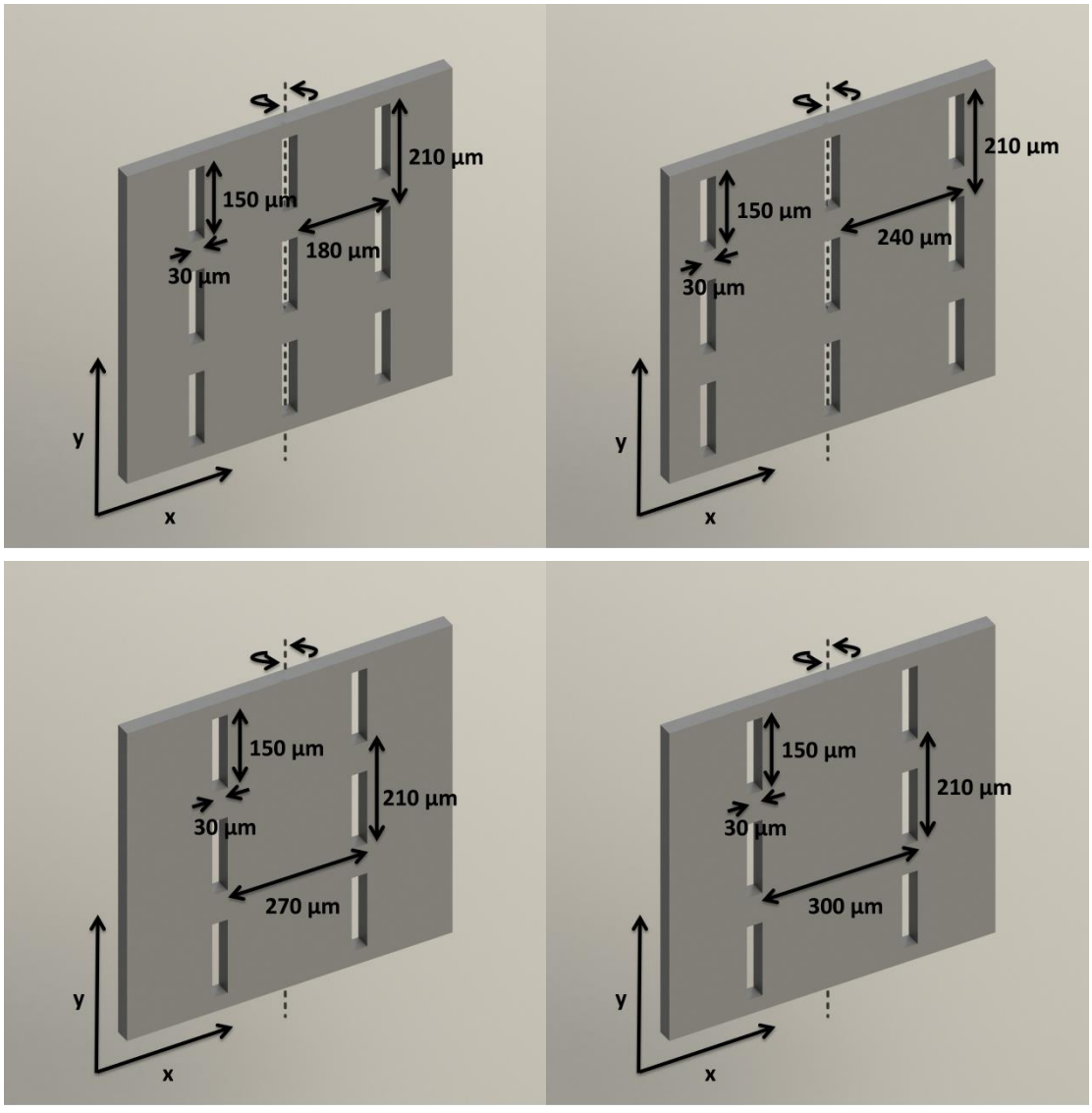

Figure 6.11: Geometry of free standing copper aperture arrays with varied x-direction periodicity.

Figure 6.12 shows the transmission spectra for an aperture array with a reduced periodic spacing, bringing the ratio of slot height : slot width : y-periodicity : x-periodicity to 5:1:7:6. As previously investigated in chapter 5, a reduction in periodic spacing causes a small rise in the localised aperture resonant frequency due to increased interaction between neighbouring apertures. By repeating the same experimental procedure of rotating the array about its y-axis the change in transmission spectra is observed.

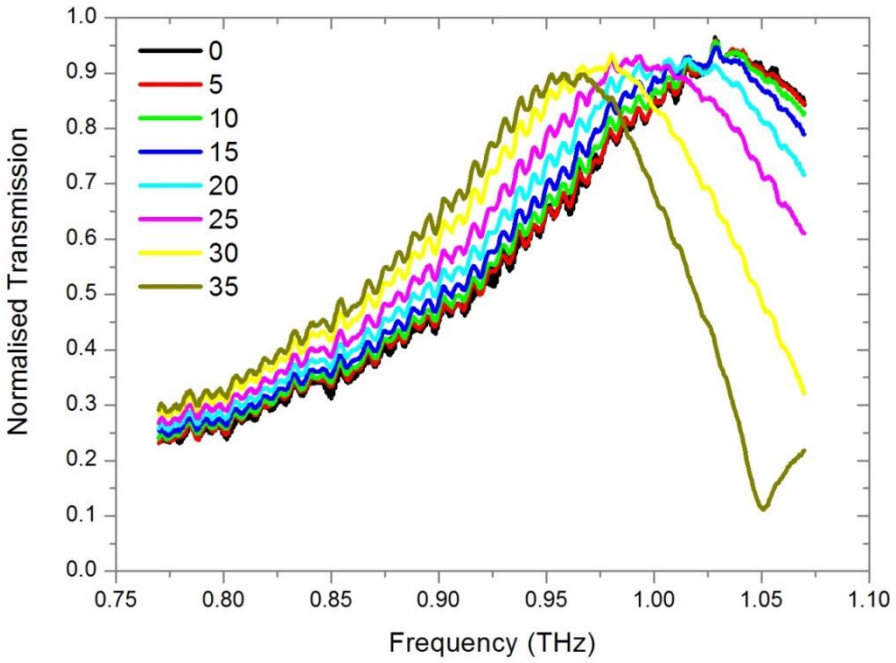

Figure 6.12: 180 µm periodic x-axis spacing at varied incident angle to electric field.

In Figure 6.12 we observe a marginally higher frequency peak than for the 210 µm square lattice array, caused by increased loading between neighbouring apertures. As the array is rotated, a reduction in peak frequency and strength is again observed; however, with a shift of 77 GHz and peak strength reduction of 4.1% this effect is much reduced. A sharp SPP minimum is observed at 35 degree. However, located further away from the maximum peak the change in peak shape is less pronounced than previously.

Figures 6.13 and 6.14 show the response of 2 more arrays this time with increased periodic x-axis spacing (with ratios of 5:1:7:8 and 5:1:7:9 respectively). As the arrays are rotated, the peak frequencies are shifted dramatically and largely reduced in transmission strength. Both arrays' transmission peaks are shifted beyond the frequency range of the VNA by 35 and 30 degree respectively. The peaks are observed to reduce in strength by >40% and are expected to continue this trend if observed at higher angles.

From as early as 10 and 5 degree incident angle respectively Figures 6.13 and 6.14 display sharp SPP minima. As in Figure 6.2, as this minimum approaches the localised aperture resonance we see a sharp transition between the two features, a large reduction in maximum peak strength and a change in the transmission peak's spectral shape.

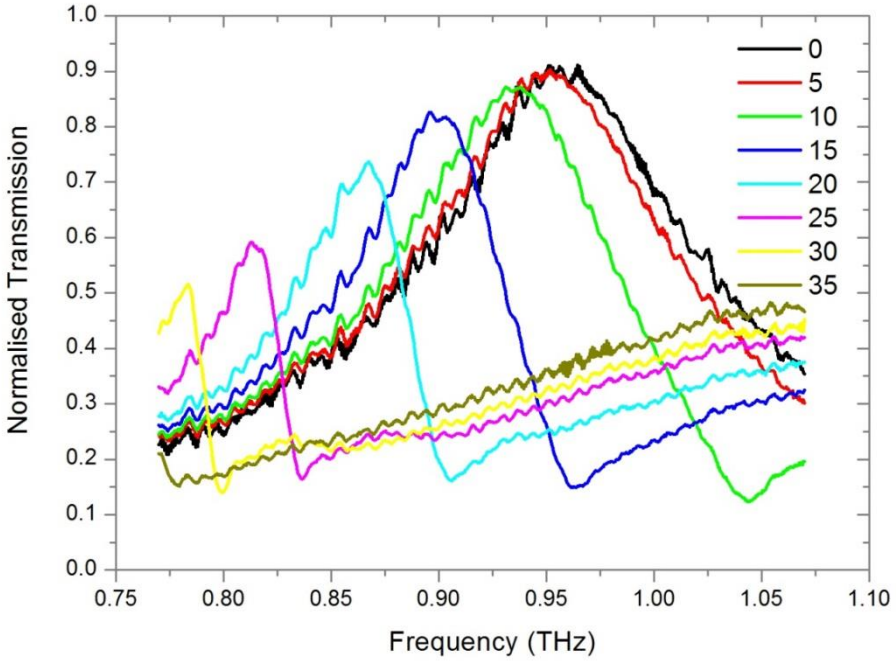

Figure 6.13: 240 µm periodic x-axis spacing at varied incident angle to electric field.

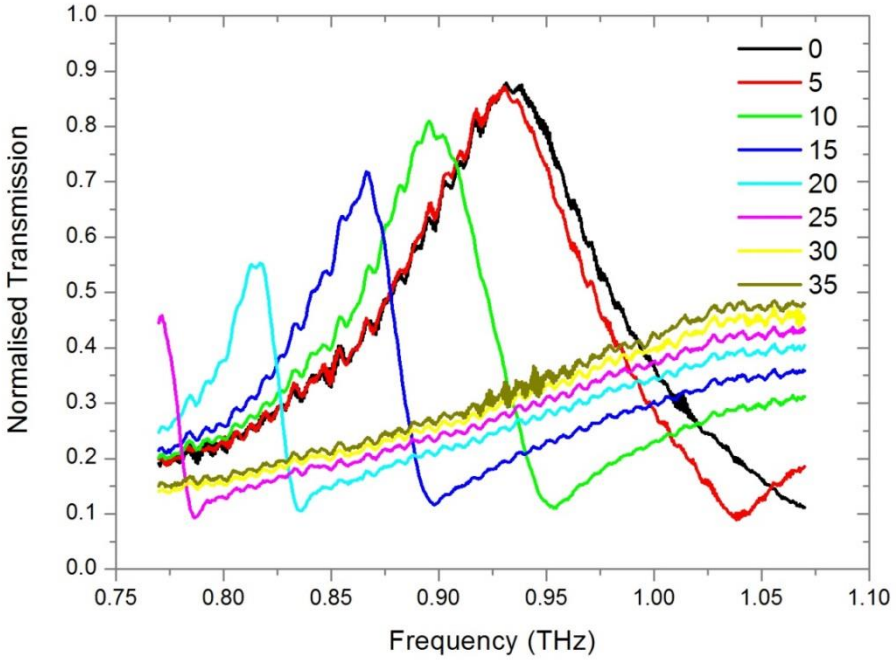

Figure 6.14: 270 µm periodic x-axis spacing at varied incident angle to electric field.

By increasing the periodic spacing in the x-axis again, an array is obtained with a ratio of 5:1:7:10; in this case the x-axis periodic spacing, 300 µm, is double that of the slot height, 150 µm. From Figure 6.15, a normal incident transmission peak is observed at 0.88 THz with a minimum located at 0.98 THz, the transmission peak is observed to fall to <35% by 10 degree incident angle as the distance between the minimum and maximum is again reduced.

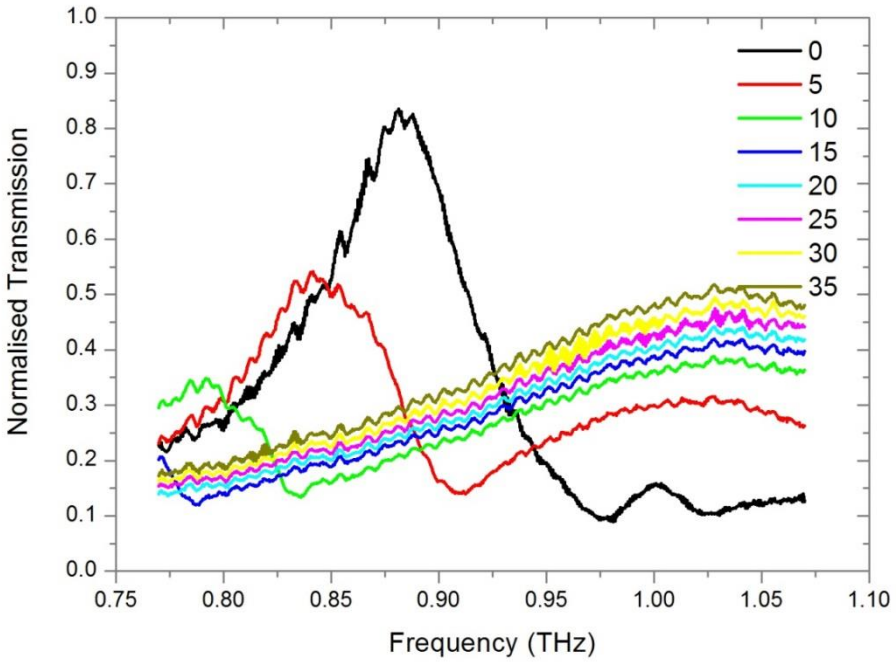

Figure 6.15: 300 µm periodic x-axis spacing at varied incident angle to electric field.

Figure 6.15 shows that it is possible to extinguish the localised aperture resonance by excitation of SPP modes at the same frequency. When the localised aperture resonance peak and the SPP minimum are located in close proximity the transmission peak strength and location becomes extremely sensitive to incident angle due to changes in SPP frequency. The SPP minimum frequency is also highly sensitive to changes in surface quality, as shown in section 6.2, and known to be dependent upon the dielectric properties at the metal interface. This makes an array with a 5:1:7:10 periodic ratio useful for many sensing applications.

6.5 Origin of Minima

Determining the trends which the SPP minima follow as the incident angle is changed can provide information as to the expected minima location when outside of the VNA frequency range. Figure 6.16 shows the frequency of the minima, where observed, in sections 6.1 and

6.4 by incident angle. By plotting a second order polynomial fit for each different periodic spacing, it is possible to obtain a second order response for each array, as shown in Table 6.2. By setting x, the incident angle, to zero for each of the quadratic responses it is possible to extrapolate the location of the minima at normal incidence for those arrays where it is not otherwise measureable due to the limited frequency range of the VNA.

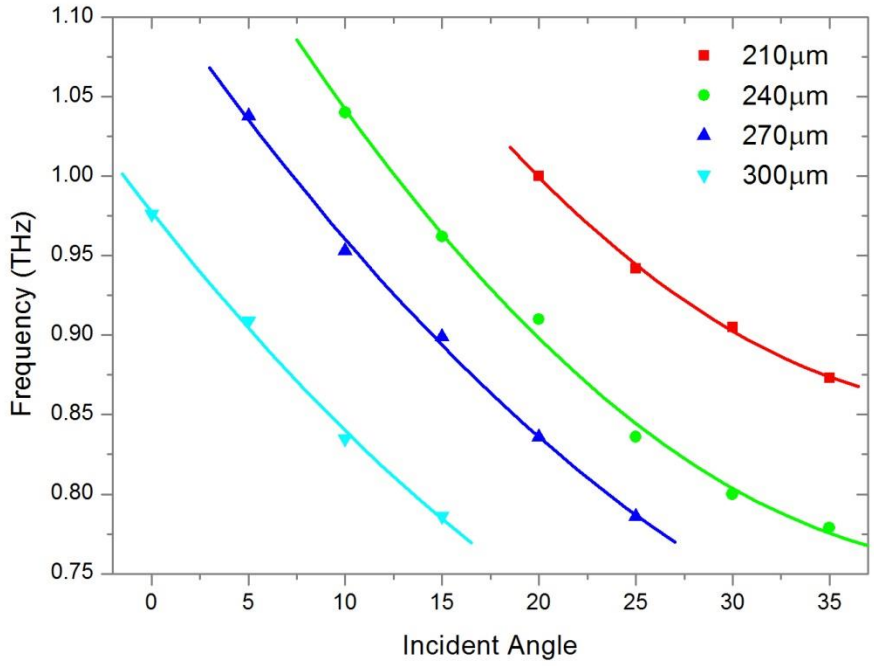

Figure 6.16: Minima in frequency against incident angle to electric field.

Periodic Spacing	***c***	***bx***	***ax^2***	***R^2 Fit***
210 µm	*1.35*	*-0.023*	*0.00026*	*0.999*
240 µm	*1.24*	*-0.022*	*0.00025*	*0.995*
270 µm	*1.12*	*-0.018*	*0.00017*	*0.998*
300 µm	*0.98*	*-0.016*	*0.00018*	*0.998*
210 µm (adjusted)	*1.41*	*-0.027*	*0.00033*	*0.999*

Table 6.2: Quadratic response of minima locations as observed by VNA transmission for varied periodic spacing.

The constant, c, response (normal incidence, x=0) of the 240, 270 and 300 µm arrays corresponds very closely to the free space frequency of a wave with their respective wavelengths; 1.25, 1.11 and 1 THz respectively. The response of the 210 µm function is further from that predicted by its periodic spacing; 1.43 THz compared to 1.35 THz for its constant, c. This is attributed to a limited number of minima locations for this array. If we return to Figure 6.2 it can be assumed that the 15 degree incident angle trace is tending to a minimum just above the maximum frequency range of the VNA. Figure 6.17 shows the effect of adding an additional data point at 15 degree for 210 µm at 1.08 THz, just beyond the VNA's measured range and a conservative estimate for the minima location by comparison to the observed trends. Recalculation of the quadratic response including this new data point is given in Table 6.2 as 210 µm adjusted. A normal incidence response of 1.41 THz much closer to the 1.43 THz predicted by a 210 µm wavelength is achieved.

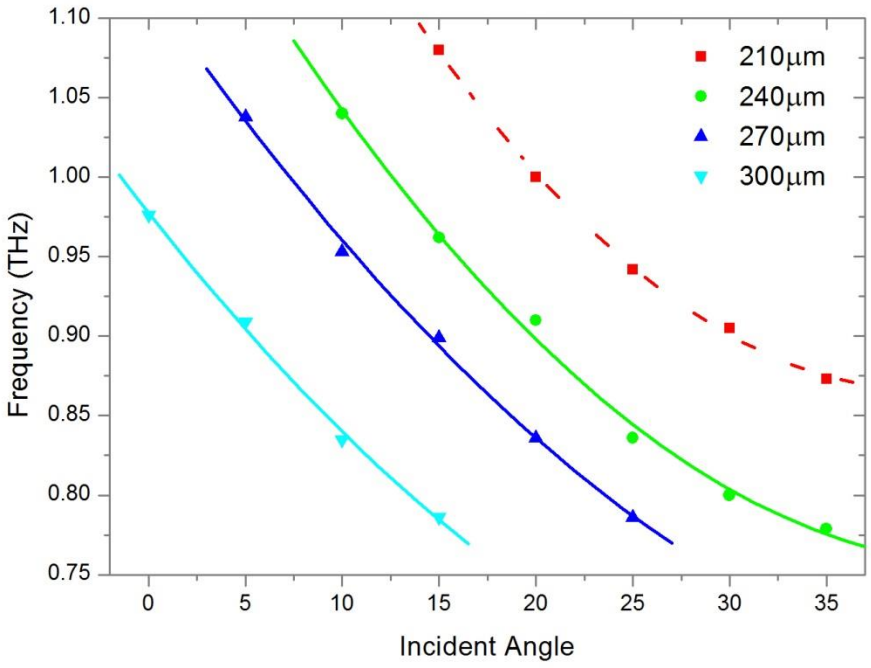

Figure 6.17: Minima in frequency against incident angle to electric field adjusted fit for 210 µm array.

From the extrapolated position of the observed minima at normal incidence, constant c (x = 0) it can be seen that the minima's origin clearly lies in its periodic x-axis spacing. This strongly agrees with the theory that the minimum is introduced by the excitation of spoof THz SPP upon a periodically patterned material. Once coupled to the surface this mode is no longer available to be coupled into the aperture's waveguided mode and therefore is a minimum in transmission.

6.6 Conclusions

This chapter has shown that it is possible to excite and control SPPs at the interface between a metal and air at THz frequencies by the periodic arrangement of 5:1 aspect ratio slot apertures. While the waveguide frequency of a single sub-wavelength aperture is loosely defined by the angle of the incident THz radiation, the SPP frequency is strongly dependent upon it. This allows for the interaction between the two resonant features to be varied by incident angle alone, and no changes to geometry are required.

Sharp transmission resonances, that usually characterise SPPs, have not been observed in the far-field transmission measurements conducted in this thesis. The confinement of the SPP into the free standing copper foil and the losses incurred by this non-ideal material are presumed to extinguish the resonance observed in PEC simulations. Instead, what is presented is EOT in free standing copper foils perforated by sub-wavelength apertures dominated by localised aperture resonance.

The phenomena of >90% transmission through an array with only 10% free space can be explained by the waveguiding properties of the sub-wavelength apertures, with a randomly spaced array with such a density producing ≈70% transmission despite its un-optimised aperture spacings.

The SPP induced minima have been observed to increase in coupling efficiency and reduce in frequency with a more defect full copper foil surface. This opens the opportunity to exploit the conditions at this interface while not altering the localised aperture resonance.

Periodic spacing of the apertures is still important to the shape and strength of the transmission peak produced by the apertures. The 5:1 aspect ratio apertures used throughout this work have been shown to give up to 12 times the transmission as indicated by free space area. Care must be taken when designing the array dimensions so as to not introduce an SPP minimum in the vicinity of the transmission peak. That these minima show transmission as low as 10% indicates that the coupling into the surface mode is very efficient. This observation is at odds with many explanations of the EOT phenomena whose origin lie in the channelling of surface modes into a sub-wavelength hole as a method of greater than expected transmission.

Chapter 7

Conclusions

In the past decade, the concept of controlling and utilising spoof SPPs in the THz region has become a reality. The confinement and measurement of these SPP modes is well established in metals with periodic subwavelength features. The role these SPPs play in the EOT of sub-wavelength apertures is, however, less well defined, and still under investigation. It is this EOT, and the role of various resonant modes which contribute to the phenomena, that the work in this thesis has sought to investigate.

Chapter 2 presented a unique opportunity to compare the relative merits of the well-used time domain THz-TDS techniques with those of the recently developed frequency domain THz-VNA measurements. Beyond the limited frequency range provided by the VNA

measurement technique, the method has been found to outperform the THz-TDS system for every figure of merit. This, however, does not indicate the replacement of THz-TDS, as the reduced frequency range provided by the THz-VNA is a largely limiting factor for any solution in which THz-TDS can provide an adequate signal to noise ratio and frequency resolution. It does, however, indicate the final stage of closing the 'THz gap' as the mature communications and optical technologies both penetrate into the region in an active way.

Chapter 3 presented the underlying physics behind the resonant features observed in THz aperture arrays and the origin of the EOT phenomena. Beginning with an introduction to surface plasmons at optical frequencies, the well-established case for 'spoof' surface plasmons at THz frequencies is presented. Numerous theoretical and experimental studies into the excitation and confinement of THz SPPs put their existence beyond reasonable doubt. However the exact role of THz SPPs in aperture array transmission is not fully defined. The resonant modes of a single sub-wavelength rectangular aperture have also been presented as a possible origin for EOT. This 'localised resonance' is loosely referred to in many rectangular slot antenna publications, normally in relation to its effect upon the SPP transmission.

Chapter 4 presented the important concepts and background knowledge of FDTD simulation techniques used to modify and build an accurate experimental geometry for the non-commercial Lucifer simulation program. Lucifer has been used to simulate the transmission properties of free standing PEC arrays, and the results compared with experimental data and commercial simulation packages. The PEC approximation has been found to be valid in the THz region, with Lucifer producing highly accurate transmission properties for similar real arrays. The level of control over geometry, data acquisition and

manipulation, and the accuracy of Lucifer has been found to outperform that of a commercial FDTD simulation package at the cost of increased computational demand.

Chapter 5 presented the systematic investigation of the transmission spectra of aperture arrays at normal incidence. Free standing copper foils perforated with sub-wavelength 5:1 aspect ratio rectangular apertures have been produced by lithographic and electroplating techniques. Arrays of apertures in a square periodic lattice with a ratio of 5:1:7 aperture length: aperture width: periodic spacing, have been shown to produce a strong transmission peak, linearly scaling as the array dimensions vary at this fixed ratio. The location of this transmission peak has been found to be dominated by the rectangular aperture length, as described by the primary mode of a rectangular waveguide, and only loosely coupled to the periodic spacing of the apertures. As the periodic square lattice distancing is varied, for a fixed aperture, the transmission peak has been observed to narrow and become extinguished by a minimum at a frequency determined by the periodic spacing. This minimum, determined to be the excitation of the fundamental THz SPP mode, has not been found to enhance the transmission properties of the free-standing metal array, which shows >95% peak transmission when far removed from SPP resonant frequencies. Repeating for two other aperture sizings a similar fall in absolute transmission strength has been observed as the periodic spacing is varied. Asymmetrical array spacings have produced an arbitrarily small dip in transmission related to the y-direction periodic spacing, while maintaining a strong minimum defined by the x-direction spacing.

Chapter 6 reported on experiments that varied the incident angle between the incoming THz radiation and the free standing metal film. The sharp resonant features produced by this varying angle are observed from the THz-VNA transmission spectra. As the incident angle is increased, the SPP induced minimum reduces in frequency at a far greater rate than the

aperture induced transmission. As the minimum approaches the transmission peak its shape becomes asymmetrical and is sharpened into that commonly observed and reported as the [1,0] SPP transmission peak. The experimental observations by THz-VNA differ largely from those produced by Lucifer as well as a commercial frequency domain simulation package. The origin of these discrepancies is believed to lie in the imperfect surface of the copper foil by comparison to the perfect surface assumed in the simulations. A more defect-full copper foil has been shown to deviate even further in minimum position than that obtain by simulation, another strong indicator that this feature is SPP controlled.

The approach of this work differs from many other publications on THz EOT in rectangular aperture arrays, which fix the periodic lattice of the array and vary the aperture dimensions. This is a reasonable approach if you assume that the EOT phenomena is dominated by the excitation of SPPs, and seek to explain spectral shape changes by Fano-type interactions. However, the measurements presented in this thesis show that for a 5:1 aspect ratio rectangular aperture array the transmission can approach unity far removed from the SPP defined periodic spacing, and can achieve 68% transmission for a random array despite only ≈10% free space. Decoupling of the two resonant features shows that the EOT displayed by these arrays is dominated by an aperture defined waveguide resonance. Coupling to SPP modes has been found to alter the transmission of this mode, with a strong transmission minimum observed dependent upon x-periodicity, incident angle and surface conditions.

7.1 Further Work

The work presented in this thesis provides a new interpretation of the transmission spectra of free-standing sub-wavelength aperture arrays. However, the dependency of the SPP minima upon surface conditions and the deviation from simulation results this causes

requires more investigation. An electroplating technique allowing for the electroplating of a nickel structure with sub-micron width pores permeating throughout has been developed. Such a deeply sub-wavelength structure can be considered a true THz 'metamaterial', as opposed to that of a metal foil with features within an order of magnitude of the wavelength. Such a structure can provide a more thorough method of investigating the effect of surface roughness upon SPP confinement.

The porous nickel material can be fabricated by the extraction of the Cu content from a co-deposited NiCu alloy by reversal of the potential difference. The necessity of precise timings to ensure that the etching is stopped once the Cu has been removed, but before the Ni is also etched away, has required much trial and error in the process to achieve the results shown in Figure 7.1.

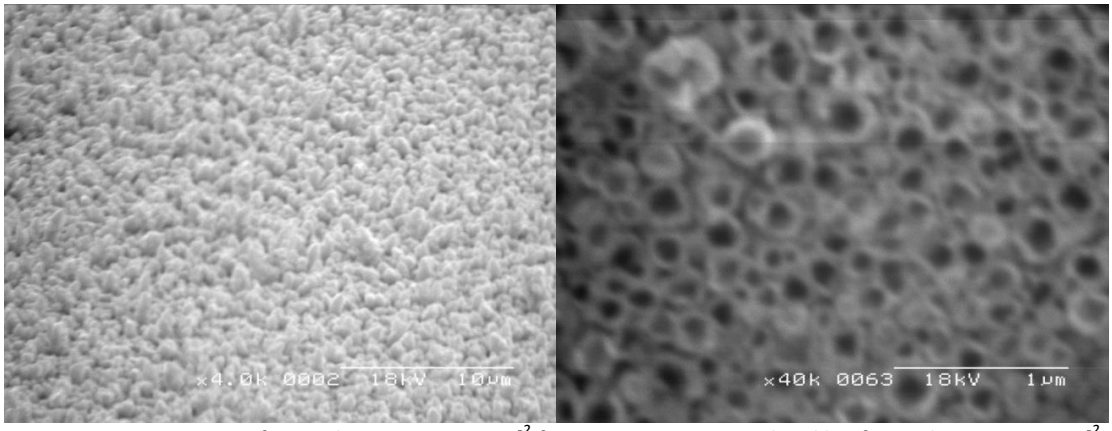

Figure 7.1:a. SEM image of NiCu plating at 10 mA cm^{-2} for 30 mins on a Cu seed and b. after etching at 5 mA cm^{-2} for 5 mins.

The porous Ni surface produced is however very delicate, and has not yet survived the delamination of the Cu foil from the Si substrate as described in section 5.1.

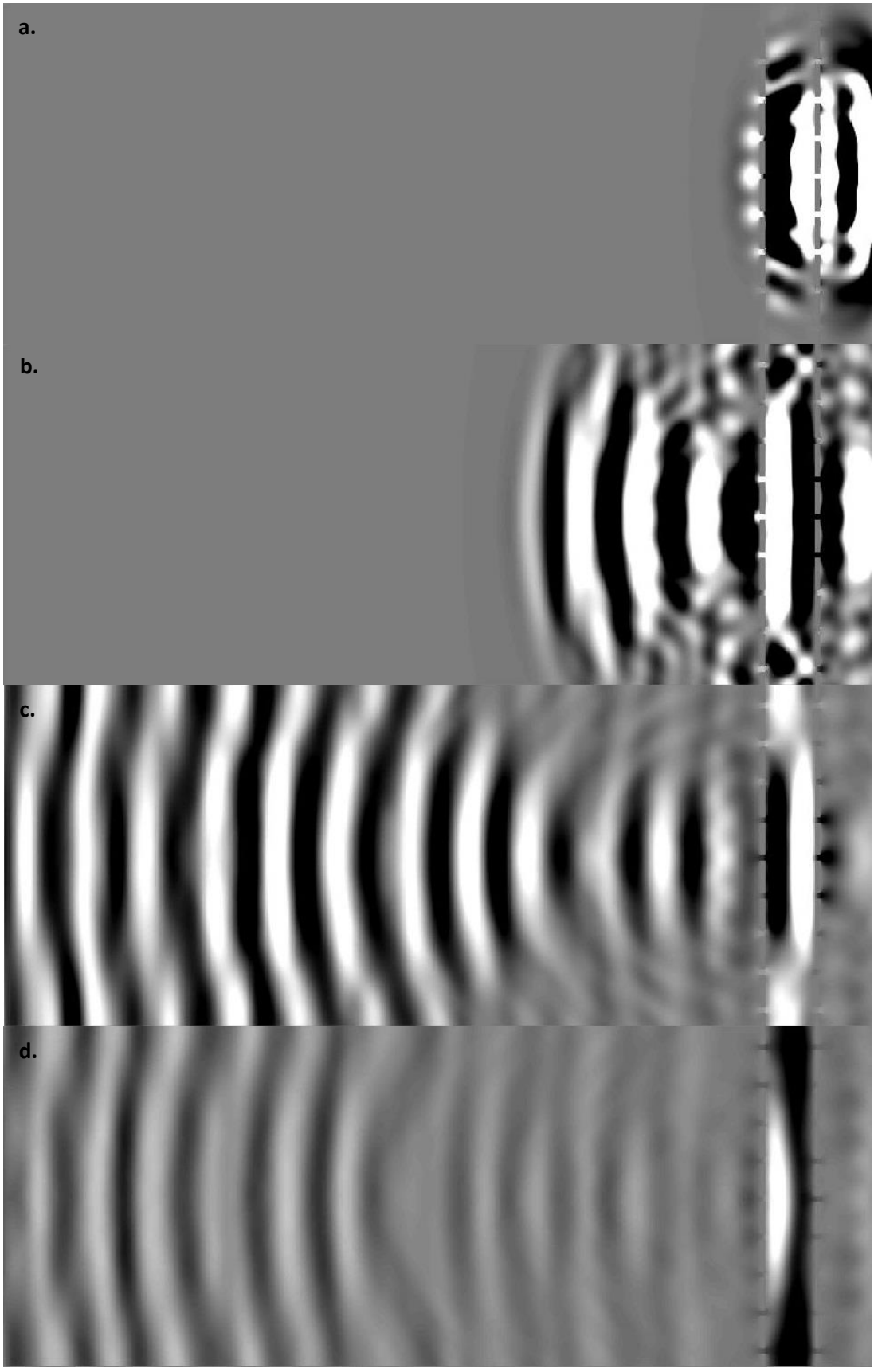

Figure 7.2: X-Z 2D cut plane of electric field for double array cavity mode FDTD simulation at; a. t ≈ 2 ps, b. t ≈ 6 ps, c. t ≈ 15 ps and d. t ≈ 20 ps.

The Lucifer FDTD program presented in chapter 4 and verified by THz-TDS measurements has been used to investigate the effect of bringing two free standing aperture arrays in close alignment. Figure 7.2 suggests that a strong resonant cavity mode can be excited, creating a standing-wave between the two arrays, decaying much more slowly than the individual apertures which comprise the arrays. Figure 7.3 shows the time domain response of the geometrical setup shown in Figure 7.2.

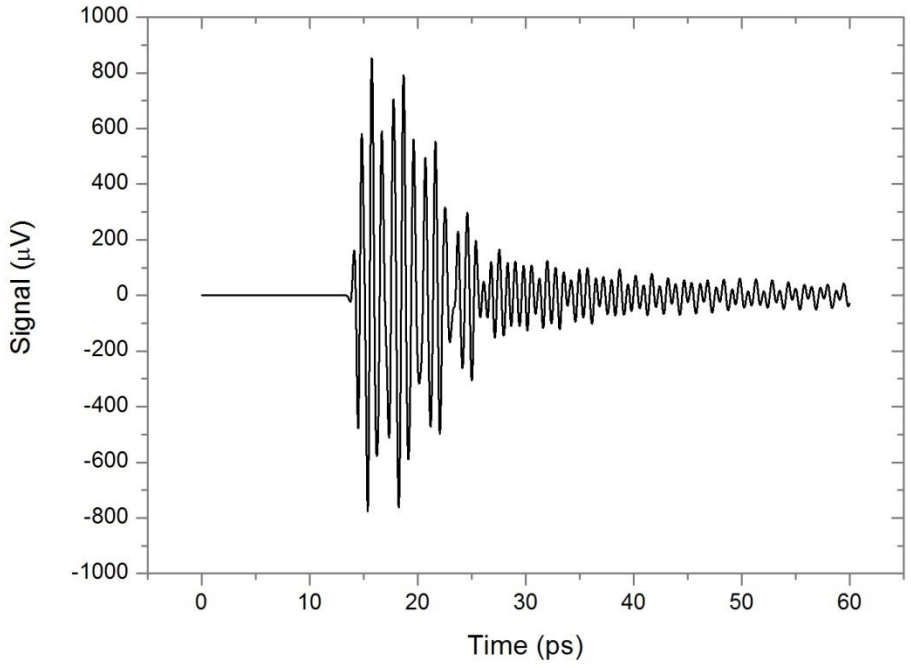

Figure 7.3: Time-domain response of double 150 x 30 μm aperture array with a 210 μm square lattice separated by 250 μm of free space.

Figure 7.3 shows that the resonant transmission has not fully decayed by 60 ps when the simulation ends; power remains in the cavity. For varied spacing between the arrays the relative strengths and frequency of these cavity modes can be seen in Figure 7.4.

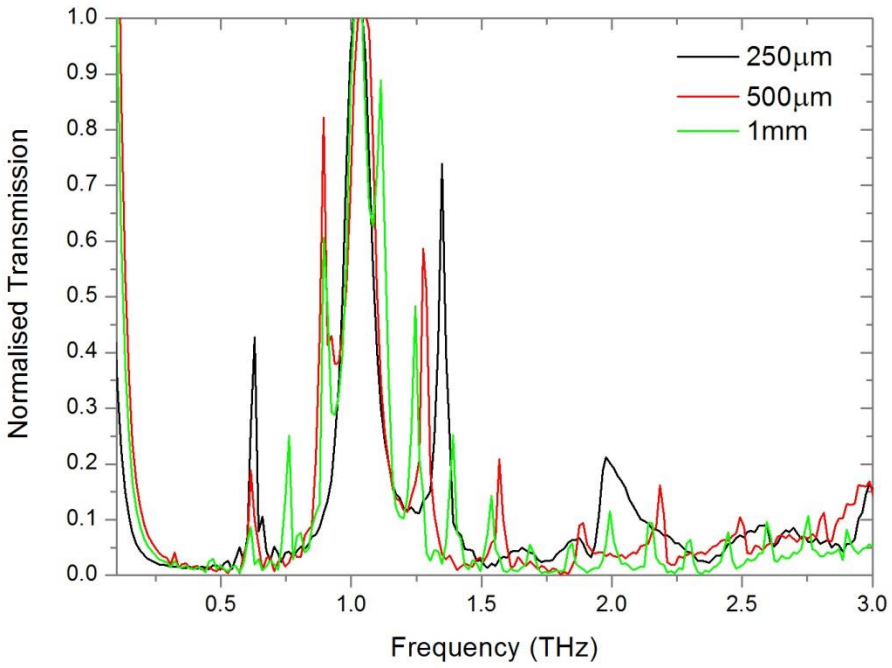

Figure 7.4: Normalised FDTD transmission of 150 x 30 µm aperture arrays with a 210 µm square lattice at varying cavity spacings.

This cavity mode is presumed to be highly sensitive to the dielectric properties of any material between the arrays with uses in gas and liquid sensing. A fabrication process to produce double arrays with a fixed spacing on either side of an ≈ 250 µm thick Si substrate, then etching away the Si to create the free space cavity, has been developed.

This cavity technique utilises the unique free standing nature of the metal foil arrays presented in this thesis for sensing purposes. Increased understanding of the interaction between and the role played by aperture resonance and SPP modes in rectangular sub-wavelength array transmission creates new possibilities in the application of THz SPPs.

Bibliography

[1] A. Adam, P. Planken, S. Meloni and J. Dik, “TeraHertz Imaging of Hidden Paint Layers on Canvas,” *Optics Express,* vol. 17, no. 5, pp. 3407-3414, 2009.

[2] J.-P. Caumes, A. Younus, S. Salort, B. Chassagne, B. Recur, A. Ziéglé, A. Dautant and E. Abraham, “Terahertz Tomographic Imaging of XVIIIth Dynasty Egyptian Sealed Pottery,” *Applied Optics,* vol. 50, no. 20, pp. 3604-3608, 2011.

[3] M. Bessou, B. Chassagne, J.-P. Caumes, C. Pradère, P. Maire, M. Tondusson and E. Abraham, “Three-Dimensional Terahertz Computed Tomography of Human Bones,” *Applied Optics,* vol. 51, no. 28, pp. 6738-6744, 2012.

[4] M. Bessou, H. Duday, J.-P. Caumes, S. Salort, B. Chassagne, A. Dautant, A. Ziéglé and E. Abraham, “Advantage of Terahertz Radiation Versus X-ray to Detect Hidden Organic Materials in Sealed Vessels,” *Optics Communications,* vol. 285, no. 21-22, pp. 4175-4179, 2012.

[5] A. G. Davies, A. D. Burnett, W. H. Fan, E. H. Linfield and J. E. Cunningham, “Terahertz Spectroscopy of Explosives and Drugs,” *Materials Today,* vol. 11, no. 3, pp. 18-26, 2008.

[6] K. Choi, T. Hong, K. I. Sim, T. Ha, B. C. Park, J. H. Chung, S. G. Cho and J. H. Kim, “Reflection Terahertz Time-Domain Spectroscopy of RDX and HMX Explosive,” *Journal of Applied Physics,* vol. 115, no. 2, p. 023105, 2014.

[7] G. Zieger, D. Born, S. Anders, E. Heinz, K. Peiselt, A. Brömel, V. Zakosarenko, T. May and H.-G. Meyer, “A Passive Submillimeter Video Camera for Security Applications,” in *Infrared, Millimeter, and Terahertz Waves (IRMMW-THz)*, Mainz, 2013.

[8] D. H. Auston, K. P. Cheung and P. R. Smith, “Picosecond Photoconducting Hertzian Dipoles,” *Applied Physics Letters,* vol. 45, no. 3, pp. 284-286, 1984.

[9] C. Fattinger and D. Grischkowsky, “Terahertz Beams,” *Applied Physics Letters,* vol. 54, no. 6, pp. 490-492, 1989.

[10] A. Redo-Sanchez and X.-C. Zhang, “Terahertz Science and Technology Trends,” *IEEE Journal of Selected Topics in Quantum Electronics,* vol. 14, no. 2, pp. 260-269, 2008.

[11] J. Xu, K. Plaxco and S. Allen, “Probing the Collective Vibrational Dynamics of a Protein in Liquid Water by Terahertz Absorption Spectroscopy,” *Protein Science,* vol. 15, pp. 1175-1181, 2006.

[12] M. Fleischmann, P. Hendra and A. McQuillan, “Raman Spectra of Pyridine Adsorbed at a Silver Electrode,” *Chemical Physics Letters,* vol. 26, no. 2, pp. 163-166, 1974.

[13] B. Liedberg, C. Nylander and I. Lundstrom, “Surface Plasmon Resonance for Gas Detection and Biosensing,” *Sensors and Actuators,* vol. 4, pp. 299-304, 1983.

[14] T. W. Ebbesen, H. J. Lezec, H. F. Ghaemi, T. Thio and P. A. Wolff, “Exraordinary Optical Transmission Through Sub-Wavelength Hole Arrays,” *Nature,* vol. 391, pp. 667-669, 1998.

[15] J. B. Pendry, L. Martín-Moreno and F. J. Garcia-Vidal, “Mimicking Surface Plasmons with

Structured Surfaces," *Science,* vol. 305, no. 5685, pp. 847-848, 2004.

[16] W. Zhang, "Resonant Terahertz Transmission in Plasmonic Arrays of Subwavelength Holes," *The European Physical Journal - Applied Physics,* vol. 43, no. 1, pp. 1-18, 2008.

[17] H. Yoshida, Y. Ogawa, Y. Kawai, S. Hayashi, A. Hayashi, C. Otani, E. Kato, F. Miyamaru and K. Kawase, "Terahertz Sensing Method for Protein Detection Using a Thin Metallic Mesh," *Applied Physics Letters,* vol. 91, no. 25, p. 253901, 2007.

[18] J. Han, X. Lu and W. Zhang, "Terahertz Transmission in Subwavelength Holes of Asymmetric Metal-Dielectric Interfaces: The Effect of a Dielectric Layer," *Journal of Applied Physics,* vol. 103, no. 3, p. 033108, 2008.

[19] L. Shen, X. Chen, X. Zhang and K. Agarwal, "Guiding Terahertz Waves by a Single Row of Periodic Holes on Planar Metal Surface," *Plasmonics,* vol. 6, no. 2, pp. 301-305, 2011.

[20] S. A. Maier, S. R. Andrews, L. Martín-Moreno and F. J. García-Vidal, "Terahertz Surface Plasmon-Polariton Propagation and Focusing on Periodically Corrugated Metal Wires," *Physical Review Letters,* vol. 97, p. 176805, 2006.

[21] D. Qu, D. Grischkowsky and W. Zhang, "Terahertz Transmission Properties of Thin, Subwavelength Metallic Hole Arrays," *Optics Letters,* vol. 29, no. 8, pp. 896-898, 2004.

[22] M. van Exter, C. Fattinger and D. Grischkowsky, "Terahertz Time-Domain Spectroscopy of Water Vapor," *Optics Letters,* vol. 14, no. 20, pp. 1128-1130, 1989.

[23] N. Krauss, M. Haas, S. Winnerl, M. Helm and T. Dekorsy, "Terahertz Emission Based on Large-Area Photoconductive Emitters Illuminated via Beam Interference," *Electronics*

Letters, vol. 51, no. 17, pp. 1357-1359, 2015.

[24] N. T. Yardimci, S.-H. Yang, C. W. Berry and M. Jarrahi, "High-Power Terahertz Generation Using Large-Area Plasmonic Photoconductive Emitters," *IEEE Transactions on Terahertz Science and Technology,* vol. 5, no. 2, pp. 223-229, 2015.

[25] Z. Piao, M. Tani and K. Sakai, "Carrier Dynamics and Terahertz Radiation in Photoconductive Antennas," *Japanese Journal of Applied Physics,* vol. 39, no. 1, pp. 96-100, 1999.

[26] J. T. Darrow, B. B. Hu, X.-C. Zhang and D. H. Auston, "Subpicosecond Electromagnetic Pulses from Large-Aperture Photoconducting Antennas," *Optics Letters,* vol. 15, no. 6, pp. 323-325, 1990.

[27] A. Dreyhaupt, S. Winnerl, T. Dekorsy and M. Helm, "High-Intensity Terahertz Radiation from a Microstructured Large-Area Photoconductor," *Applied Physics Letters,* vol. 86, p. 121114, 2005.

[28] G. Zhao, R. N. Schouten, N. van der Valk, W. T. Wenckebach and P. C. M. Planken, "Design and Performance of a THz Emission and Detection Setup Based on a Semi-Insulating GaAs Emitter," *Review of Scientific Instruments,* vol. 73, no. 4, pp. 1715-1719, 2002.

[29] I. Wilke and S. Sengupta, "Nonlinear Optical Techniques for Terahertz Pulse Generation and Detection-Optical Rectification and Electrooptic Sampling," in *Terahertz Spectroscopy: Principles and Applications*, CRC Press, 2007, pp. 41-72.

[30] Q. Wu and X.-C. Zhang, “Ultrafast Electro-Optic Field Sensors,” *Applied Physics Letters,* vol. 68, no. 12, pp. 1604-1606, 1996.

[31] E. Brigham, “The Discrete Fourier Transform,” in *The Fast Fourier Transform*, New Jersey, Prentice-Hall, Inc., 1974, pp. 91-109.

[32] E. Brigham, “Fourier Series and Sampled Waveforms,” in *The Fast Fourier Transform*, New Jersey, Prentice-Hall, Inc., 1974, pp. 75-90.

[33] J. L. Hestler, Y. Duan, B. Foley and T. W. Crowe, “THz Vector Network Analyzer Measuments and Calibration,” in *21st International Symposium on Space Terahertz Technology*, Oxford, 2010.

[34] M. Skolnik, “Introduction to Radar,” in *Radar Handbook*, McGraw-Hill, 1962, pp. 1.6-1.10.

[35] Keysight Technologies, 31 July 2014. [Online]. Available: http://literature.cdn.keysight.com/litweb/pdf/5980-2778EN.pdf. [Accessed 07 May 2015].

[36] D. Pines, “Collective Energy Losses in Solids,” *Reviews of Modern Physics,* vol. 28, no. 3, pp. 184-199, 1956.

[37] E. C. Le Ru and P. G. Etchegoin, Principles of Surface-Enhanced Raman Spectroscopy, Oxford: Elsevier, 2009.

[38] K. Kneipp, Y. Wang, H. Kneipp, L. T. Perelman, I. Itzkan, R. R. Dasari and M. S. Feld, “Single Molecule Detection Using Surface-Enhanced Raman Scattering (SERS),” *Physics*

Review Letters, vol. 78, no. 9, pp. 1667-1670, 1997.

[39] H. Raether, Surface plasmons on smooth and rough surfaces and on gratings, Berlin: Springer-Verlag, 1988.

[40] J. W. Cooley and J. W. Tukey, "An Algorithm for the Machine Calculation of Complex Fourier Series," *Mathematics of Computation,* vol. 19, no. 90, pp. 297-301, 1965.

[41] E. Kretschmann and H. Raether, "Radiative Decay of Non Radiative Surface Plasmons Excited by Light," *Z. Naturforsch,* vol. 23a, pp. 2135 - 2136, 1968.

[42] A. V. Zayats, I. I. Smolyaninov and A. A. Maradudin, "Nano-Optics of Surface Plasmon Polaritons," *Physics Reports,* vol. 408, no. 3-4, pp. 131-314, 2005.

[43] A. Otto, "Excitation of Nonradiative Surface Plasma Waves in Silver by the Method of Frustrated Total Reflection," *Zeitschrift ffir Physik,* vol. 216, no. 4, pp. 398-410, 1968.

[44] A. D. Rakic, A. B. Djurisic, J. M. Elazar and M. L. Majewski, "Optical Properties of Metallic Films for Vertical-Cavity Optoelectronic Devices," *Applied Optics,* vol. 37, no. 22, pp. 5271-5283, 1988.

[45] H. A. Bethe, "Theory of Diffraction by Small Holes," *Physics Review,* vol. 66, no. 7 and 8, pp. 163-182, 1944.

[46] H. Liu and P. Lalanne, "Microscopic Theory of the Extraordinary Optical Transmission," *Nature,* vol. 452, pp. 728-730, 2008.

[47] P. Lalanne, J. P. Hugonin and J. C. Rodier, "Theory of Surface Plasmon Generation at

Nanoslit Apertures," *Physics Review Letters,* vol. 95, no. 26, p. 263902, 2005.

[48] R. W. Wood, "On a Remarkable Case of Uneven Distribution of Light in a Diffraction Grating Spectrum," *Physical Society of London,* vol. 18, pp. 269-275, 1902.

[49] Lord Rayleigh, "On the Dynamical Theory of Gratings," *Proceedings of the Royal Society of London,* vol. 79, pp. 399-416, 1907.

[50] J. Strong, "Effect of Evaporated Films on Energy Distribution in Grating Spectra," *Physical Review,* vol. 49, pp. 291-296, 1936.

[51] U. Fano, "The Theory of Anomalous Diffraction Gratings and of Quasi-Stationary Waves on Metallic Surfaces," *Journal of the Optical Society of America,* vol. 31, pp. 213-222, 1941.

[52] L. Martín-Moreno, F. J. García-Vidal, H. J. Lezec, K. M. Pellerin, T. Thio, J. B. Pendry and T. W. Ebbesen, "Theory of Extraordinary Optical Transmission through Subwavelength Hole Arrays," *Physical Review Letters,* vol. 86, no. 6, pp. 1114-1117, 2001.

[53] T. Ongarello, F. Romanato, P. Zilio and M. Massari, "Polarization Independence of Extraordinary Transmission Trough 1D Metallic Gratings," *Optics Express,* vol. 19, no. 10, pp. 9426-9433, 2011.

[54] T. Bian, B. Dong and Y. Zhang, "Polarization Independent Extraordinary Transmission Through a Subwavelength Slit," *Optics Communications,* vol. 285, no. 6, pp. 1523-1527, 2012.

[55] M. A. Ordal, L. L. Long, R. J. Bell, S. E. Bell, R. R. Bell, R. W. Alexander and C. A. Ward,

"Optical Properties of the Metals Al, Co, Cu, Au, Fe, Pb, Ni, Pd, Pt, Ag, Ti, and W in the Infrared and Far Infrared," *Applied Optics,* vol. 22, no. 7, pp. 1099-1120, 1983.

[56] J. Gómez Rivas and A. Berrier, "Terahertz Plasmonics with Semiconductor Surfaces and Antennas," in *Asia Pacific Microwave Conference*, Suntec City, 2009.

[57] A. Rusina, M. Durach and M. I. Stockman, "Theory of Spoof Plasmons in Real Metals," *Applied Physics A,* vol. 100, pp. 375-378, 2010.

[58] J. Saxler, J. Gómez Rivas, C. Janke, H. P. M. Pellemans, P. H. Bolívar and H. Kurz, "Time-Domain Measurements of Surface Plasmon Polaritons in the Terahertz Frequency Range," *Physical Review B,* vol. 69, p. 155427, 2004.

[59] C. R. Williams, S. R. Andrews, S. A. Maier, A. I. Fernández-Domínguez, L. Martín-Moreno and F. J. García-Vidal, "Highly Confined Guiding of Terahertz Surface Plasmon Polaritons on Structured Metal Surfaces," *Nature Photonics,* vol. 2, pp. 175-179, 2008.

[60] J. F. O'Hara, R. D. Averitt and A. J. Taylor, "Prism Coupling to Terahertz Surface Plasmon Polaritons," *Optics Express,* vol. 13, no. 16, pp. 6117-6126, 2005.

[61] A. P. Hibbins, E. Hendry, M. J. Lockyear and J. R. Sambles, "Prism Coupling to 'Designer' Surface Plasmons," *Optics Express,* vol. 16, no. 25, pp. 20441-20447, 2008.

[62] D. E. Grupp, H. J. Lezec, T. Thio and T. W. Ebbesen, "Beyond the Bethe Limit: Tunable Enhanced Light Transmission Through a Single Sub-Wavelength Aperture," *Advanced Materials,* vol. 11, no. 10, pp. 860-862, 1999.

[63] A. Agrawal, H. Cao and A. Nahata, "Time-Domain Analysis of Enhanced Transmission

Through a Single Subwavelength Aperture," *Optics Express,* vol. 13, no. 9, pp. 3535-3542, 2005.

[64] K. Ishihara, T. Ikari, H. Minamide, J.-i. Shikata, K. Ohashi, H. Yokoyama and H. Ito, "Terahertz Near-Field Imaging Using Enhanced Transmission through a Single Subwavelength Aperture," *Japanese Journal of Applied Physics,* vol. 44, no. 29, pp. 929-931, 2005.

[65] K. Ishihara, K. Ohashi, T. Ikari, H. Minamide, H. Yokoyama, J.-i. Shikata and H. Ito, "Terahertz-Wave Near-Field Imaging with Subwavelength Resolution Using Surface-Wave-Assisted Bow-Tie Aperture," *Applied Physics Letters,* vol. 89, p. 201120, 2006.

[66] W. Zhu and A. Nahata, "Electric Field Vector Characterization of Terahertz Surface Plasmons," *Optics Express,* vol. 15, no. 9, pp. 5616-5624, 2007.

[67] H. Cao and A. Nahata, "Resonantly Enhanced Transmission of Terahertz Radiation Through a Periodic Array of Subwavelength Apertures," *Optics Express,* vol. 12, no. 6, pp. 1004-1010, 2004.

[68] H. Cao and A. Nahata, "Influence of Aperture Shape on the Transmission Properties of a Periodic Array of Subwavelength Apertures," *Optics Express,* vol. 12, no. 16, pp. 3664-3672, 2004.

[69] J. W. Lee, M. A. Seo, D. J. Park, D. S. Kim, S. C. Jeoung, C. Lienau, Q.-H. Park and P. C. M. Planken, "Shape Resonance Omni-Directional Terahertz Filters with Near-Unity Transmittance," *Optics Express,* vol. 14, no. 3, pp. 1253-1259, 2006.

[70] J. W. Lee, J.-K. Yang, I.-B. Sohn, C. Kang and C.-S. Kee, "Folded Slot Resonator Array with Efficient Terahertz Transmission," *Optics Communications,* vol. 293, pp. 155-159, 2013.

[71] F. Miyamaru, M. Tanaka and M. Hangyo, "Effect of Hole Diameter on Terahertz Surface-Wave Excitation in Metal-Hole Arrays," *Physical Review B,* vol. 74, p. 153416, 2006.

[72] J. Bravo-Abad, L. Martín-Moreno, F. J. García-Vidal, E. Hendry and J. Gómez Rivas, "Transmission of Light Through Periodic Arrays of Square Holes: From a Metallic Wire Mesh to an Array of Tiny Holes," *Physical Review B,* vol. 76, p. 241102(R), 2007.

[73] T. Matsui, A. Agrawal, A. Nahata and Z. V. Vardeny, "Transmission Resonances Through Aperiodic Arrays of Subwavelength Apertures," *Nature,* vol. 446, pp. 517-521, 2007.

[74] J. Bravo-Abad, A. I. Fernández-Domínguez, F. J. García-Vidal and L. Martín-Moreno, "Theory of Extraordinary Transmission of Light through Quasiperiodic Arrays of Subwavelength Holes," *Physical Review Letters,* vol. 99, p. 203905, 2007.

[75] A. K. Azad and W. Zhang, "Resonant Terahertz Transmission in Subwavelength Metallic Hole Arrays of Sub-Skin-Depth Thickness," *Optics Express,* vol. 30, no. 21, pp. 2945-2947, 2005.

[76] J. W. Lee, M. A. Seo, J. Y. Sohn, Y. H. Ahn, D. S. Kim, S. C. Jeoung, C. Lienau and Q.-H. Park, "Invisible Plasmonic Meta-Materials through Impedance Matching to Vacuum," *Optics Express,* vol. 13, no. 26, pp. 10681-10687, 2005.

[77] R. Gordon, A. G. Brolo, A. McKinnon, A. Rajora, B. Leathem and K. L. Kavanagh, "Strong Polarization in the Optical Transmission through Elliptical Nanohole Arrays," *Physical*

Review Letters, vol. 92, p. 037401, 2004.

[78] K. J. Klein Koerkamp, S. Enoch, F. B. Segerink, N. F. van Hulst and L. Kuipers, "Strong Influence of Hole Shape on Extraordinary Transmission through Periodic Arrays of Subwavelength Holes," *Physical Review Letters,* vol. 92, no. 18, p. 183901, 2004.

[79] F. J. García-Vidal, E. Moreno, J. A. Porto and L. Martín-Moreno, "Transmission of Light through a Single Rectangular Hole," *Physcal Review Letters,* vol. 95, p. 103901, 2005.

[80] Z. Ruan and M. Qiu, "Enhanced Transmission through Periodic Arrays of Subwavelength Holes: The Role of Localized Waveguide Resonances," *Physical Review Letters,* vol. 96, p. 233901, 2006.

[81] J. Han, A. K. Azad, M. Gong, X. Lu and W. Zhang, "Coupling Between Surface Plasmons and Nonresonant Transmission in Subwavelength Holes at Terahertz Frequencies," *Applied Physics Letters,* vol. 91, p. 071122, 2007.

[82] D. J. Park, S. B. Choi, Y. H. Ahn, F. Rotermund, I. B. Sohn, C. Kang, M. S. Jeong and D. S. Kim, "Terahertz Near-Field Enhancement in Narrow Rectangular Apertures on Metal Film," *Optics Express,* vol. 17, no. 15, pp. 12493-12501, 2009.

[83] F. Miyamaru and M. W. Takeda, "Coupling between Localized Resonance and Excitation of Surface Waves in Metal Hole Arrays," *Physical Review B,* vol. 79, p. 153405, 2009.

[84] Y.-W. Jiang, L. D.-C. Tzuang, Y.-H. Ye, Y.-T. Wu, M.-W. Tsai, C.-Y. Chen and S.-C. Lee, "Effect of Wood's Anomalies on the Profile of Extraordinary Transmission Spectra through Metal Periodic Arrays of Rectangular Subwavelength Holes with Different

Aspect Ratio," *Optics Express,* vol. 17, no. 4, pp. 2631-2637, 2009.

[85] E. Hendry, F. J. Garcia-Vidal, L. Martin-Moreno, J. Gómez Rivas, M. Bonn, A. P. Hibbins and M. J. Lockyear, "Optical Control over Surface-Plasmon-Polariton-Assisted THz Transmission Through a Slit Aperture," *Physical Review Letters,* vol. 100, p. 123901, 2008.

[86] J. Bromage, S. Radic, G. P. Agrawal, C. R. Stroud, P. M. Fauchet and R. Sobolewski, "Spatiotemporal Shaping of Half-Cycle Terahertz Pulses by Diffraction through Conductive Apertures of Finite Thickness," *Journal of the Optical Society of America B,* vol. 15, no. 4, pp. 1399-1405, 1998.

[87] M. A. Seo, H. R. Park, S. M. Koo, D. J. Park, J. H. Kang, O. K. Suwal, S. S. Choi, P. C. M. Planken, G. S. Park, N. K. Park, Q. H. Park and D. S. Kim, "Terahertz Field Enhancement by a Metallic Nano Slit Operating Beyond the Skin-Depth Limit," *Nature Photonics,* vol. 3, pp. 152-156, 2009.

[88] J. Valentine, S. Zhang, T. Zentgraf, E. Ulin-Avila, D. A. Genov, G. Bartal and X. Zhang, "Three-Dimensional Optical Metamaterial with a Negative Refractive Index," *Nature,* vol. 455, pp. 376-379, 2008.

[89] K. Song and P. Mazumder, "Active Terahertz Spoof Surface Plasmon Polariton Switch Comprising the Perfect Conductor Metamaterial," *IEEE Transactions on Electronic Devices,* vol. 56, no. 11, pp. 2792-2799, 2009.

[90] F. Miyamaru and M. Hangyo, "Anomalous Terahertz Transmission through Double-Layer Metal Hole Arrays by Coupling of Surface Plasmon Polaritons," *Physcial Review B,* vol.

71, p. 165408, 2005.

[91] K. Yee, “Numerical Solution of the Initial Boundary Value Problems Involving Maxwell's Equations in Isotropic Media,” *IEEE Transactions on Antennas and Propagation,* vol. 14, no. 3, pp. 302-307, 1966.

[92] J. B. Schneider, “Dispersion in the FDTD grid,” in *Understanding the finite-difference time-domain method*, 2015, pp. 165-169.

[93] G. Kumar, S. Pandey, A. Cui and A. Nahata, “Planar Plasmonic Terahertz Waveguides Based on Periodically Corrugated Metal Films,” *New Journal of Physics,* vol. 13, p. 033024, 2011.

[94] Q. Gan, Z. Fu, Y. J. Ding and F. J. Bartoli, “Ultrawide-Bandwidth Slow-Light System Based on THz Plasmonic Graded Metallic Grating Structures,” *Physical Review Letters,* vol. 100, p. 256803, 2008.

[95] O. P. Lehar, M. A. Spak, S. Meyer, R. R. Dammel, C. J. Brodsky and C. G. Willson, “Resist rehydration during thick film processing,” in *Advances in Resist Technology and Processing XVIII*, Santa Clara, 2001.

[96] Microchemicals, “Microchemicals Technical Information,” [Online]. Available: www.microchemicals.eu/technical-information. [Accessed 29 Oct 2012].